

Modelling the Rheology and Internal Resistance of Alginate-based Semi-solid Flow Batteries

W.S.J.M. Peters

Modelling the Rheology and Internal Resistance of Alginate-based Semi-solid Flow Batteries

by

W.S.J.M. Peters

to obtain the degree of Master of Science
at the Delft University of Technology,
to be defended publicly on Wednesday May 11, 2022 at 10:00 AM.

Student number: 4455495
Project duration: August 31, 2021 – May 1, 2022
Thesis committee: dr. ir. M. Rohde, TU Delft, supervisor
dr. E. M. Kelder, TU Delft
dr. ir. D. Lathouwers, TU Delft

This thesis is confidential and cannot be made public until May 11, 2022.

An electronic version of this thesis is available at <http://repository.tudelft.nl/>.

Abstract

The rise of intermittent electricity sources has increased the relevance of large scale energy storage technologies. Semi-solid flow batteries are a promising technology for large-scale energy storage. In search of a safe system with inexpensive components, a new semi-solid flow battery with an aqueous, alginate-based electrolyte is studied. The electrolyte contains conducting carbon black particles to improve electronic conduction. The energy efficiency of semi-solid flow batteries is diminished by internal electric resistance and fluid friction. This thesis aims to contribute to a better understanding of these two sources of energy loss. To this end, the rheology and electric field are modelled to find the internal electronic resistance and pumping power under various flow conditions. Furthermore, an experimental method for measurements of viscosity and conductivity, which are important inputs for the models, is developed.

In this research, a lattice Boltzmann fluid dynamics model and a finite volume model for the electric field are developed and validated. The fluid dynamics model simulates the flow of the electrolyte through the battery. Based on the flow field, the electronic conductivity in the flow channel, which is a function of shear rate, is determined. The conductivity is an input for the finite volume model that computes the electric field in the battery. The internal electronic resistance of the electrolyte is derived from the electric field. Using this approach, the flow of the electrolyte and the electric field in the battery are simulated for a range of inlet velocities. As the the viscosity and conductivity of the alginate-based electrolyte have not yet been characterised, a nonaqueous carbon black suspension whose viscosity and conductivity are known, is used as a replacement. For a flow channel with a length of 22.5mm, a height of 5mm and a width of 50mm, the internal electronic resistance of the carbon black suspension is found to have a minimum of 5 k Ω at zero fluid velocity. This is orders of magnitude higher than the internal ionic resistance of the membrane (0.1 Ω) and the electrolyte (0.9 Ω). Ion transport therefore is not a limiting factor for the reaction rate in this SSFB. The pumping power increases with velocity as a power law with an exponent of ~ 1.5 . This steep increase should be taken into consideration when deciding on the inlet velocity of the semi-solid flow battery. Developing a coupled electrochemical-transport model is recommended to get a more complete description of the electrochemical performance.

Due to their different compositions, the replacement of the aqueous alginate-based electrolyte by a nonaqueous carbon black suspension in all likelihood causes a significant deviation in the output of the simulations. The viscosity and conductivity of the aqueous alginate-based electrolyte must therefore be characterised to get a more reliable estimation for the electronic resistance and pumping power. The proposed setup for these measurements is a parallel plate rheometer equipped with a dielectro rheological device. It measures torque and conductance as a function of angular frequency. The torque-angular frequency data can be converted into a viscosity-shear rate curve using an existing method. For the conversion of conductance as a function of angular frequency into conductivity as a function of shear rate, a dedicated algorithm is developed and validated. The error of the algorithm was found to be well below 5 % for all validation cases. This precision is adequate for the purpose of this study.

Nomenclature

Abbreviations

ABB	Anti bounce back (boundary technique)
BGK	Bhatnagar-Gross-Krook (collision operator)
BB	Bounce back (boundary technique)
CAES	Compressed air energy storage
CES	Cryogenic energy storage
CFD	Computational fluid dynamics
CV	Convective (boundary technique)
DRD	Dielectro rheological device
EP	Extrapolation (boundary technique)
FMLB	Filter matrix lattice Boltzmann
FVM	Finite volume method
LBM	Lattice Boltzmann method
MRT	Multiple relaxation time
NEBB	Non-equilibrium bounce back (boundary technique)
SSFB	Semi-solid flow battery
RFB	Redox Flow Battery

Chemical formulas

Cl^-	Chlorine ion
Fe^{2+}/Fe^{3+}	Divalent/trivalent iron ion
$Fe - Alg$	Iron alginate
Li	Lithium
Mn^{2+}/Mn^{3+}	Divalent/trivalent manganese ion
$Mn - Alg$	Manganese alginate
MnO_2	Manganese dioxide
Na^+	Sodium ion
PO_4	Phosphate
Ti	Titanium
Zn	Zinc

Contents

1	Introduction	1
1.1	Semi-solid Flow Batteries	1
1.2	Review of Large-scale Energy Storage Technologies	2
1.3	Recent work on Semi-solid Flow Batteries	3
1.3.1	Carbon Black Suspensions	3
1.3.2	Electrolyte Composition	4
1.4	Thesis goal	4
1.4.1	Contribution to the Current State of Knowledge	5
1.4.2	Thesis Outline	6
2	Theory	7
2.1	Working Principle of Alginate-based Semi-solid Flow Battery	8
2.1.1	Chemical Composition	8
2.1.2	Electron Transport	8
2.1.3	Ion Transport	9
2.2	Fluid Dynamics	10
2.2.1	Kinetic Theory	11
2.2.2	Computational Fluid Dynamics	11
2.2.3	Lattice Boltzmann Method	11
2.2.4	Pumping Power	13
2.3	Internal Resistance	14
2.4	Electrochemical Performance	15
2.5	Fluid Characteristics	16
3	Description of Fluid Dynamics Model	19
3.1	Multiple Relaxation Time Lattice Boltzmann Method	19
3.2	Filter Matrix Lattice Boltzmann Method	21
3.3	Geometry	23
3.4	Boundary Conditions	24
3.4.1	Walls	24
3.4.2	Inlet	25
3.4.3	Outlet	26
4	Description of Electric Field Model	29
4.1	Geometry	29
4.2	Discretisation	30
4.3	Solution Method	31
4.4	Electric Current and Resistance	32
5	Description of Experimental Method for Rheo-impedance Measurements	33
5.1	Experimental Setup	33
5.2	Viscosity Measurements	34
5.2.1	Viscosity Conversion Method	35
5.3	Conductivity Measurements	36
5.3.1	Conductivity Conversion Method	36
6	Results and Discussion	39
6.1	Validation of Fluid Dynamics Model	39
6.1.1	Analytical Solution	39
6.1.2	Boundary Conditions	40
6.1.3	Benchmarking	40
6.1.4	Wall Friction	43

6.2	Validation of Finite Volume Method	45
6.3	Flow Behaviour and Resistance of Carbon Black Suspension	47
6.3.1	Grid Convergence	47
6.3.2	Internal Resistance Optimization	49
6.3.3	Pumping Power.	50
6.3.4	Effect of Viscosity-cutoff	51
6.3.5	Asymmetries	53
6.4	Total Internal Resistance.	53
6.5	Validation of Conductivity Conversion Method	55
7	Conclusions and Recommendations	57
7.1	Simulation of Rheology and Electric Field in SSFBs	57
7.2	Experimental Method for Rheo-impedance Measurements	58
7.3	Recommendations	58
A	Systematic Analysis of Boundary Techniques for Lattice Boltzmann Method	59
B	Simulation Parameters	61
C	Codes	63

Introduction

Over the past decades it has become increasingly apparent that greenhouse gases are responsible for climate change. The Intergovernmental Panel on Climate Change reported in 2021 that greenhouse gas caused by human activity is responsible for a 1 K to 2 K increase in global surface temperature. This human-induced climate change is affecting weather and climate extremes across the globe [1]. The energy sector is a main contributor to greenhouse gas emissions: approximately 75 % of greenhouse gas is emitted as a result of energy generation [2]. Driven by economic and population growth, energy demand has risen over the past decades and is expected to keep rising. To meet the growing energy demand while reducing greenhouse gas emissions, polluting energy sources must be replaced with renewable energy sources. Renewable energy sources such as solar photovoltaics and wind have experienced rapid growth and this growth is likely to continue [3]. Since these technologies are dependent on weather conditions and season there is a demand for carbon free, large-scale energy storage to balance the grid.

Large-scale energy storage technologies must be affordable, safe and have a long cycle life. Other relevant criteria are power and energy density, availability of materials and recyclability. There is a wide variety of carbon free, large-scale energy storage technologies such as pumped hydro storage, compressed air energy storage, hydrogen and batteries. Each technology comes with its own (dis)advantages and the preferred storage method greatly depends on the required capacity, power and duration of storage. Flow batteries are a promising large-scale energy storage technology because their power and capacity are decoupled. Redox flow batteries have received a lot of attention in the last 30 years. The vanadium redox flow battery is the most established flow battery with over 30 active installations across the globe [4]. However, due to a low energy density and expensive materials, its costs currently are too high to be competitive [5]. The semi-solid flow battery is a novel flow battery concept with a higher energy density and thus potentially a lower cost of storage. This research focuses on a semi-solid flow battery with an aqueous alginate-based electrolyte. This electrolyte was chosen for its safe, abundant and affordable components [6]. Internal resistance and friction diminish the energy efficiency of semi-solid flow batteries. The goal of this research is to gain a better understanding of these two sources of energy loss and to evaluate how they are influenced by the rheology.

This chapter gives an introduction into semi-solid flow batteries in section 1.1. This is followed by a review of large-scale energy storage technologies in section 1.2. Subsequently, section 1.3 gives an overview of recent work on similar systems. The research questions and an overview of the project are discussed in section 1.4.

1.1. Semi-solid Flow Batteries

Flow batteries are devices that convert chemical energy into electricity and vice versa via redox reactions. Their working principle is similar to that of regular batteries, except that flow batteries have a constant supply of new active material. Electrochemical energy is stored outside the battery in two fluids that are kept in separate tanks. The fluids are electrolytes with active material (i.e. a redox couple).

When pumped through the battery, the fluids react with each other to release energy (discharging) or store energy (charging). The half cells are separated by a membrane that functions as salt bridge. The two fluids contain different redox couples which results in a potential difference between the half cells. If the two half cells are connected via an external circuit, redox half-reactions occur in the two half cells and an electronic current flows between them. To balance this electron flow, ions move between the half cells through the membrane. Depending on the external circuit, the fluids are either charged or discharged. The storage of the fluids in separate tanks has several advantages compared to regular batteries, whose reactants are stored inside the half cells:

- Battery power is decoupled from battery capacity: the power depends on the characteristics of the cell while the capacity depends on the size of the fluid reservoirs. As a consequence, flow batteries can be tailored to specific applications.
- Storage in tanks is cheaper than storage of reactants in batteries. Decoupling the power and storage components thus comes with a cost benefit [7][8].
- Flow batteries are inherently safe. Thermal runaway is impossible as reactants are stored in separate tanks [9].

Two types of flow batteries can be distinguished: Redox flow batteries (RFBs) and semi-solid flow batteries (SSFBS). In RFBs the redox active ions are dissolved in the electrolyte whereas in SSFBs these ions are stored in solid particles that are dispersed in the electrolyte. Their differences and (dis)advantages are listed below:

- The energy density of SSFBs is not limited by ion solubility while that of RFBs is. SSFBs therefore have an energy density 20 to 30 times that of conventional RFBs [10].
- Membranes of SSFBs are much simpler than those of RFBs. A porous separator that blocks solid particles and passes ions, suffices for SSFBs. RFBs require a more complex ion-exchange membrane that blocks the active ions and passes other ions [5][11].
- In RFBs the fluids flow through a porous electrode. The reactions occur at the surface of this electrode. In SSFBs, the porous electrode is replaced by conducting carbon black particles that are dispersed in the fluids. These particles form electronic conducting networks to connect the active material to the current collectors [12].
- While RFB electrolytes are solutions, SSFB electrolytes are suspensions. SSFBs therefore have a higher viscosity and thus higher pumping losses compared to RFBs [11].

This research focuses on an SSFB with an aqueous alginate-based electrolytes and conducting carbon black particles. Together with cations (positive ions) the alginates form hydrogels in aqueous solutions. These hydrogels are the active part of this SSFB. Alginates are especially promising since they are abundant in nature and non-toxic. The cations are iron and manganese ions, which are similarly abundant in nature. Because of their aqueous nature the electrolytes are non-flammable.

1.2. Review of Large-scale Energy Storage Technologies

This section provides a concise overview of conventional and upcoming carbon free large-scale energy storage technologies. These technologies are compared qualitatively to SSFBs, which helps to understand the potential of SSFBs as large-scale energy storage method.

- With 93% of the total energy storage capacity in 2020, **pumped hydro storage** currently is the most mature form of large-scale energy storage [13]. A pumped hydro storage system consists of two large water reservoirs at different heights in which energy is stored as gravitational energy. When there is a low power demand, water is pumped to the upper reservoir, and when there is high power demand it flows back down, generating electricity via a turbine. Pumped hydro is suitable for storage periods ranging from hours to years, depending on the size of the reservoirs. Its advantages include a high round trip efficiency, long lifetime, fast response time and low storage costs. However, since the development costs of pumped hydro storage largely depend on geographical conditions, its applicability is limited [14].

- **Compressed air energy storage (CAES)** stores energy by compressing air in a reservoir. It has a low energy density and thus requires large reservoirs to store significant amounts of energy. Because artificial reservoirs are very costly, usually underground caverns are used for the storage of compressed air. CAES is a very cost-effective energy storage method and is capable of storing energy for periods of over a year. However, as a consequence of the use of natural reservoirs, CAES too has geographical limitations [15].
- **Cryogenic energy storage (CES)** stores energy in liquified gases at cryogenic temperatures [16]. This emerging storage method is attractive because of its long cycle life, cost effectiveness and relatively high energy density. Its storage duration ranges from hours to months [17]. Main drawbacks are a low round trip efficiency and safety concerns related to leakage [18].
- **Batteries** have a high energy density, an almost instant response time, a long cycle life and a high efficiency. This makes them very suitable for mobile applications and applications where a short response time is of importance. For grid scale storage of energy however, the need for rare materials and high material, processing and maintenance costs pose significant limitations [18].
- **Hydrogen** is an upcoming large-scale energy storage technology with a high energy density compared to other technologies. Hydrogen in the form of (compressed) gas or post-processed into methane (synthetic natural gas) stores chemical energy. This makes it suitable for long term storage and has the additional advantage that the energy can be easily redistributed over large distances. Its disadvantages include a low volumetric energy density (at room temperature hydrogen is a gas) and a low round trip efficiency compared to batteries. [19]

SSFBS have high efficiencies similar to those of pumped hydro and CAES. Its storage costs are higher compared to pumped hydro and CAES, but a major advantage is the lack of geographical limitations. Flow batteries have a higher round trip efficiency and faster response time than CES on the one hand, but higher energy storage costs on the other hand [20]. Research by MIT [7] into the levelised cost of storage shows that costs of both hydrogen and SSFBs decrease with discharge duration. For storage periods of longer than a day, both SSFBs and hydrogen outperform regular lithium ion batteries and vanadium redox flow batteries. This is mainly due to high cost of power related components, i.e. the components related to the conversion of chemical into electrical energy. (Since SSFBs are still in an early stage of development, the results of this feasibility study by MIT might differ significantly from reality.) In regular batteries, power and capacity are intertwined while for both SSFBs and hydrogen power and energy are scaled independently.

In conclusion, the best-suited technology differs per case, as a result of the diverse range of criteria at play in large-scale energy storage. Given that the SSFB is still in its infancy, it is hard to predict its exact performance and hence its competitiveness with other technologies. This thesis aims to contribute to the understanding of SSFBs.

1.3. Recent work on Semi-solid Flow Batteries

In this section relevant recent work on SSFBs is presented. Since the focus of this thesis is the internal electrical resistance, this literature review concentrates on aspects of the battery that affect the resistance.

1.3.1. Carbon Black Suspensions

As touched upon in section 1.1, electrolytes of SSFBs contain carbon black particles to enhance their electronic conductivity. Carbon black particles cluster to form electron conducting networks. Above a certain carbon black concentration (the percolation threshold), these networks span the entire flow channel resulting in a steep electronic conductivity increase [21][22].

- In a study of aqueous dispersions of carbon black, the fluid was found to be non-Newtonian. This means that the fluid's viscosity changes with shear rate. This behaviour is attributed to shear induced changes in size and shape of carbon black microstructures. The study further found out that, when varying the carbon black concentration, the percolation threshold was at approximately the same concentration at which the viscosity shows a steep increase [21].

- Other research into aqueous carbon black suspensions has shown that the pH influences the viscosity and shear behaviour of the fluid. In basic fluids (i.e. $pH > 7$) carbon black suspensions exhibit shear thinning behaviour. This is explained by an increased hydrophobicity of the carbon black and hence an increased tendency to agglomerate. Stronger agglomeration causes a higher viscosity. Shearing the fluid decreases the agglomeration which results in shear thinning behaviour. This effect is stronger at higher concentrations [23].
- Research into non-aqueous carbon black suspensions has demonstrated that both conductivity and viscosity depend on shear rate. Again, the fluid shows shear thinning behaviour. The conductivity is at its lowest at medium shear rates. At zero and low shear rates, the carbon black networks are sustained, which comes with a high conductivity and viscosity. As the shear rate increases, the continuous networks are broken up resulting in a sharp drop of conductivity as well as viscosity. As shear rate increases further, another type of carbon black clusters form resulting in a slight increase in conductivity. At high shear rates, only very small carbon black clusters remain resulting in a high effective density of carbon black chains which enhances the conductivity further [22].
- Research by Narayanan *et al.* shows similar agglomerating behaviour in nonaqueous carbon black suspensions. It additionally demonstrates a shear history dependence. This thixotropic behaviour, too, is attributed to the formation and breaking down of carbon black microstructures [12].

1.3.2. Electrolyte Composition

A wide range of materials has been considered for SSFBs. Some relevant compositions are listed below.

- Non-aqueous SSFBs: Non-aqueous electrolytes generally have higher energy densities than aqueous electrolytes. Energy density is the product of capacity and voltage. Owing to their narrow electrochemical window, aqueous electrolytes impose an upper limit of 1.23 V on the cell potential [8][24]. Major drawbacks of non-aqueous electrolytes are their flammability and high costs [24]. Furthermore, carbon black conductivity in non-aqueous electrolytes at rest typically is at least one order of magnitude lower than in aqueous electrolytes [5][7][22]. Non-aqueous electrolytes are often combined with lithium-ion battery materials as active particles. This electrolyte could potentially reach energy densities that are sufficiently high for the use in all electric vehicles [8].
- Aqueous $LiTi_2(PO_4)_3-LiFePO_4$ SSFB: The first aqueous SSFB was demonstrated in 2013 and was based on the $LiTi_2(PO_4)_3-LiFePO_4$ couple as active material. In addition to the experimental study, a model was set up to simulate the flow and electrochemical behaviour [5]. This study underlines the importance of properly choosing the operating conditions to maximise cell efficiency. In addition, several parasitic reactions that degrade cell efficiency were identified.
- $Zn - MnO_2$ SSFB with aqueous electrolyte: Manganese dioxide is an inexpensive and abundant active material. This semi-solid electrolyte has been reported to have significant pumping losses due to its high viscosity. These pumping losses increase the cost of power. Nevertheless, an economical feasibility study has demonstrated that, mainly due to its low material costs, this SSFB is more cost-effective than Li-ion batteries and Vanadium redox flow batteries for storage periods longer than one day [7].

1.4. Thesis goal

To meet the need of cheap and safe large scale energy storage, an aqueous SSFB with an alginate-based electrolyte suspension has been proposed. Internal electrical resistance and friction diminish energy efficiency and thus increase the cost of power. This study aims to contribute to a better understanding of both internal electrical resistance and friction in SSFBs. Previous studies into carbon black suspensions have shown that the presence of carbon black particles affects the viscosity as well as the conductivity the slurry. This is attributed to the formation of carbon black microstructures. Shearing the fluid reforms the microstructures, resulting in a conductivity and viscosity change [21][22]. Hence, the rheological and electrical properties are intertwined. This leads to the following research questions:

1. *What is the internal resistance of an SSFB with alginate-based electrolyte and how is it influenced by the rheology?*

This question is split up in the following sub-questions:

- (a) *What is the flow profile and how does it depend on rheological properties?*
 - (b) *How does electronic conductivity relate to shear rate? Which other factors determine the electronic resistivity? What is the electronic resistivity of the fluid as a function of location and time?*
 - (c) *Which factors determine the internal ionic resistivity?*
 - (d) *How are the internal electronic and ionic resistance related to each other and to the total resistance.*
2. *What is the required pumping power for an alginate-based SSFB?*

1.4.1. Contribution to the Current State of Knowledge

To answer the research questions the following approach was taken:

- A two dimensional **fluid dynamics model** was developed to simulate the flow of the suspension through the battery. This fluid dynamics simulation is capable of modeling non-Newtonian fluids. Based on a direct relation between shear rate and conductivity, the conductivity as a function of location was derived.
- A **finite volume model** was set up to model the **electric field** in the flow channel and compute the internal resistance. The conductivity field that was obtained with the fluid dynamics model is an important input for this model.
- Important inputs for these two models are the viscosity and conductivity as a function of shear rate. An **experimental method** was developed to determine the viscosity and conductivity with a rheo-impedance setup. Because these measurements do not directly yield the conductivity, an **algorithm** was developed to convert the raw measurement data into a conductivity-shear rate relation.

Figure 1.1 clarifies how the different components of this research are related to each-other.

In previous studies, many numerical models have been developed to describe the fluid dynamics and electrochemical processes flow batteries. The models developed as part of this thesis differ significantly from the models presented in this thesis:

- First of all, it should be noted that models of redox flow batteries cannot be straightforwardly be applied to SSFBs because the electron transport through a sheared carbon black network is different than that through a porous current collector.
- Li *et al.* set up a coupled transport and electrochemical model for an SSFB. The electron flow, reaction kinetics and mass transport are described by a set of equations which is discretised and solved with a finite volume method. Two flow types are modeled: Newtonian Poiseuille flow and plug flow. The electronic conductivity of the suspension is taken to be constant [5].
- A coupled computational fluid dynamics and discrete element method was proposed by Heidarian *et al.* to simulate slurry electrolytes (i.e. water with carbon black particles). While in most other studies the electrolyte is described on a macroscopic level, Heidarian *et al.* model the carbon particles separately. The interactions and charge transfer between carbon black particles determine the electronic conductivity of the slurry. A shortcoming of this model is that the electrolyte is assumed to be a Newtonian fluid [25].
- Most other numerical studies of SSFBs employ a finite element method (using COMSOL Multi-physics software) to solve a system of differential equations for the fluid dynamics and electrochemical behaviour. These models incorporate complex rheological behaviour (e.g., power law fluids), but do not account for a shear rate dependent carbon black conductivity [10][26][27][28].

The models developed in this thesis are capable of simulating a wide range of fluids, including strongly shear thinning fluids that cannot be described by a power law relation. In addition, they implement a conductivity that varies with shear rate.

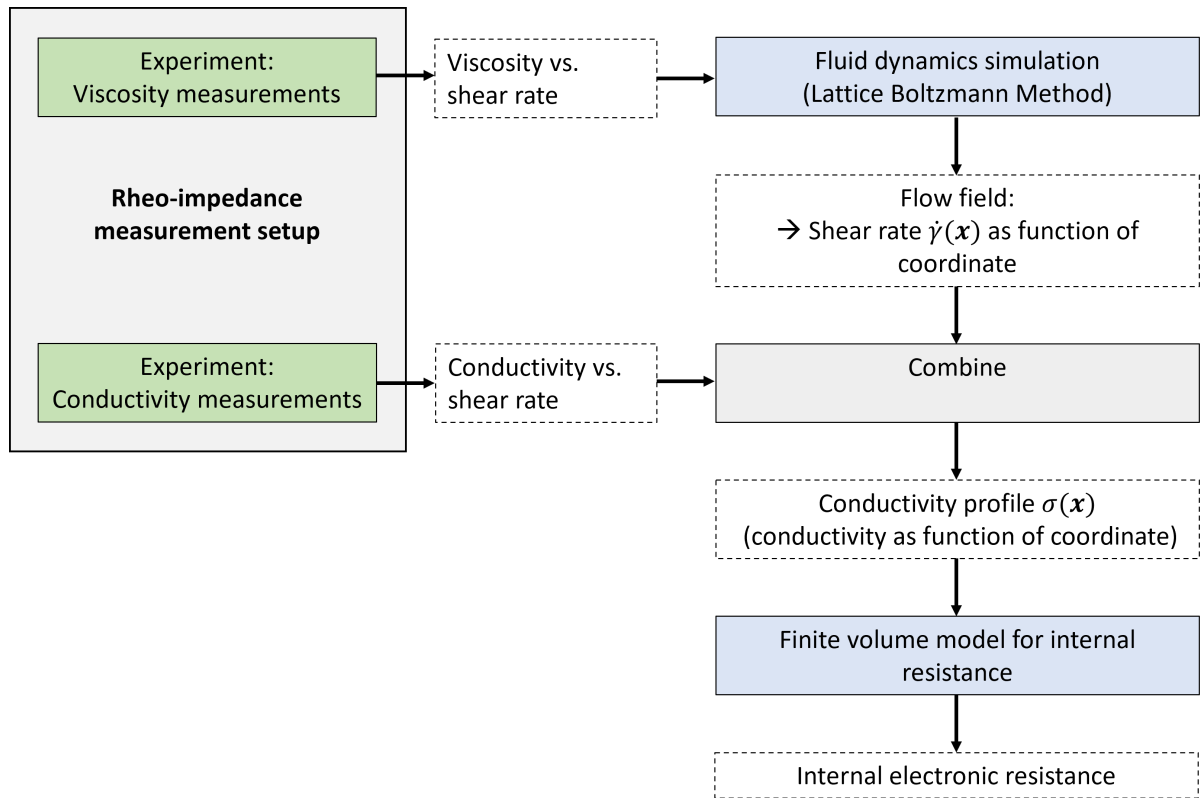


Figure 1.1: Overview of how the different aspects of this research are related to each other.

1.4.2. Thesis Outline

This thesis is structured as follows: first, the theoretical background for this thesis is presented in chapter 2. Subsequently the fluid dynamics model and the electric field model are described in chapter 3 and 4 respectively. Chapter 5 discusses the experimental method for rheo-impedance measurements. The results are presented and discussed in chapter 6. Finally, chapter 7 presents the conclusions and gives recommendations for future research.

2

Theory

Rheological and electrical properties of SSFBs are intertwined. The electronic conductivity depends on the flow behaviour of the electrolyte. Consequently, in order to analyse the internal resistance of SSFBs and its dependency on rheological properties, the fluid dynamics must be characterised first. This chapter explains which battery properties play a role in the internal resistance and how they are related to each other. Furthermore it provides the theoretical framework for a fluid dynamics model and a model for the internal resistance.

First, the working principle and chemistry of the alginate-based SSFB are explained in section 2.1. Subsequently section 2.2 provides a theoretical background in fluid dynamics and introduces the computational method. Then, section 2.3 elaborates on the internal resistance and discusses the numerical method to determine the electronic conductivity of carbon black networks. The electrochemical performance of SSFBs is considered in section 2.4. Finally, section 2.5 discusses the relevant fluid characteristics.

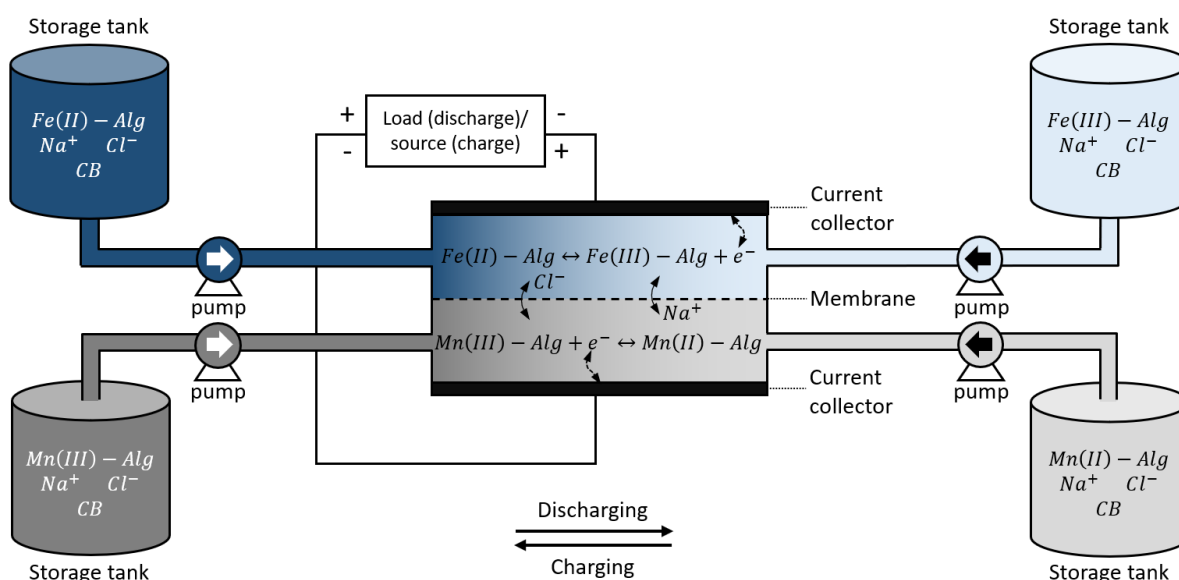


Figure 2.1: Schematic illustration of an SSFB. The electrolytes are stored in separate tanks and pumped through the battery where they are (dis)charged.

2.1. Working Principle of Alginate-based Semi-solid Flow Battery

An SSFB consists of two half cells through which an electrolyte suspension flows. The half cells are separated by a micro filtration membrane. Opposite to the membrane, both half cells are flanked by current collectors. The electrolyte consists of water, active material, carbon black particles, and dissolved ions. A schematic representation of the SSFB is given in figure 2.1. The active material is an alginate hydrogel with redox-active cations. The hydrogel forms bulbs that are too large to pass the membrane. The two half cells contain different redox-active cations, as a result of which a potential difference is induced. A positive redox potential means that the reaction occurs spontaneously when connected to an external circuit. In case of a negative potential on the other hand, the reaction must be driven by an external voltage. In the reaction one of the cations is oxidised releasing an electron, while the other cation receives an electron. The carbon black particles form a conductive pathway for electronic current between the hydrogel bulbs and the current collectors. The external circuit connects the two current collectors. The micro filtration membrane functions as salt bridge. The dissolved ions can easily pass the membrane to preserve electric neutrality in the half cells.

2.1.1. Chemical Composition

Alginates are anionic polysaccharides that occur in brown algae. Together with certain multivalent cations they chelate and form hydrogels [29]. The positively charged cations attract the anionic alginate chains. In this manner they can connect multiple alginate chains to each other. The properties of the gel are mainly governed by the type and number of cations. Different cations have different binding modes with the alginate chains such as the well known 'egg-box' structure [30] or the '3D valent binding structure' [31]. When the cations are chosen appropriately hydrogels can be used as active material in a battery. In this research the cations are iron ($Fe^{2+/3+}$) and Manganese ($Mn^{2+/3+}$) ions. Each ion binds to two anionic (negatively charged) groups at alginate chains. In case of the trivalent ions (Fe^{3+} and Mn^{3+}), a nearby chlorine ion (Cl^-) ensures local neutrality by compensating for the 3rd positive charge. In this early stage of research it is unknown where exactly the chlorine ions are located. A schematic representation of part of a hydrogel with egg-box structures is shown in figure 2.2.

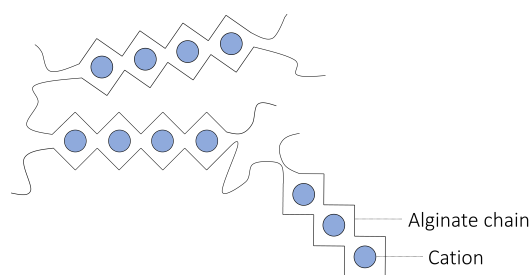
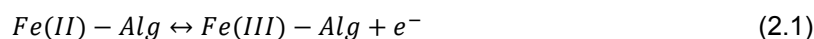
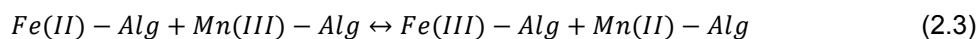


Figure 2.2: Schematic representation of an alginate hydrogel. The alginate chains (represented by black lines) are crosslinked by divalent cations (represented by blue dots).

The reduction and oxidation reactions are given by equations 2.1 and 2.2 respectively.



The reactions have standard reduction potentials of 0.77 V and 1.54 V respectively. The total reaction is given by equation 2.3.



The reaction occurring from left to right has a positive overall potential meaning energy is released in the reaction. This is a discharge reaction. The reaction occurring from right to left, on the other hand, has a negative overall potential and thus absorbs energy. This is a charge reaction.

2.1.2. Electron Transport

During the reaction, the reductant in one half cell loses an electron and the oxidant in the other half cell gains one. Electrons are transferred between the half cells to enable the half reactions. The electronic resistance is the resistance related to the path of the electric current between the locations of the half reactions. It comprises the charge transfer resistance, carbon black resistance and the resistance of the external circuit. The former two are internal resistances. The charge transfer resistance

is the resistance related to the electron transfer between the cation and the carbon black network. It depends on the reaction mechanism, on the local chemical composition of the fluid and on the distance between the carbon black particles and the reacting cation. The carbon black resistance is the ohmic resistance of the carbon black network. As pointed out in section 1.3 carbon black particles cluster and form microstructures. When the carbon black volume fraction is above the percolation threshold, the carbon black particles form networks that span the entire cell, resulting in a considerable conductivity increase. The carbon black conductivity depends on many factors including the size and shape of the microstructures and the composition of the surrounding medium.

Experiments have yielded values of several mS/cm for the electronic conductivity of carbon black networks in aqueous suspensions at rest [5][7]. A study of non-aqueous carbon black suspensions has found values that were at least one order of magnitude lower. Additionally it demonstrated a strong shear rate dependence of carbon black conductivity [12]. This phenomenon is attributed to the shear rate dependent size and shape of the carbon black microstructures. Measurements to evaluate the relation between shear rate and conductivity in aqueous carbon black suspensions have not been performed yet. Nevertheless, since the electronic conduction in aqueous and non-aqueous carbon black suspension is based on the same principles, it is expected that shear rate plays a role in the conductivity of aqueous suspensions too [21][32].

2.1.3. Ion Transport

During operation of the flow battery, ion transfer between the half cells is necessary to conserve charge. Dissolved chlorine (Cl^-) and sodium (Na^+) ions fulfill this role in alginate-based SSBFs. The ionic resistance is the resistance associated with the path of the ions. Ion transport in the electrolyte is described by the Nernst-Planck equation (equation 2.4).

$$\vec{N}_i = z_i \mu_i F c_i \vec{\nabla} \phi - D_i \vec{\nabla} c_i + c_i \vec{u} \quad (2.4)$$

This equation gives the particle flux \vec{N}_i as a function of charge z_i , mobility μ_i , concentration c_i , diffusion coefficient D_i , electric potential ϕ local fluid velocity \vec{u} . F is the Faraday constant. The particles are driven by a potential difference (migration), a concentration gradient (diffusion) and/or the local fluid velocity (convection):

- **Migration** is responsible for the transfer of ions between the half cells. During the reaction, a divalent cation releases an electron and becomes trivalent. To prevent local charge imbalance, a negative chlorine ion moves close to the trivalent cation. In the other half cell the opposite happens and a negative chlorine ion is pushed away by the divalent cation. To preserve global charge neutrality of the half cells, either a positive ion moves from the reduction half cell to the oxidation half cell or a negative ion moves in opposite direction. When moving between the half cells ions pass a micro-filtration membrane. All these processes are driven by electric potential gradients.
- **Diffusion** is the ionic flux due to a concentration gradient. Because the redox reaction neither creates nor absorbs dissolved ions, there are no local concentration gradients within the half cells. The ion transfer between the half cells does however cause a concentration difference between the half cells. This concentration gradient causes a diffusive force that counteracts the electrostatic force for migration. This internal resistance results in a decrease of the operating cell voltage. The loss of potential as a result of the concentration difference ($\Delta\phi_{concentration}$) is given by equation 2.5.

$$\Delta\phi_{concentration} = \frac{RT}{F} \ln\left(\frac{c_A}{c_B}\right) \quad (2.5)$$

In this equation T represents the temperature, R the gas constant, F the Faraday constant and c_A/c_B the ratio of the concentrations in the two half cells [33]. Usually the concentrations are sufficiently high such that the relative concentration difference is small and the resulting internal resistance is negligible.

- **Convection** does not play a role in the transfer of ions between the half cells because the local fluid velocity has no component perpendicular to the membrane.

The electrolyte and the membrane resistance are the main contributors to the ionic resistance. The ionic conductivity in aqueous electrolytes ranges between 50 and 400 mS/cm, depending on aspects such as ionic size, concentration, pressure and temperature [5][34][35][36]. The membrane is a microporous separator which is permeable for solutions (i.e., water with ions) and impermeable for solid particles. It conducts ions and is an insulator for electronic current. Its ionic conductivity depends on many factors including electrolyte composition, pH and temperature. The ionic conductivity of a commercially available microporous membrane in an aqueous 1 M *NaCl* solution was reported to be in the range of 4 mS/cm to 9 mS/cm. Membrane thickness typically ranges from 20 μm to several hundred micrometers [37].

2.2. Fluid Dynamics

A fluid dynamics model is set up to analyse the flow of the electrolyte through the SSFB. There are various different approaches to fluid dynamics. The conventional fluid dynamics approach uses a macroscopic description of the fluid and treats it as a continuum. The presence of individual particles is ignored and macroscopic fluid properties are treated as continuous variables. In this description the motion of fluids is governed by conservation of mass, momentum and energy.

- Conservation of mass is given by the continuity equation:

$$\frac{\partial \rho}{\partial t} + \vec{\nabla} \cdot (\rho \vec{u}) = 0 \quad (2.6)$$

In this equation ρ represents density, t time and \vec{u} velocity.

- Conservation of momentum for incompressible fluids is given by the following equation:

$$\rho \left(\frac{\partial \vec{u}}{\partial t} + (\vec{u} \cdot \vec{\nabla}) \vec{u} \right) = -\vec{\nabla} p + \eta \Delta \vec{u} + \vec{F} \quad (2.7)$$

Here p represents pressure, η dynamic viscosity and \vec{F} external force. The left side of the equation describes the total acceleration and is the sum of local acceleration (due to unsteady flow) and convection. The right side of the equation is the total force exerted and consists of a pressure term, a viscous drag term and an external forcing term.

- Conservation of energy can be described in terms of total energy or in terms of internal energy. Total energy is the sum of a kinetic term for bulk motion ($u^2/2$) and an internal energy term (e). It can be shown that conservation of total energy is equivalent to conservation of internal energy. The internal energy conservation equation is given below [38]:

$$\begin{aligned} \frac{\partial(\rho e)}{\partial t} + \vec{\nabla} \cdot (\rho \vec{u} e) = & -\vec{\nabla} \cdot \vec{q} + \sigma_{xx} \frac{\partial u_x}{\partial x} + \sigma_{yx} \frac{\partial u_x}{\partial y} + \sigma_{zx} \frac{\partial u_x}{\partial z} + \sigma_{xy} \frac{\partial u_x}{\partial y} + \sigma_{yy} \frac{\partial u_x}{\partial y} \\ & + \sigma_{zy} \frac{\partial u_x}{\partial y} + \sigma_{xz} \frac{\partial u_x}{\partial z} + \sigma_{yz} \frac{\partial u_x}{\partial z} + \sigma_{zz} \frac{\partial u_x}{\partial z} \end{aligned} \quad (2.8)$$

In this equation e is the fluid's internal energy, \vec{q} is the heat flux and $\sigma_{\alpha\beta}$ (with $\alpha, \beta \in [x, y, z]$) are the components of the stress tensor.

In addition to the conservation equations, an equation of state is needed to close the system. The equation of state relates local thermodynamic state variables (temperature, pressure, density, internal energy, entropy) to each other. Due to the convection term in the Navier-Stokes equation the system of equations is nonlinear and hence hard to solve analytically [38].

An alternative to the continuum fluid dynamics approach is to treat fluids as a collection of particles. Such descriptions avoid the nonlinear Navier-Stokes equation by calculating the dynamics of each particle individually. Microscopic particle based descriptions treat individual molecules separately using Newton's dynamics whereas mesoscopic particle based descriptions of fluids track collections of particles via for example kinetic theory. Kinetic theory forms the basis for the Lattice Boltzmann method.

2.2.1. Kinetic Theory

Kinetic theory is a mesoscopic representation of fluids that tracks collections of molecules via a particle distribution function [38]. The particle distribution function $f(\vec{x}, \vec{u}, t)$ represents the density of particles with velocity \vec{u} at position \vec{x} and time t . The particles move with a certain velocity and interact with each other via collisions. The Boltzmann equation 2.9 governs the evolution of the distribution function. It captures both what happens in collisions and in between collisions.

$$\frac{\partial f}{\partial t} + \vec{u} \cdot \vec{\nabla} f + \frac{\vec{F}}{\rho} \vec{\nabla}_{\vec{u}} f = \Omega(f) \quad (2.9)$$

In this equation F is the body force, ρ is the density and $\Omega(f)$ is a source term called the collision operator. In each collision, the collision operator brings the distribution function towards a local equilibrium while conserving mass, momentum and energy. The particle distribution function is related to macroscopic quantities such as velocity and density. As an example, the macroscopic density is the integral of the particle distribution function over velocity space (equation 2.10).

$$\rho(\vec{x}, t) = \iiint f(\vec{x}, \vec{u}, t) d^3 \vec{u} \quad (2.10)$$

Via the Chapman-Enskog analysis it can be shown that the macroscopic fluid dynamics equations can be derived from the Boltzmann equation. This means that kinetic theory is capable of describing the macroscopic behaviour of fluids [38].

2.2.2. Computational Fluid Dynamics

Generally, fluid dynamics problems are hard to solve analytically, even in case of simple problems. In many cases numerical solution methods are preferred. Computational fluid dynamics (CFD) solves fluid dynamics problems numerically with the help of computers. Conventional numerical fluid simulation methods use the macroscopic picture and treat fluids as a continuum governed by discretised versions of the continuity, Navier-Stokes and energy equation. Since this system of equations is nonlinear, complicated iterative schemes are needed and approximation errors are inevitable. Particle based fluid simulation methods on the other hand, do not solve the fluid mechanics equations directly but calculate the behaviour of particles that make up the fluid. These particles represent individual molecules (microscopic picture) or collections of many molecules (mesoscopic picture). A common difficulty in particle based fluid simulations is bridging the gap between the particle picture and the macroscopic picture of the fluid. For this reason, microscopic particle based simulations typically are not suitable for CFD. As mentioned in section 2.2.1 kinetic theory is connected to the macroscopic fluid dynamics equations and hence capable of describing macroscopic fluid behaviour. Therefore, the lattice Boltzmann method, a numerical method which stems from kinetic theory, is suitable for CFD simulations. In this research the lattice Boltzmann method is used to simulate the flow of the electrolyte through the SSFB [38].

2.2.3. Lattice Boltzmann Method

The lattice Boltzmann method (LBM) has its origin in kinetic theory and cellular automata and describes fluids via a particle distribution function. While kinetic theory uses a continuous distribution function, LBM reduces the degrees of freedom by discretising time, coordinate space and velocity space. Velocity space is discretised by defining a small set of velocity vectors $\{\vec{c}_i\}$ and corresponding weights $\{w_i\}$. Particles are restricted to this velocity set, meaning they cannot move in any other direction. The discrete particle distribution function $f_i(\vec{x}, t)$ represents the density of particles at position \vec{x} that have velocity \vec{c}_i at time t . A discretised form of the Boltzmann equation, the lattice Boltzmann equation (equation 2.11), governs the evolution of the discrete particle distribution function.

$$f_i(\vec{x} + \vec{c}_i \Delta t, t + \Delta t) = f_i(\vec{x}, t) + \Omega_i(\vec{x}, t) \quad (2.11)$$

In this equation $\Omega_i(\vec{x}, t)$ is the discretised collision operator. The distribution function is related to macroscopic variables like density and velocity through its moments:

$$\rho(\vec{x}, t) = \sum_i f_i(\vec{x}, t), \quad \vec{u}(\vec{x}, t) = \frac{\sum_i \vec{c}_i f_i(\vec{x}, t)}{\rho(\vec{x}, t)} \quad (2.12)$$

In LBM the pressure is proportional to the density as given in equation 2.13. The proportionality constant is the speed of sound (c_s) squared.

$$p = \rho c_s^2 \quad (2.13)$$

Velocity Sets

The velocity set characterises the discretisation of velocity space. It is specified by 2 numbers labeled D and Q. The former gives the number of spatial dimensions and the latter the amount of velocity directions. As an example, the D2Q9 velocity set is a commonly used set for lattice Boltzmann models in two dimensions. It has 9 velocities (illustrated in figure 2.3) with corresponding weights given by: $w_0 = \frac{4}{9}$, $w_{1,2,3,4} = \frac{1}{9}$ and $w_{5,6,7,8} = \frac{1}{36}$.

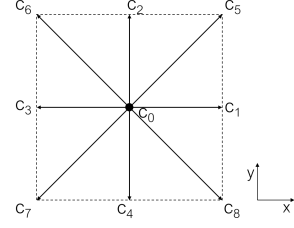


Figure 2.3: D2Q9 velocity set. The particles are restricted to these 9 velocities.

Algorithm

LBM uses an iterative algorithm that updates the particle distribution function every iteration until it has reached an equilibrium. Each iteration consists of 2 steps: collision and streaming. Each time step the particles collide, meaning that particles at time t and coordinate \vec{x} are redistributed among the velocities \vec{c}_i (i.e. the particles stay at location \vec{x} and get a different direction). Mass, momentum and energy are conserved in collisions. In between collisions, particles stream with velocity \vec{c}_k from lattice point \vec{x} towards the neighbouring lattice point located at $\vec{x} + \vec{c}_k \Delta t$. Collision and streaming are depicted in figure 2.4 for the D2Q9 velocity set.

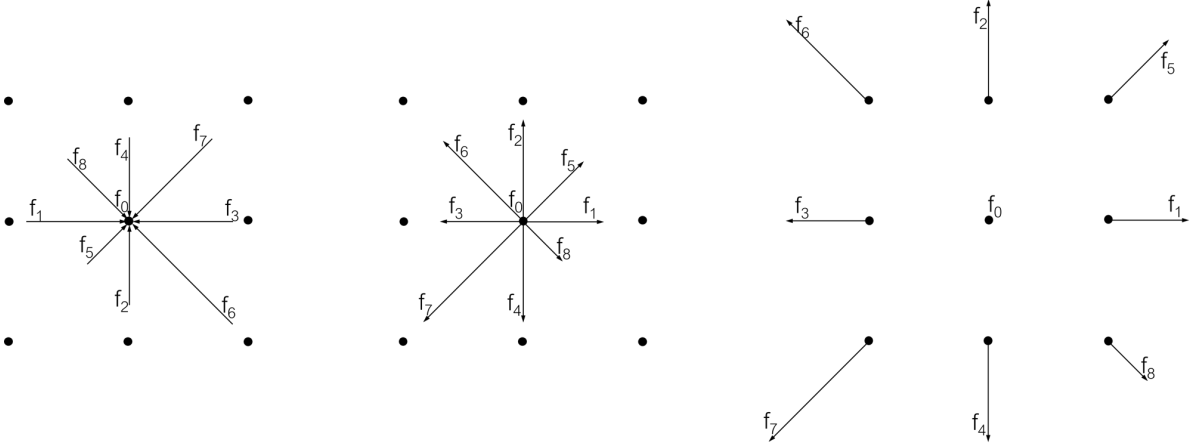


Figure 2.4: Particles collide and are redistributed over the velocities. After collision the particles stream from their lattice point to neighbouring lattice points. Collision and streaming occur at each lattice point. Left: Initial distribution. Center: Distribution after collision. Right: Distribution after streaming step.

Collision Operators

Collisions are modeled by applying a collision operator. It brings the distribution function towards a local equilibrium and conserves mass, momentum and energy. There are multiple collision operators, each with its own (dis)advantages. The preferred choice of operator depends on the details of the simulation.

- The simplest operator is the **Bhatnagar-Gross-Krook (BGK)** operator:

$$\Omega_i(f) = -\frac{f_i - f_i^{eq}}{\tau} \Delta t \quad (2.14)$$

This operator brings the distribution function towards a local equilibrium f_i^{eq} on a timescale defined by relaxation time τ . The relaxation time has a lower and upper bound for stability and accuracy reasons and is directly related to kinematic viscosity ν via equation 2.15. (The kinematic viscosity is the dynamic viscosity η divided by the density ρ .)

$$\nu = c_s^2 \left(\tau - \frac{\Delta t}{2} \right) \quad (2.15)$$

Therefore, the BGK poses limitations on the viscosity: high viscosities result in reduced accuracy and low viscosities lead to instabilities.

- The **multiple-relaxation-time (MRT)** operator is a matrix with multiple different relaxation times. Owing to the fact that it has much more free parameters to tune, a wider viscosity range can be used. This comes at the cost of increased computational time [38].
- Alternatively, the **filter matrix lattice Boltzmann method (FMLB)** can be used. Unlike the BGK and MRT schemes, it uses a nonlinear collision operator. Like the MRT collision operator, the FMLB method allows for a wide viscosity range, but comes at the cost of increased computational time [39].

Chapter 3 explains how LBM is implemented for a fluid dynamics model of the SSFB.

2.2.4. Pumping Power

During charging and discharging, the electrolyte suspensions are pumped through the battery half cells. Friction at the walls causes loss of energy. To compensate for wall friction the flow is driven by a pump. The energy loss as a result of friction limits the overall energy efficiency of the battery. Hence, for an efficient flow battery, the power lost in pumping must be minimized. The pumping power depends on fluid properties (viscosity and density), on flow velocity and on the geometry of the channel.

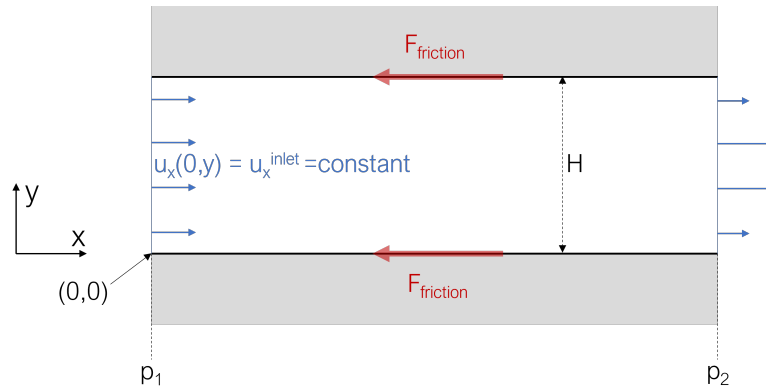


Figure 2.5: Schematic illustration of flow through a two dimensional rectangular channel with height H . The inlet velocity u_x^{inlet} is uniform. The flow is driven by a pressure gradient ($p_1 - p_2$) and slowed down by wall friction. These two forces compensate each other.

The pump applies a pressure difference between the in- and outlet ($p_1 - p_2$), which compensates for the friction force such that the net force acting on the fluid is zero. In case of a two dimensional parallel plate flow as depicted in figure 2.5, both forces act in x-direction such that:

$$\sum_i F_x^i = A(p_1 - p_2) - F_{friction} = 0 \quad (2.16)$$

The wall friction can be calculated from the CFD simulation output in two different ways, which should yield the same result.

1. Rewriting equation 2.16 gives a direct relation between the pressure difference and the friction force:

$$F_{friction} = A(p_1 - p_2) = F_{pressure} \quad (2.17)$$

In which p_1 and p_2 are the in- and outlet pressure respectively and A is the cross sectional area of the channel. For the two dimensional flow channel of figure 2.5 $A = H$.

2. Alternatively, the wall friction can be computed by integrating over the shear stress at the walls. For the two dimensional rectangular channel the wall friction force is given by equation 2.18.

$$F_{friction} = F_{shear} = \int_{upper\ wall} \tau(x, y = H) dx + \int_{lower\ wall} \tau(x, y = 0) dx \quad (2.18)$$

The pumping power is the product of inlet velocity and wall friction force as given in equation 2.19.

$$P_{pumping} = F_{friction} u_x^{inlet} \quad (2.19)$$

Where $u_x^{inlet} = u(x = 0) \neq f(y)$ is a uniform inlet velocity.

2.3. Internal Resistance

The aim of this thesis is to determine the internal electrical resistance in alginate-based SSFBs and evaluate its dependence on the rheology. The internal resistance is the sum of the carbon black electronic resistance, the charge transfer resistance, the electrolyte ionic resistance and the membrane ionic resistance. These components can be computed independently. Most likely, the carbon black resistance is the only component that depends on the flow characteristics. Therefore this research mainly focuses on the carbon black resistance. Its internal electronic resistance is determined by the conductivity of the medium and by the path of the electrons:

- **Conductivity:** As touched upon in section 2.1.2, the conductivity of carbon black networks depends on shear rate. As shear rate in the flow channel varies with location, the conductivity in the flow channel is a local variable ($\sigma(\vec{r})$). The CFD model computes the shear rate in the flow channel ($\dot{\gamma}(\vec{r})$). Combining this with experimental data for the electronic conductivity as a function of shear rate ($\sigma(\dot{\gamma})$) gives the conductivity in the flow channel (i.e. $\sigma(\vec{r})$).
- **Location of reaction:** The longer the path of the electrons, the higher its resistance. Therefore the location of the reactions influences the internal resistance. Ideally, when computing the internal resistance, the location of the reactions is taken into account. In principle reactions could take place in any alginate bulb (i.e. anywhere in the flow channel). It is expected that reactions with a lower total resistance (i.e. combination of ionic, electronic and external resistance) are more likely to occur. Describing this requires a complex model that incorporates fluid dynamics, mass transfer and electrochemistry. Due to a lack of information it is at this stage impossible to set up such a model. (Section 2.4 elaborates on what information is necessary for setting up an electrochemical performance model.)

In this research a simplified approach is taken to analyse the flow dependence of the carbon black resistance. The flow channel is represented as a cuboidal conductor with a stationary, inhomogeneous conductivity $\sigma(\vec{r})$. The carbon black electronic resistance of the channel is computed by applying a voltage V_{ext} over the channel and dividing it by the resulting total current I (equation 2.20).

$$R = \frac{V_{ext}}{I} \quad (2.20)$$

While this representation of the situation disregards the varying location of reactions (all reactions are assumed to occur close to the membrane), it still provides valuable insights about the flow dependence of the carbon black resistance.

The current through an inhomogeneous conductor can be derived from the electric potential field $V(\vec{r})$. The electric potential in a conductor is governed by the following set of equations [40]:

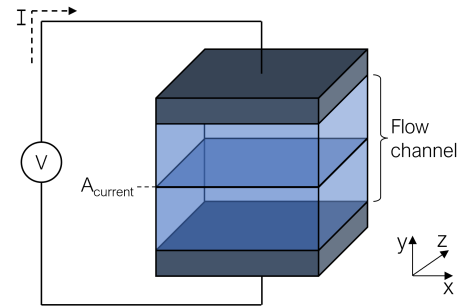


Figure 2.6: Schematic illustration of flow channel as a cuboidal conductor (blue). A voltage V_{ext} is applied over the conductor, as a result of which a current I flows through the conductor. $A_{current}$ is the cross sectional area of the conductor.

- Electric field (\vec{E}) and electric potential V :

$$\vec{E} = -\vec{\nabla}V \quad (2.21)$$

- Electric current density \vec{j} :

$$\vec{\nabla} \cdot \vec{j} = -\frac{\partial \rho_c(\vec{r}, t)}{\partial t} \quad (2.22)$$

Where $\rho_c(\vec{r}, t)$ is the charge density. In case of a stationary situation this simplifies to:

$$\vec{\nabla} \cdot \vec{j} = 0 \quad (2.23)$$

- Relation between current density and electric field (Ohm's law):

$$\vec{j}(\vec{r}) = \sigma(\vec{r}) \vec{E}(\vec{r}) \quad (2.24)$$

Where $\sigma(\vec{r})$ is the conductivity.

Combining these equations leads to a differential equation for the electric potential:

$$0 = -\vec{\nabla} \cdot \vec{j} = \vec{\nabla} \cdot \sigma \vec{\nabla}V \quad (2.25)$$

Chapter 4 discusses the implementation of a finite volume model to solve equation 2.25 for the electric potential. Once the electric field is computed, the internal resistance can be derived in the following manner:

- Combining equations 2.21 and 2.24 leads to an equation for the current density as a function of electric potential:

$$\vec{j} = \sigma \vec{\nabla}V \quad (2.26)$$

- Integration of current density \vec{j} over the full cross sectional area $A_{current}$ (see figure 2.6) of the conductor gives the current I flowing through the conductor.
- The internal resistance is computed by dividing the applied voltage by the current through the conductor (equation 2.20).

2.4. Electrochemical Performance

To evaluate the electrochemical performance of SSFBs a combined fluid dynamics, particle transport and electrochemical model is needed. In literature, many electrochemical models for similar systems (both RFBs and SSFBs with different chemical compositions) use COMSOL Multiphysics to solve a system of equations numerically. The cornerstones of such simulations are listed below [5][10][26][27][28]:

- The fluid dynamics is governed by the Navier-Stokes equation. Alternatively a lattice Boltzmann or other CFD model can be used.
- The electric potential ($\phi_s(V)$) and electronic current density ($\vec{j}_s(A/m^2)$) in solid particles are described by Ohm's law (equation 2.27).

$$\vec{j}_s = -\sigma_s \vec{\nabla} \phi_s \quad (2.27)$$

Where σ_s represents electronic conductivity of the particles (S/m). (ϕ_s is equivalent to V in equation 2.21.)

- The chemical reaction acts as a source term for the electric current:

$$\vec{\nabla} \cdot (\sigma_s \vec{\nabla} \phi_s) = F a_s j_n \quad (2.28)$$

Where F is the Faraday constant ($C \text{ mol}^{-1}$), a_s the specific active surface area (m^{-1}) and j_n the reaction rate per unit active area ($\text{mol m}^{-2} \text{ s}^{-1}$).

- The reaction kinetics are described by the Butler-Volmer equation.

$$j_n = \frac{i_0}{nF} \left(\exp\left(\frac{\alpha nF\eta}{RT}\right) - \exp\left(\frac{(1-\alpha)nF\eta}{RT}\right) \right) \quad (2.29)$$

Where j_n is the reaction rate per unit active area ($\text{mol m}^{-2} \text{s}^{-1}$), i_0 the exchange current density (A/m^2), η the activation overpotential (V), n the number of electrons per reaction, α the charge transfer coefficient, T the temperature (K) and R the universal gas constant ($\text{K}^{-1} \text{mol}^{-1}$). The activation overpotential depends on the state of charge and on the materials.

- Electrolyte potential, ionic concentrations (in intercalation particles and the electrolyte) are governed by the Nernst-Planck equation, and by mass and charge conservation.

As pointed out in section 1.4.1 these models cannot straightforwardly be applied to the alginate-based electrolyte with carbon black particles. Some major issues with these models and potential ways to resolve them are listed below:

- In previous studies the electrolyte was assumed to have a simple rheology such as Newtonian, power law or plug flow [5][10][26][27][28]. The alginate-based carbon black electrolyte has a more complex viscosity-shear rate relation [21]. The viscosity-shear rate relation must therefore be determined experimentally and incorporated in the fluid dynamics model.
- As the carbon black conductivity is a function of shear rate, it is not constant throughout the channel [22]. It must therefore be implemented as a local variable. Alternatively, a coupled CFD discrete element method could be used to model the interactions and charge transfer between separate carbon black particles as was done by Heidarian *et al.* [25].
- The reaction kinetics of $Fe - Alg$ and $Mn - Alg$ are largely unknown. Variables such as the activation overpotential and exchange current density depend on many aspects including chemical composition, ionic concentrations and electrode structure. These have to be quantified and incorporated in the electrochemical model.
- The charge transfer resistance, i.e. the resistance related to electron transfer between alginate bulb and carbon black, is unknown.

To summarize, it is, mainly due to a lack of information, currently impossible to set up a comprehensive electrochemical-transport model. In this research a simplified approach is taken by combining a lattice Boltzmann fluid dynamics model with a finite volume model for internal resistance.

2.5. Fluid Characteristics

The alginate-based electrolyte with dispersed carbon black particles has not been characterised yet. Its viscosity and conductivity, which are both functions of shear rate, are unknown. The models that are developed in this research must therefore be applicable to a wide range of fluids such that they are likely to be capable of simulating the alginate-based electrolyte too. In this research, the LBM model is tested on 3 benchmark fluids: Newtonian, shear thickening and shear thinning. Additionally, to get a first indication of the flow behaviour and internal resistance of the alginate-based electrolyte, a comparable fluid, whose viscosity and conductivity are known, is analysed. This fluid is a non-aqueous carbon black suspension containing 2.1 Vol-% Ketjen Black dispersed in 1M Lithium bis(trifluoromethanesulfonyl)imide in propylene carbonate. This section discusses its electrical and rheological properties.

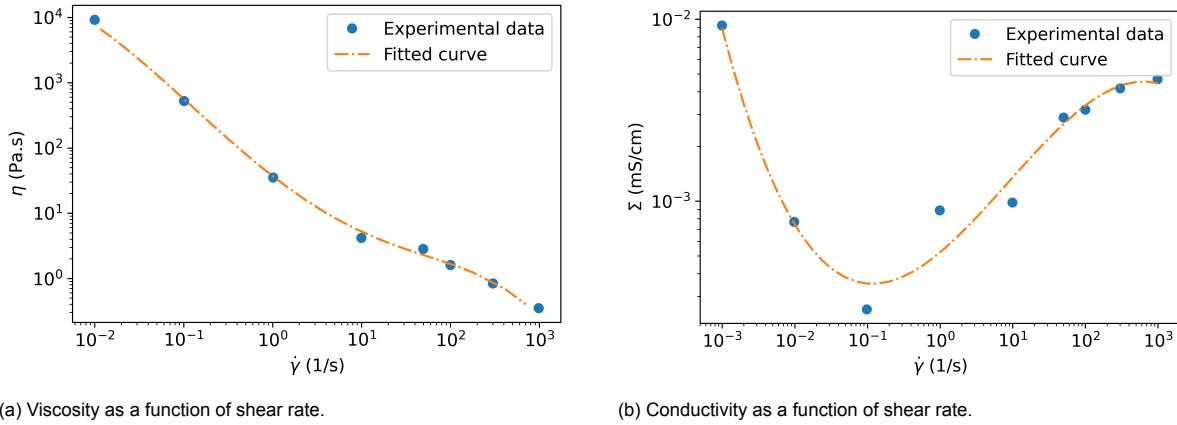
The dynamic viscosity and conductivity have been determined experimentally by Youssry *et al.* [22]. To obtain continuous functions of shear rate for the viscosity and conductivity, curves were fit to the experimental data. Figure 2.7 shows the results of the fit along with the experimental data. The fitted curves are given by equations 2.30 and 2.31.

$$\eta_{fit}(\dot{\gamma}) = \exp(q_0\dot{\gamma}^5 + q_1\dot{\gamma}^4 + q_2\dot{\gamma}^3 + q_3\dot{\gamma}^2 + q_4\dot{\gamma} + q_5) \quad (2.30)$$

with coefficients $q_0 = -9.873 \times 10^{-5}$, $q_1 = -0.001251$, $q_2 = 0.009049$, $q_3 = 0.07908$, $q_4 = -1.063$, $q_5 = 3.614$ and units $[\eta_{fit}] = \text{Pa} \cdot \text{s}$, $[\dot{\gamma}] = \text{s}^{-1}$.

$$\sigma_{fit}(\dot{\gamma}) = \exp(p_0\dot{\gamma}^3 + p_1\dot{\gamma}^2 + p_2\dot{\gamma} + p_3) \quad (2.31)$$

with coefficients $p_0 = -0.008\,069\,6$, $p_1 = 0.052\,177\,17$, $p_2 = 0.334\,445\,89$, $p_3 = -7.555\,960\,85$ and units $[\sigma_{fit}] = mS \cdot cm^{-1}$, $[\dot{\gamma}] = s^{-1}$.



(a) Viscosity as a function of shear rate.

(b) Conductivity as a function of shear rate.

Figure 2.7: Rheological and electrical characterisation of carbon black suspension. The experimental results (blue dots) are plotted along with the fitted curves (orange dashed lines).

Because it is hard to predict the viscosity and conductivity outside the experimental shear rate range, both are assumed to be constant and continuous. Section 6.3.4 elaborates on the effect of these cutoff values.

$$\sigma(\dot{\gamma}) = \begin{cases} \sigma_{fit}(\dot{\gamma} = 1 \times 10^{-3}) & \dot{\gamma} \leq 1 \times 10^{-3} \text{ s}^{-1} \\ \sigma_{fit}(\dot{\gamma}) & \dot{\gamma} > 1 \times 10^{-3} \text{ s}^{-1} \\ \sigma_{fit}(\dot{\gamma} = 9.8 \times 10^2) & \dot{\gamma} \leq 9.8 \times 10^2 \text{ s}^{-1} \end{cases} \quad (2.32)$$

$$\eta(\dot{\gamma}) = \begin{cases} \eta_{fit}(\dot{\gamma} = 1 \times 10^{-2}) & \dot{\gamma} \leq 1 \times 10^{-2} \text{ s}^{-1} \\ \eta_{fit}(\dot{\gamma}) & \dot{\gamma} > 1 \times 10^{-2} \text{ s}^{-1} \\ \eta_{fit}(\dot{\gamma} = 7 \times 10^2) & \dot{\gamma} \leq 7 \times 10^2 \text{ s}^{-1} \end{cases} \quad (2.33)$$

It should be noted that the alginate-based electrolyte has a different composition than the carbon black suspension presented here. It is therefore likely that its viscosity and conductivity as a function of shear rate differ from the functions presented here. Chapter 5 describes an experimental method for viscosity and conductivity measurements.

3

Description of Fluid Dynamics Model

This chapter describes the implementation of the lattice Boltzmann method for a fluid dynamics model of the flow battery. Alginate-based electrolyte suspensions are non-Newtonian, meaning their viscosity depends on the shear rate. Consequently, viscosity is a function of position and time and has to be updated each time step. In previous studies the MRT and FMLB performed better in terms of stability (and in some cases accuracy) than methods using the BGK operator [41][39][42]. Especially at low viscosities the BGK experiences issues with stability [38][42]. The MRT and FMLB are therefore chosen in this research for the simulation of fluids with varying viscosities. Two models are developed: one based on the MRT collision operator and the other one employing the FMLB method. The models are otherwise identical which allows to compare them. Sections 3.1 and 3.2 elaborate on MRT and FMLB model respectively. Subsequently the geometry of the model is explained in section 3.3 followed by a discussion of the boundary conditions in section 3.4.

3.1. Multiple Relaxation Time Lattice Boltzmann Method

The idea behind the MRT collision operator is to use multiple relaxation times instead of one. As a result it has more free parameters that can be tuned to achieve stability. Collisions take place in moment space and are described by equation 3.1 [38][43].

$$f(\vec{x} + \vec{c}_i \Delta t, t + \Delta t) - f(\vec{x}, t) = -\mathbf{M}^{-1} \mathbf{S} \mathbf{M} (f(\vec{x}, t) - f^{eq}(\vec{x}, t)) \Delta t \quad (3.1)$$

There are multiple options for transformation matrix M and relaxation matrix S . In this research the Gram-Schmidt transformation matrix and corresponding relaxation matrix were used. For the D2Q9 velocity set the matrices are given by equations 3.2 and 3.3 [38].

$$\mathbf{M} = \begin{pmatrix} 1 & 1 & 1 & 1 & 1 & 1 & 1 & 1 & 1 \\ -4 & -1 & -1 & -1 & -1 & 2 & 2 & 2 & 2 \\ 4 & -2 & -2 & -2 & -2 & 1 & 1 & 1 & 1 \\ 0 & 1 & 0 & -1 & 0 & 1 & -1 & -1 & 1 \\ 0 & -2 & 0 & 2 & 0 & 1 & -1 & -1 & 1 \\ 0 & 0 & 1 & 0 & -1 & 1 & 1 & -1 & -1 \\ 0 & 0 & -2 & 0 & 2 & 1 & 1 & -1 & -1 \\ 0 & 1 & -1 & 1 & -1 & 0 & 0 & 0 & 0 \\ 0 & 0 & 0 & 0 & 0 & 1 & -1 & 1 & -1 \end{pmatrix} \quad (3.2)$$

$$\mathbf{S}(\vec{x}, t) = \begin{pmatrix} s_0 & 0 & 0 & 0 & 0 & 0 & 0 & 0 & 0 \\ 0 & s_1 & 0 & 0 & 0 & 0 & 0 & 0 & 0 \\ 0 & 0 & s_2 & 0 & 0 & 0 & 0 & 0 & 0 \\ 0 & 0 & 0 & s_3 & 0 & 0 & 0 & 0 & 0 \\ 0 & 0 & 0 & 0 & s_4 & 0 & 0 & 0 & 0 \\ 0 & 0 & 0 & 0 & 0 & s_5 & 0 & 0 & 0 \\ 0 & 0 & 0 & 0 & 0 & 0 & s_6 & 0 & 0 \\ 0 & 0 & 0 & 0 & 0 & 0 & 0 & s_7 & 0 \\ 0 & 0 & 0 & 0 & 0 & 0 & 0 & 0 & s_8 \end{pmatrix} \quad (3.3)$$

Symbols $s_0 - s_8$ represent the relaxation rates, where s_7 and s_8 are directly related to the viscosity. In simulations of non-Newtonian fluids the viscosity varies over the computational domain and \mathbf{S} is a function of time and place.

When taking a closer look at equation 3.1 the collision can be divided into 3 steps:

- The populations are transformed from velocity (f_i) to moment space (m_k) through matrix multiplication with matrix \mathbf{M}
- Each moment m_k is relaxed towards its equilibrium value at relaxation rate s_k . This is the equivalent to matrix multiplication with diagonal matrix \mathbf{S} .
- The post-collision moments are transformed back through matrix multiplication with \mathbf{M}^{-1}

The Numerical procedure for the MRT Lattice Boltzmann methods for the D2Q9 velocity set, in absence of external forces is given below [38]:

1. Initialization:

- Initial values are chosen for the density, velocity and kinematic viscosity of the fluid.
- Particle distribution function is calculated based on the initial values for density and velocity:

$$f_i(\vec{x}) = f_i^{eq}(\vec{x}) = w_i \rho(\vec{x}) \left(1 + \frac{\vec{c}_i \cdot \vec{u}(\vec{x})}{c_s^2} + \frac{(\vec{c}_i \cdot \vec{u}(\vec{x}))^2}{2c_s^4} - \frac{\vec{u}(\vec{x}) \cdot \vec{u}(\vec{x})}{2c_s^2} \right) \quad (3.4)$$

- Relaxation rates are set as: $s_0 = s_3 = s_5 = 0$, $s_1 = 1.1$, $s_2 = 1.0$, $s_4 = s_6 = 1.2$, $s_7 = s_8 = (\tau(\vec{x}))^{-1} = \frac{\Delta t + 6\nu(\vec{x})}{2}$ [44]. Here $\nu(\vec{x})$ is the initial kinematic viscosity.

2. Computation of **density and velocity** via the conserved moments of the particle distribution function:

$$\rho(\vec{x}) = \sum_i f_i(\vec{x}), \quad \vec{u}(\vec{x}) = \frac{\sum_i \vec{c}_i f_i(\vec{x})}{\rho(\vec{x})} \quad (3.5)$$

3. Computation of **equilibrium particle distribution function**:

$$f_i^{eq}(\vec{x}) = w_i \rho(\vec{x}) \left(1 + \frac{\vec{c}_i \cdot \vec{u}(\vec{x})}{c_s^2} + \frac{(\vec{c}_i \cdot \vec{u}(\vec{x}))^2}{2c_s^4} - \frac{\vec{u}(\vec{x}) \cdot \vec{u}(\vec{x})}{2c_s^2} \right) \quad (3.6)$$

4. Transformation to **moment space**: The populations are transformed from velocity space to moment space by matrix multiplication.

$$m_k(\vec{x}) = \sum_{i=0}^8 M_{ki} f_i(\vec{x}), \quad m_k^{eq}(\vec{x}) = \sum_{i=0}^8 M_{ki} f_i^{eq}(\vec{x}) \quad (3.7)$$

The resulting moments $m_k(\vec{x})$ and $m_k^{eq}(\vec{x})$ have, like the populations in velocity space $f_i(\vec{x})$, 9 components (denoted by k) and are coordinate dependent.

5. Computation of **shear rate and kinematic viscosity**. The components of the strain rate tensor ϵ_{xy} , ϵ_{yx} , ϵ_{xx} , ϵ_{yy} are given by equation 3.8 [44]:

$$\epsilon_{\alpha\beta}(\vec{x}) = -\frac{1}{2\rho(\vec{x})c_s^2\Delta t} \sum_{i=0}^8 \sum_{j=0}^8 c_i^\alpha c_j^\beta (\mathbf{M}^{-1}\mathbf{S}(\vec{x})\mathbf{M})_{ij} (f_j(\vec{x}) - f_j^{eq}(\vec{x})) \quad (3.8)$$

The shear rate follows from the strain rate tensor [44]:

$$\dot{\gamma}(\vec{x}) = \sqrt{2(\epsilon_{xy}(\vec{x})^2 + \epsilon_{yx}(\vec{x})^2 + \epsilon_{xx}(\vec{x})^2 + \epsilon_{yy}(\vec{x})^2)} \quad (3.9)$$

Using $\epsilon_{xy}(\vec{x}) = \epsilon_{yx}(\vec{x})$ (as can be seen in equation 3.8) this simplifies to:

$$\dot{\gamma}(\vec{x}) = \sqrt{2 \left(2\epsilon_{xy}(\vec{x})^2 + \epsilon_{xx}(\vec{x})^2 + \epsilon_{yy}(\vec{x})^2 \right)} \quad (3.10)$$

If the kinematic viscosity is a function of shear rate it is updated accordingly. E.g. for a power law fluid:

$$\nu(\dot{\gamma}(\vec{x})) = \frac{K}{\rho(\vec{x})} (\dot{\gamma}(\vec{x}))^{n-1} \quad (3.11)$$

Where K is the fluid consistency coefficient with a unit of $\text{kg s}^{n-2} \text{m}^{-1}$, and n is the dimensionless power law index [44]. For fluids with more complex shear behaviour a curve fit to experimental viscosity-shear rate data is used to compute the new viscosity.

6. **Relaxation matrix update:** Relaxation rates s_7 and s_8 are directly related to the kinematic viscosity.

$$s_7(\vec{x}) = s_8(\vec{x}) = \frac{2}{\Delta t + 6\nu(\vec{x})} \quad (3.12)$$

Using this equation, relaxation matrix \mathbf{S} is updated.

7. **Collision** takes place in moment space. The moments m_k are relaxed towards the equilibrium moments m_k^{eq} at a pace determined by the relaxation rate s_k , $k \in [0, 1, 2, 3, 4, 5, 6, 7, 8]$.

$$m_k^{new}(\vec{x}) = m_k(\vec{x}) - s_k(\vec{x}) (m_k(\vec{x}) - m_k^{eq}(\vec{x})) \quad (3.13)$$

8. Transformation to **velocity space:** The new moments are transformed back to velocity space via a multiplication with inverse matrix \mathbf{M}^{-1} .

$$f_i^{new}(\vec{x}) = \sum_{k=0}^8 M_{ik}^{-1} m_k^{new}(\vec{x}) \quad (3.14)$$

9. **Streaming:** All particles with velocity \vec{c}_i move from lattice point \vec{x} to neighbouring lattice point $\vec{x} + \vec{c}_i \Delta t$ resulting in a new particle distribution function: $f_i(\vec{x} + \vec{c}_i \Delta t, t + \Delta t)$. Boundary conditions are applied along the edge of the simulation domain. Section 3.4 elaborates on the boundary conditions.

The post-streaming particle distribution function is the starting point for the next time step.

10. Step 2 to 9 are **repeated until convergence**.

3.2. Filter Matrix Lattice Boltzmann Method

The FMLB was originally proposed by Somers [45] in 1993 and has been improved and extended amongst others by Zhuo *et al.* [39]. In FMLB, the lattice boltzmann equation (equation 3.15) is defined on a staggered coordinate-time grid and contains a nonlinear collision operator $\Omega_i(f)$.

$$\frac{f_i\left(\vec{x} + \frac{\vec{c}_i \Delta t}{2}, t + \frac{\Delta t}{2}\right) - f_i\left(\vec{x} - \frac{\vec{c}_i \Delta t}{2}, t - \frac{\Delta t}{2}\right)}{\Delta t} = \Omega_i(f) \quad (3.15)$$

The Boltzmann equation (equation 2.9) is obtained by second order Taylor expansion of the FMLB lattice Boltzmann equation. First order Taylor-expansion of equation 3.15 in combination with Boltzmann equation 2.9 leads to an expression for $f_i\left(\vec{x} \pm \frac{\vec{c}_i \Delta t}{2}, t \pm \frac{\Delta t}{2}\right)$ as a function of $f_i(\vec{x}, t)$ and the collision operator.

$$f_i\left(\vec{x} \pm \frac{\vec{c}_i \Delta t}{2}, t \pm \frac{\Delta t}{2}\right) = f_i(\vec{x}, t) \pm \frac{\Delta t}{2} \Omega_i(f) \quad (3.16)$$

This equation can be solved using a reversible filter matrix E_{ki} and corresponding solution vector α_k^\pm . The solution vector is defined as the matrix multiplication of E_{ki} with particle distribution function f_i .

$$\alpha_k^\pm(\vec{x}) = \sum_i E_{ki} f_i\left(\vec{x} \pm \frac{\vec{c}_i \Delta t}{2}, t \pm \frac{\Delta t}{2}\right) \quad (3.17)$$

Vice versa, the particle distribution function is obtained by matrix multiplication of the inverse matrix $E_{ki}^{-1} = w_i E_{ik}$.

$$f_i \left(\vec{x} \pm \frac{\vec{c}_i \Delta t}{2}, t \pm \frac{\Delta t}{2} \right) = \sum_k w_i E_{ik} \alpha_k^\pm(\vec{x}) \quad (3.18)$$

For the D2Q9 velocity set E_{ki} and α_k^\pm are defined as:

$$\alpha_k^\pm(\vec{x}) = \begin{pmatrix} \rho(\vec{x}) \\ \rho(\vec{x}) u_x(\vec{x}) \pm \frac{\Delta t}{2} F_x(\vec{x}) \\ \rho(\vec{x}) u_y(\vec{x}) \pm \frac{\Delta t}{2} F_y(\vec{x}) \\ 3\rho(\vec{x}) u_x(\vec{x}) u_x(\vec{x}) + \rho(\vec{x}) (-6\nu(\vec{x}) \pm \Delta t) \frac{\partial u_x}{\partial x}(\vec{x}) \\ 3\rho(\vec{x}) u_x(\vec{x}) u_y(\vec{x}) + \frac{\rho(\vec{x}) (-6\nu(\vec{x}) \pm \Delta t)}{2} \left(\frac{\partial u_x}{\partial y}(\vec{x}) + \frac{\partial u_y}{\partial x}(\vec{x}) \right) \\ 3\rho(\vec{x}) u_y(\vec{x}) u_y(\vec{x}) + \rho(\vec{x}) (-6\nu(\vec{x}) \pm \Delta t) \frac{\partial u_y}{\partial y}(\vec{x}) \\ 0 \\ 0 \\ 0 \end{pmatrix} \quad E_{ki} = \begin{pmatrix} 1 \\ c_{ix} \\ c_{iy} \\ 3c_{ix}^2 - 1 \\ 3c_{ix}c_{iy} \\ 3c_{iy}^2 - 1 \\ c_{ix}(3c_{iy}^2 - 1) \\ c_{iy}(3c_{ix}^2 - 1) \\ \frac{1}{2}(3c_{ix}^2 - 1)(3c_{iy}^2 - 1) \end{pmatrix} \quad (3.19)$$

The filter matrix is independent of time and position while the solution vector is time and position dependent and changes every time step as a result of changes in density, velocity, viscosity and/or force [39].

The Numerical procedure for the filter matrix lattice Boltzmann method for the D2Q9 velocity set, in absence of external forces is as follows [39]:

1. **Initialization:** $\alpha_k^-(\vec{x})$ is chosen and the initial particle distribution function $f_i \left(\vec{x} - \frac{\vec{c}_i \Delta t}{2}, t - \frac{\Delta t}{2} \right) = f_i^-$ is calculated using equation 3.18. Initial values are chosen for $\rho(\vec{x})$ and $\nu(\vec{x})$.
2. **Pre-collision solution vector** $\alpha_k^-(\vec{x})$ is updated based on f_i^- using equation 3.17.
3. **Collision:** Velocity components $u_x(\vec{x})$ and $u_y(\vec{x})$ and post-collision solution vector $\alpha_k^+(\vec{x})$ are determined from $\alpha_k^-(\vec{x})$.
4. **Update of fluid properties:** Based on post-collision solution vector $\alpha_k^+(\vec{x})$, density $\rho(\vec{x})$ and kinematic viscosity $\nu(\vec{x})$ are updated:
 - The density follows directly from the first component of α_k^+ .
 - The shear rate is computed using the 1st and 4 – 6th components of α_k^+ . If the kinematic viscosity is a function of shear rate it is updated accordingly. E.g. for a power law fluid:

$$\nu(\dot{\gamma}(\vec{x})) = \frac{K}{\rho(\vec{x})} (\dot{\gamma}(\vec{x}))^{n-1} \quad (3.20)$$

For fluids with more complex shear behaviour a curve fit to experimental viscosity vs. shear rate data is used to compute the new viscosity.

5. The **post collision particle distribution function** $f_i \left(\vec{x} + \frac{\vec{c}_i \Delta t}{2}, t + \frac{\Delta t}{2} \right)$ is obtained from the post-collision solution vector $\alpha_k^+(\vec{x})$ via equation 3.18.
6. **Streaming:** All particles with velocity \vec{c}_i move from lattice point \vec{x} to neighbouring lattice point $\vec{x} + \vec{c}_i \Delta t$. Boundary conditions are applied along the edge of the simulation domain. Section 3.4 elaborates on the boundary conditions. The resulting distribution function: $f_i^+ = f_i \left(\vec{x} + \frac{\vec{c}_i \Delta t}{2}, t + \frac{\Delta t}{2} \right) = f_i \left((\vec{x} + \vec{c}_i \Delta t) - \frac{\vec{c}_i \Delta t}{2}, (t + \Delta t) - \frac{\Delta t}{2} \right)$ corresponds to f_i^- for the next time step.
7. Step 2 to 6 are **repeated until convergence**.

3.3. Geometry

The active part of the SSFB consists of two half cells separated by a membrane. In this research the half cells are represented as two separate flow channels with parallel plate geometry. Figure 3.1 shows the computational domain of one half cell.

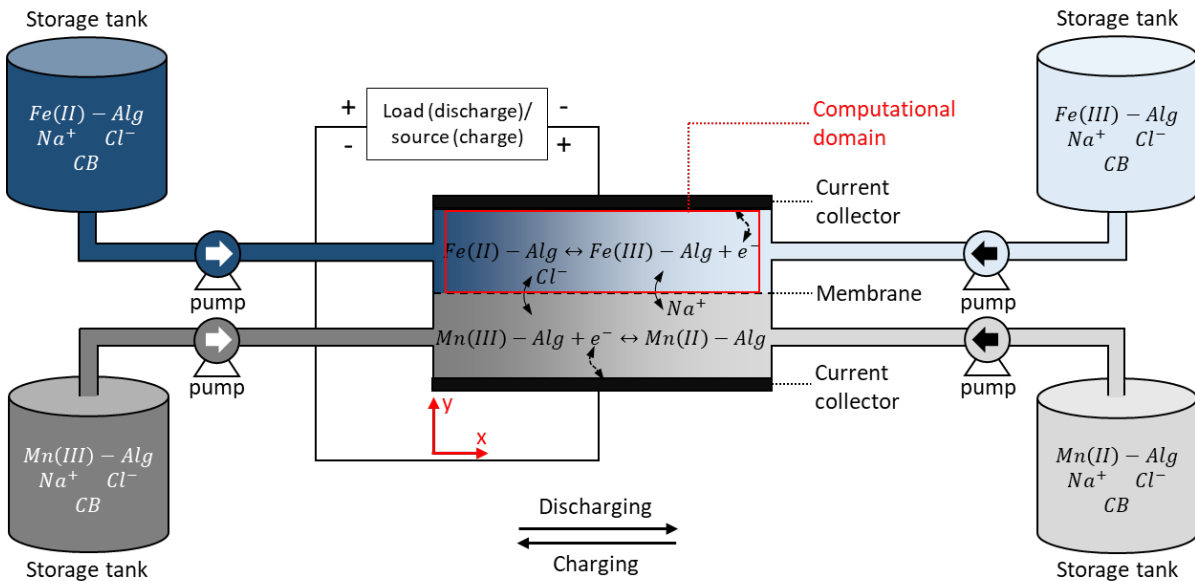


Figure 3.1: Schematic illustration of SSFB with the computational domain marked in red. The computational domain is (in 2D representation) a rectangular part of the half cell which is sandwiched between the membrane and a current collector.

- For simplicity the system is assumed to be 2 dimensional, i.e. the plates are assumed to be infinitely long in z-direction. In this early stage of research, a 2D model suffices to give initial predictions of the flow behaviour and electrical characteristics of alginate electrolytes in an SSFB. Adding a third dimension would increase complexity and computation time, while bringing only a limited added scientific value.
- The in- and outlet of the flow channel are connected to tubes for the in- and outflow of the electrolyte. These tubes have smaller cross sectional areas than the flow channel, resulting in diverging and converging flow at the in- and outlet. These in- and outflow effects are neglected: the y-component of the fluid velocity in- and outlet is assumed to be zero.
- The velocity at the inlet is externally imposed by the pump and taken to be uniform. At the outlet the fluid flows smoothly out of the computational domain (i.e. the outlet boundary does not affect the simulation in the computational domain.)

An example of a spatially discretised lattice for parallel plate geometry is shown in figure 3.2. It is a square lattice with N_x lattice points in the x-direction and N_y lattice points in the y-direction. The velocity is discretised using the D2Q9 velocity set which is described in section 2.2.3. The particle distribution function has 9 components and is defined at each lattice point.

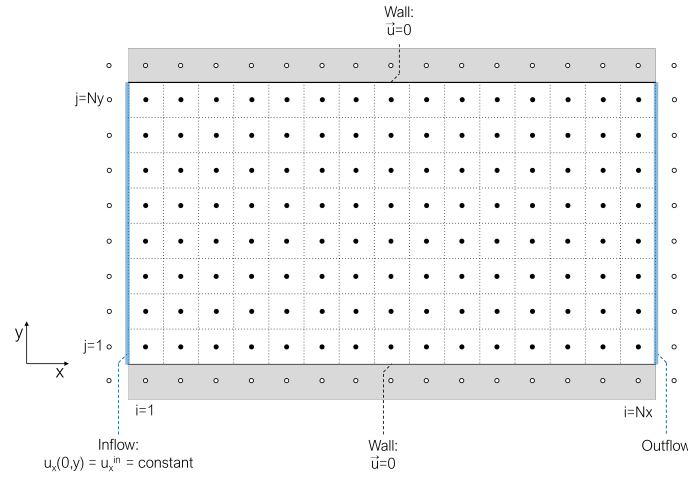


Figure 3.2: Schematic illustration of parallel plate geometry with discrete spatial coordinates. The fluid nodes (black) and the ghost nodes (white) are depicted with their indices i and j . The ghost nodes are necessary for implementing the boundary conditions. The inflow velocity is constant, the velocity at the walls is zero.

3.4. Boundary Conditions

Boundary conditions must be chosen in such way that the simulation correctly represents the physical situation. This section describes the boundary conditions at the walls (3.4.1), inlet (3.4.2) and outlet (3.4.3).

3.4.1. Walls

The fluid velocity is zero at the walls. This is established by implementing a no slip velocity boundary condition. The most common approach in the lattice Boltzmann method for no slip boundary conditions is the bounce back method [38]. The velocities of particles that hit the wall are reversed such that the particles are reflected back to where they came from. In the bounce back method the wall is positioned approximately halfway between two lattice nodes. There are two approaches for the bounce back method:

- In the fullway bounce back method it takes two time steps to reflect populations. The boundary populations that are directed at the wall move to a nodes located inside the wall. In the next collision step their directions are reversed and they stream back into the fluid. This method is first order accurate [38].
- In the halfway bounce back the particles are assumed to hit the wall halfway through the streaming step. Their directions are reversed directly after which the streaming step is completed. This method is second order accurate [38].

Because of its better accuracy the halfway bounce back method was preferred in this research. To implement the halfway bounce back method, an extra set of lattice points is created in the solid: the ghost-nodes. They are located along the solid-fluid boundary, just inside the solid. Prior to the streaming step the particles along the boundary that are directed towards the walls, are copied to the ghost nodes and reversed as shown in figure 3.3. During the streaming step, these particles stream from the ghost nodes into the fluid: This way, the particles coming from the ghost-nodes cancel out the particles coming from the fluid boundary nodes resulting in a net zero velocity at the wall. This process also ensures that particles cannot leave the fluid through the wall.

Figure 3.3 shows the creation of ghost-nodes and populations at the lower wall. The particle distributions at the ghost nodes are obtained from the particle distributions on the fluid boundary-nodes in the following manner:

$$\begin{aligned}
 f_5^*(x-1, y^{ghost}) &= f_7(x, y^{boundary}) \\
 f_2^*(x, y^{ghost}) &= f_4(x, y^{boundary}) \\
 f_6^*(x+1, y^{ghost}) &= f_8(x, y^{boundary})
 \end{aligned} \tag{3.21}$$

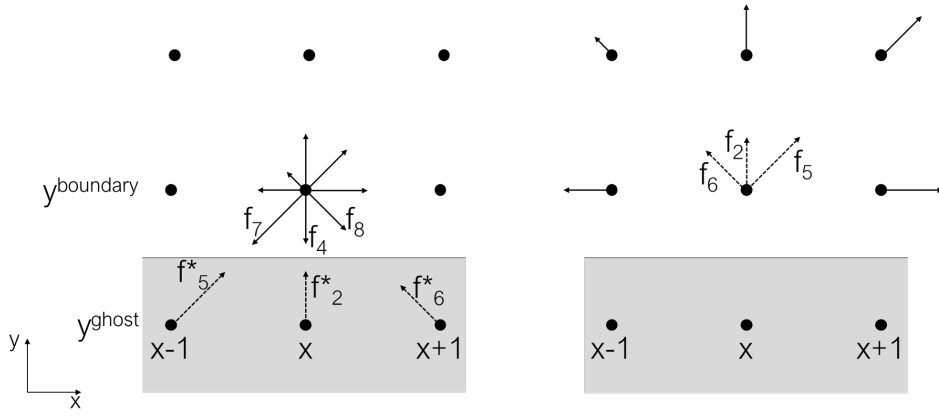


Figure 3.3: Illustration of bounce back boundary condition. The grey region represents the wall and the white region the fluid. The ghost nodes are located inside the walls. Left: Based on the populations of the fluid nodes that are located along the boundary, mirror populations are created at the ghost nodes. Right: Populations in the fluid nodes after streaming.

The post-streaming populations f_i^{new} are computed from the pre-streaming f_i and ghost node populations f_i^* by equations 3.22

$$\begin{aligned}
 f_0^{new}(x, y^{boundary}) &= f_0(x, y^{boundary}) \\
 f_1^{new}(x, y^{boundary}) &= f_1(x-1, y^{boundary}) \\
 f_2^{new}(x, y^{boundary}) &= f_2^*(x, y^{ghost}) \\
 f_3^{new}(x, y^{boundary}) &= f_3(x+1, y^{boundary}) \\
 f_4^{new}(x, y^{boundary}) &= f_4(x, y^{boundary} + 1) \\
 f_5^{new}(x, y^{boundary}) &= f_5^*(x-1, y^{ghost}) \\
 f_6^{new}(x, y^{boundary}) &= f_6^*(x+1, y^{ghost}) \\
 f_7^{new}(x, y^{boundary}) &= f_7(x+1, y^{boundary} + 1) \\
 f_8^{new}(x, y^{boundary}) &= f_8(x-1, y^{boundary} + 1)
 \end{aligned} \tag{3.22}$$

3.4.2. Inlet

The inlet and outlet are open boundaries where the flow respectively enters and leaves the computational domain. As the exact physical behaviour outside the boundaries generally is unknown, a physical approximation has to be made at open boundaries to couple the simulation to the physical problem.

The inlet boundary condition must impose a uniform inflow velocity. There are multiple inlet boundary techniques that can achieve this. In link-wise methods the boundary is located approximately halfway between the lattice nodes whereas in wet-node approaches the lattice nodes are located on the boundary. In this research two widely used velocity boundary techniques, one link-wise and the other one wet-node, are implemented and compared. The bounce back (BB) method (link-wise) and the non-equilibrium bounce back boundary (NEBB) method. The inlet boundary condition is applied after the streaming step and calculates the unknown populations located along the inlet boundary. After streaming, populations f_1 , f_5 and f_8 are unknown. The other populations are known. The two inlet boundary methods are explained below:

- The **bounce back boundary method** is a link-wise approach. It looks like the wall bounce back method with an additional term. This extra term imposes a change in momentum such that the fluid velocity at the inlet is the prescribed inlet velocity. The populations at the ghost nodes are

computed according to equation 3.23 [38].

$$\begin{aligned} f_5(0, y) &= f_7^{old}(0, y) - 2w_7\rho(0, y) \frac{\vec{c}_7 \cdot \vec{u}_{inlet}}{c_s^2} \\ f_1(0, y) &= f_3^{old}(0, y) - 2w_3\rho(0, y) \frac{\vec{c}_3 \cdot \vec{u}_{inlet}}{c_s^2} \\ f_8(0, y) &= f_6^{old}(0, y) - 2w_6\rho(0, y) \frac{\vec{c}_6 \cdot \vec{u}_{inlet}}{c_s^2} \end{aligned} \quad (3.23)$$

- Alternatively, a uniform inlet velocity can be implemented via the **non-equilibrium bounce back method**. This is a wet-node method. After streaming, the distribution function is extrapolated to find the unknown populations (f_1, f_5, f_8) based on the known populations (equation 3.24) [46].

$$\begin{aligned} f_1(0, y) &= f_3(0, y) + \frac{2}{3}u_x^{in}\rho^{in} \\ f_5(0, y) &= f_7(0, y) + \frac{1}{2}(f_4 - f_2) + \frac{1}{6}\rho^{in}u_x^{in} \\ f_8(0, y) &= f_6(0, y) + \frac{1}{2}(f_2 - f_4) + \frac{1}{6}\rho^{in}u_x^{in} \end{aligned} \quad (3.24)$$

3.4.3. Outlet

The outlet boundary condition should realize a smooth, continuous flow through the boundary. There are many ways to establish this. Analogously to the inlet boundary, the anti bounce back (link-wise) or non-equilibrium bounce back (wet-node) method can be applied with a fixed pressure instead of a fixed velocity [38]. However, when applying these two methods and comparing the results it was observed that the choice of outflow boundary technique in some cases influences the accuracy and stability of the simulation output. This is undesirable since the two methods represent the same physical situation. Neither of these two boundary techniques gave satisfactory results in all simulations. Therefore three other widely used outflow boundary techniques were implemented and evaluated too: the convective (CV) method, the Neumann method and the extrapolation (EP) method [47]. Section 6.1.2 and appendix A elaborate on the comparison of the boundary techniques.

The outflow boundary condition is applied after the streaming step. The unknown post-streaming populations at the outlet are (f_3, f_6 and f_7). The convective method, the non-equilibrium bounce back method and the anti bounce back pressure (ABB) method only calculate the unknown populations at the outflow boundary. The Neumann method and the extrapolation method calculate all populations at the outflow boundary, based on neighbouring post streaming populations. The outlet boundary techniques are listed below:

- **Convective method:** The unknown populations at the outflow boundary ($x = N_x - 1$) are calculated based on their previous values and on the velocity at the neighbouring ($x = N_x - 2$) lattice point.

$$\begin{aligned} f_i(N_x - 1, y) &= \frac{f_i^{old}(N_x - 1, y, t) + \lambda(y) f_i(N_x - 2, y)}{1 + \lambda(y)} \\ \lambda(y) &= u_x(N_x - 2, y) \frac{\Delta t}{\Delta x} \end{aligned} \quad (3.25)$$

for $i \in [3, 6, 7]$ [47].

- **Non-equilibrium bounce back method for pressure:** The unknown populations (f_3, f_6 and f_7) are calculated based on a post-streaming extrapolation of the known populations [46].

$$\begin{aligned} f_3(N_x - 1, y) &= f_1(N_x - 1, y) - \frac{2}{3}u_x^{out}(y)\rho_0 \\ f_6(N_x - 1, y) &= f_8(N_x - 1, y) + \frac{f_4(N_x - 1, y) - f_2(N_x - 1, y)}{2} - \frac{1}{6}\rho_0 u_x^{out}(y) \\ f_7(N_x - 1, y) &= f_5(N_x - 1, y) + \frac{f_2(N_x - 1, y) - f_4(N_x - 1, y)}{2} - \frac{1}{6}\rho_0 u_x^{out}(y) \end{aligned} \quad (3.26)$$

The outlet velocity is defined as:

$$u_x^{out}(y) = -1 + \frac{f_0(N_x - 1, y) + f_2(N_x - 1, y) + f_4(N_x - 1, y)}{\rho_0} + \frac{2(f_1(N_x - 1, y) + f_5(N_x - 1, y) + f_8(N_x - 1, y))}{\rho_0} \quad (3.27)$$

- **Anti bounce back method for pressure:** This approach imposes a pressure at the outflow boundary. It is similar to the regular bounce back approach that was applied to the walls. The difference with the regular bounce back approach is that the populations at the ghost nodes are negative instead of positive. An extra term is added to the equation to take care of the prescribed pressure profile. To model a continuous, smooth outflow, the outflow pressure is set at its initial value everywhere ($\rho(x^{boundary}, y) = \rho_0$). This leads to the following equations for populations at the ghost nodes that are located to the right of the computational domain [38]:

$$\begin{aligned} f_6(N_x - 1, y) &= -f_8^{old}(N_x - 1, y) + 2w_8\rho_0 \left(1 + \frac{(\vec{c}_8 \cdot \vec{u}^{out})^2}{2c_s^4} - \frac{\vec{u}^{out2}}{2c_s^2} \right) \\ f_3(N_x - 1, y) &= -f_1^{old}(N_x - 1, y) + 2w_1\rho_0 \left(1 + \frac{(\vec{c}_1 \cdot \vec{u}^{out})^2}{2c_s^4} - \frac{\vec{u}^{out2}}{2c_s^2} \right) \\ f_7(N_x - 1, y) &= -f_5^{old}(N_x - 1, y) + 2w_5\rho_0 \left(1 + \frac{(\vec{c}_5 \cdot \vec{u}^{out})^2}{2c_s^4} - \frac{\vec{u}^{out2}}{2c_s^2} \right) \end{aligned} \quad (3.28)$$

The outlet velocity \vec{u}^{out} is unknown and is estimated by extrapolation of the velocity at the boundary node and the velocity at its left neighbour [48]:

$$\vec{u}^{out}(y) = \frac{3}{2}\vec{u}^{old}(N_x - 1, y) - \frac{1}{2}\vec{u}^{old}(N_x - 2, y) \quad (3.29)$$

- **Neumann method with zero x-derivative:** This method sets the x-derivatives of the populations to zero. The populations at outflow nodes ($x = N_x - 1$) are calculated from the neighbouring populations at $x = N_x - 2$ [47].

$$f_i(N_x - 1, y) = f_i(N_x - 2, y) \quad (3.30)$$

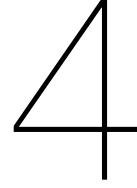
for $i \in [0, 1, 2, 3, 4, 5, 6, 7, 8]$

- **Extrapolation method:** This boundary technique calculates the populations at the outlet based on the populations of the previous two nodes in the x-direction [47].

$$f_i(N_x - 1, y) = 2f_i(N_x - 2, y) - f_i(N_x - 3, y) \quad (3.31)$$

for $i \in [0, 1, 2, 3, 4, 5, 6, 7, 8]$

The nodes in the corners of the computational domain border both on the wall and on the in-/outlet. In these nodes the in-/outlet boundary condition overrules the wall boundary condition [38].



Description of Electric Field Model

As derived in section 2.3 the electric potential in the flow channel of an SSFB is described by an equation that has the form of a conservation law (equation 2.25). The finite volume method (FVM) is a popular technique for discretisation of differential equations that describe conservation laws. It has applications in various fields including fluid dynamics, heat transfer and electromagnetics. In finite volume models, the computational domain is divided in contiguous, non-overlapping volume elements. The governing differential equation(s) is (are) integrated over each control volume. This volume integral is then converted into a surface integral by the divergence theorem. The surface integral represents the flux of the integrand through the surface of the control volume. Since the control volumes are contiguous, the flux out of a control volume equals the flux into its neighbouring control volumes. This results in a coupled system of equations [49].

This chapter explains how the finite volume method is implemented to solve the differential equation for the electric potential and to compute the internal resistance. Section 4.1 describes the geometry and governing differential equation. In section 4.2 the differential equation is discretised, resulting in a coupled, linear system of equations. Then, in section 4.3 the system of equations is rewritten as a matrix equation and solved for the electric potential. Finally, section 4.4 explains the derivation of the internal resistance from the electric potential.

4.1. Geometry

In this study, the flow channel is represented as a cuboidal resistance that has an inhomogeneous conductivity. The resistance is sandwiched between two parallel, conducting plates over which a voltage is applied. As derived in section 2.3, the electric potential in a conductor is described by equation 2.25. Integrating this expression over a control volume Ω and applying the divergence theorem results in the following equation for the electric potential:

$$0 = \iiint_{\Omega} \vec{\nabla} \cdot \sigma \vec{\nabla} V \, d^3\vec{r} = \iint_{\partial\Omega} \sigma \vec{\nabla} V \cdot \hat{n} \, dA = \iint_{\partial\Omega} \vec{j} \cdot \hat{n} \, dA \quad (4.1)$$

The physical meaning of this equation is that the net current through any closed surface that does not enclose a current source, is zero [40].

The computational domain consists of the flow channel, two parallel conducting plates located at the top and bottom of the channel, and a surrounding medium. Dirichlet boundary conditions are applied at the surface of the parallel plates and at the edge of the computational domain. As discussed in section 3.3 the width W of the flow channel in the z-direction is sufficiently large to neglect edge effects in the z-direction (i.e. the system is independent of z-coordinate). The flow channel can therefore be divided into volume elements that cover the entire width of the channel, essentially making the problem 2 dimensional.

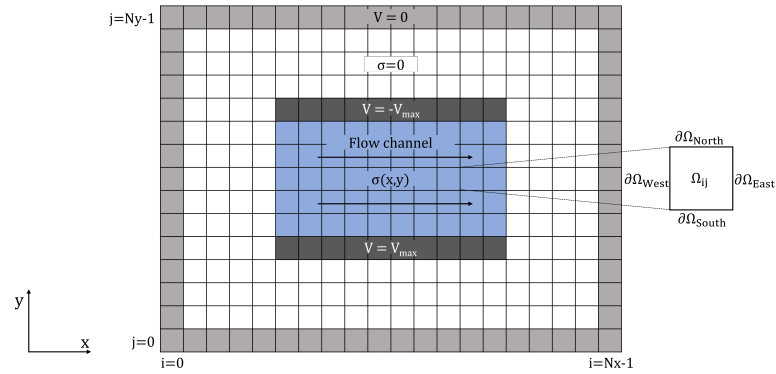


Figure 4.1: Flow channel and surrounding domain represented on regular quadrilateral grid. Blue region: Flow channel with inhomogeneous conductivity. Dark grey regions: Parallel conducting plates over which a voltage is applied. White region: Surrounding medium with low conductivity. Light grey region: Edge of computational domain with electric potential of 0 V. The square on the right-hand side of the image is the magnification of one lattice site.

4.2. Discretisation

To discretise the problem, the computational domain is divided into cuboidal volume elements with $\Delta y = \Delta x$ and $\Delta z = W$. This results in a quadrilateral grid in the x, y -plane. A schematic illustration of the computational domain is shown in figure 4.1. Indices i and j represent respectively the x and y -coordinates of the elements. In the figure four regions are distinguished:

- **Flow channel (blue):** The flow channel consists of many volume elements, each with their own conductivity $\sigma(i, j)$.
- **Parallel plates (dark grey):** A voltage is applied over the flow channel by setting the electric potential in the upper plate at $V = -V_{max}$ and in the bottom plate at $V = V_{max}$.
- **Surrounding medium (white):** The conductivity of the surrounding medium is set to 0 to ensure that all current flows through the flow channel.
- **Edge of computational domain (light grey):** To close the system of equations, the electric potential at the edge of the computational domain is set to zero. In reality the electric potential approaches zero infinitely far away from the plates. Therefore, this assumption is more accurate if the edge is further away from the computational domain. This is at the cost of computational time. Hence, a trade-off must be made between accuracy and computational efficiency.

For cuboidal volume elements equation 4.1 is rewritten as:

$$0 = \int_{\partial\Omega_{East}} \sigma \vec{\nabla} V \cdot \hat{x} dy W + \int_{\partial\Omega_{West}} \sigma \vec{\nabla} V \cdot -\hat{x} dy W + \int_{\partial\Omega_{North}} \sigma \vec{\nabla} V \cdot \hat{y} dx W + \int_{\partial\Omega_{South}} \sigma \vec{\nabla} V \cdot -\hat{y} dx W \quad (4.2)$$

The four components respectively represent the electric current flowing out of the control volume through its eastern, western, northern and southern boundary. Following the discretisation, the fluxes at the element interfaces are approximated using a central difference approximation for the partial derivatives of V . Interior volume elements are treated slightly differently than volume elements that border the parallel plate or are located at the edge of the domain [49]:

- As an example, the current flowing through the eastern boundary of an interior volume element is given by equation 4.3.

$$I_x \left(i + \frac{1}{2}, j \right) = \iint_{\partial\Omega_{East}} \sigma \vec{\nabla} V \cdot \hat{x} dy dz \approx \sigma \left(i + \frac{1}{2}, j \right) \frac{V(i+1, j) - V(i, j)}{\Delta x} \Delta y \Delta z \quad (4.3)$$

In this equation, the conductivity at the interface is approximated using linear interpolation:

$$\sigma\left(i + \frac{1}{2}, j\right) = \frac{\sigma(i + 1, j) + \sigma(i, j)}{2} \quad (4.4)$$

The current through the northern, southern and western boundaries are described with similar equations. Combining this with equation 4.1 yields the following equation for the flux out of an interior volume element:

$$\begin{aligned} 0 = & \sigma\left(i + \frac{1}{2}, j\right) \frac{V(i + 1, j) - V(i, j)}{\Delta x} \Delta y \Delta z + \sigma\left(i - \frac{1}{2}, j\right) \frac{V(i - 1, j) - V(i, j)}{\Delta x} \Delta y \Delta z \\ & + \sigma\left(i, j + \frac{1}{2}\right) \frac{V(i, j + 1) - V(i, j)}{\Delta y} \Delta x \Delta z + \sigma\left(i, j - \frac{1}{2}\right) \frac{V(i, j - 1) - V(i, j)}{\Delta y} \Delta x \Delta z \end{aligned} \quad (4.5)$$

- If however, the element boundary is located at the edge of the computational domain or if it borders one of the parallel plates, a Dirichlet boundary condition is applied. The partial derivatives of the electric potential are then approximated by either the forward or by the backward difference method. Furthermore, the conductivity at the boundary is assumed to be equal to the conductivity at the cell center. As an example, the current through an eastern boundary with a Dirichlet boundary condition is given by equation 4.6.

$$I_x\left(i + \frac{1}{2}, j\right) = \iint_{\partial\Omega_{East}} \sigma \vec{\nabla} V \cdot \hat{x} \, dy dz \approx \sigma(i, j) \frac{V^{boundary} - V(i, j)}{\Delta x/2} \Delta y \Delta z \quad (4.6)$$

Combining this with equation 4.1 yields the following equation for the flux out of an element with one Dirichlet boundary condition at its eastern boundary:

$$\begin{aligned} 0 = & \sigma(i, j) \frac{V^{boundary} - V(i, j)}{\Delta x/2} \Delta y \Delta z + \sigma\left(i - \frac{1}{2}, j\right) \frac{V(i - 1, j) - V(i, j)}{\Delta x} \Delta y \Delta z \\ & + \sigma\left(i, j + \frac{1}{2}\right) \frac{V(i, j + 1) - V(i, j)}{\Delta y} \Delta x \Delta z + \sigma\left(i, j - \frac{1}{2}\right) \frac{V(i, j - 1) - V(i, j)}{\Delta y} \Delta x \Delta z \end{aligned} \quad (4.7)$$

4.3. Solution Method

For each volume element an equation that describes the electric potential is set up, analogously to equations 4.5 and 4.7. Each equation is linked to the equation of its four neighbouring elements because of the shared boundary surface. (E.g. The flux out of the eastern boundary of control volume is the same as the flux into the western boundary of its left neighbour.) The equations therefore form a linear system of equations. This system is rewritten in the form of a linear matrix equation.

$$\mathbf{M}\vec{U} = \vec{b} \quad (4.8)$$

\mathbf{M} is a square matrix with dimensions $(N_x N_y) \times (N_x N_y)$ and vectors \vec{U} and \vec{b} have length $(N_x N_y)$. In this equation $\vec{U}(i \times N_y + j)$ represents $V(i, j)$. All equations are translated into components of \mathbf{M} , and \vec{b} . As an example, equation 4.7 is split up into four components of \mathbf{M} and one component of \vec{b} [49]:

$$\begin{aligned} M(i \times N_y + j, i \times N_y + j) = & -\left(\sigma(i, j) \frac{\Delta y \Delta z}{\Delta x/2} + \frac{\sigma(i - 1, j) + \sigma(i, j)}{2} \frac{\Delta y \Delta z}{\Delta x} \right. \\ & \left. + \frac{\sigma(i, j + 1) + \sigma(i, j)}{2} \frac{\Delta x \Delta z}{\Delta y} + \frac{\sigma(i, j - 1) + \sigma(i, j)}{2} \frac{\Delta x \Delta z}{\Delta y} \right) \end{aligned} \quad (4.9)$$

$$M(i \times N_y + j, (i - 1) \times N_y + j) = \frac{\sigma(i - 1, j) + \sigma(i, j)}{2} \frac{\Delta y \Delta z}{\Delta x} \quad (4.10)$$

$$M(i \times N_y + j, i \times N_y + (j - 1)) = \frac{\sigma(i, j - 1) + \sigma(i, j)}{2} \frac{\Delta x \Delta z}{\Delta y} \quad (4.11)$$

$$M(i \times Ny + j, i \times Ny + (j + 1)) = \frac{\sigma(i, j + 1) + \sigma(i, j)}{2} \frac{\Delta x \Delta z}{\Delta y} \quad (4.12)$$

$$b(i \times Ny + j) = -V^{boundary} \sigma(i, j) \frac{\Delta y \Delta z}{\Delta x / 2} \quad (4.13)$$

The resulting matrix \mathbf{M} is a banded matrix. A dedicated Python function (`scipy.linalg.solve_banded`) solves the matrix equation exactly, giving the solution for \vec{U} . $V(i, j)$ is then obtained by reshaping \vec{U} .

4.4. Electric Current and Resistance

As previously mentioned, the $\sigma \vec{\nabla} V$ -flux between two volume elements represents the electric current flowing between them (see equation 4.3). The current can therefore be computed from the electric potential as described in equation 4.14.

$$I_x(i, j) = - \left(\frac{\sigma(i-1, j) + \sigma(i, j)}{2} \right) \left(\frac{V(i, j) - V(i-1, j)}{\Delta x} \right) \Delta y \Delta z \quad (4.14)$$

$$I_y(i, j) = - \left(\frac{\sigma(i, j-1) + \sigma(i, j)}{2} \right) \left(\frac{V(i, j) - V(i, j-1)}{\Delta y} \right) \Delta x \Delta z$$

The fluxes are defined at the interfaces between elements rather than at the centers. Therefore, the grid of the current in x-direction I_x is translated $-\Delta x/2$ in x-direction with respect to the electric potential grid, and the grid of the current in y-direction is translated $-\Delta y/2$ in y-direction [49]. The three grids are schematically depicted in figure 4.2.

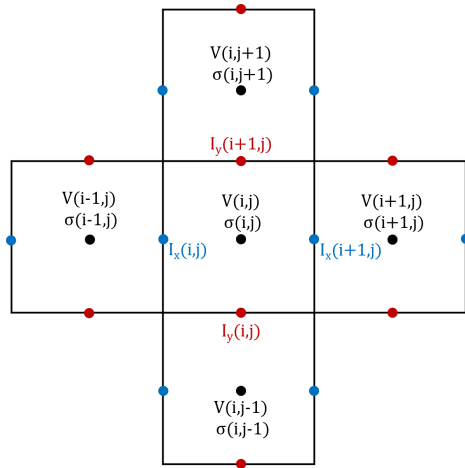


Figure 4.2: Schematic illustration of the different grids for electric potential V (black), current in x-direction I_x (blue) and current in y-direction I_y (red). The potential is defined at the centers of lattice sites while the currents are defined at the interfaces between lattice sites.

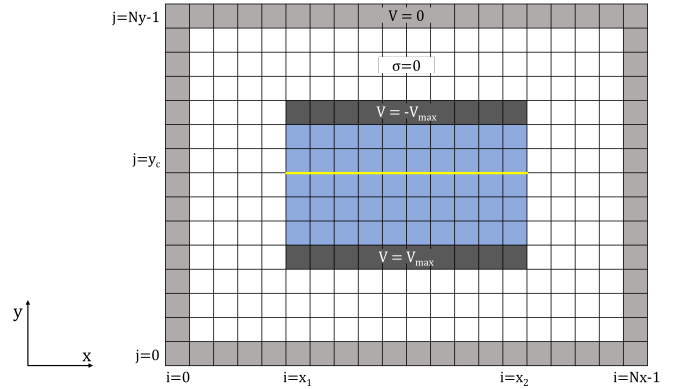


Figure 4.3: Schematic illustration of flow channel and surrounding medium on a regular quadrilateral grid with a simple contour (yellow line) that is used to evaluate the total current through the flow channel. The surrounding medium is an isolator. All current between the two plates therefore passes through this yellow contour.

The resistance is computed by dividing the voltage applied over the flow channel by the current flowing through it, as described by equation 2.20. As the flow channel has no sinks or sources, the current is computed by summing over the current through any contour that is located in between the parallel plates and spans the entire length of the flow channel. As an example, the simplest contour is a straight line as shown in yellow in figure 4.3. For this straight contour only y-components of the current are relevant such that the total current is given by equation 4.15.

$$\sum_{i=x_1}^{x_2} I_y(j = y_c, i) \quad (4.15)$$

5

Description of Experimental Method for Rheo-impedance Measurements

This thesis analyses the effect of flow behaviour on internal electrical resistance in SSFBs. Two fluid characteristics, viscosity and conductivity, play a decisive role in the internal resistance. Both are functions of shear rate. The viscosity and conductivity of the aqueous alginate suspension with carbon black particles have not yet been determined. Therefore the data of a comparable fluid, a non-aqueous carbon black suspension (see section 2.5), is used in this research. Presumably, the viscosity and conductivity, which are both functions of shear rate, of the alginate slurry differ from those of the non-aqueous carbon black suspension due to their different compositions. It is therefore crucial to characterise the viscosity and conductivity of the alginate electrolyte in order to get a reliable prediction of the internal resistance and pumping power. Furthermore, viscosity and conductivity experiments can be used to study the influence of factors such as temperature, pH and carbon black volume fraction on the electrical and rheological properties. This would allow to optimise the electrolyte suspension for low internal resistance and low pumping losses.

This chapter presents the experimental design for simultaneous viscosity and conductivity measurements over a range of shear rates. Section 5.1 introduces the experimental setup. Subsequently, section 5.2 discusses the torque measurements and the post-processing of the results into a viscosity-shear rate relation. Finally, section 5.3 explains the impedance measurements in more detail and proposes a post-processing algorithm to convert the measured impedance data into a conductivity-shear rate relation.

5.1. Experimental Setup

The experimental setup needed for simultaneous viscosity and conductivity measurements consists of 2 main components:

- **Rheometer:** This device consists of two circular coaxial parallel plates (with radius R and gap H) between which the fluid is sandwiched. The upper plate rotates at angular frequency ω while the lower plate is kept stationary. The rheometer measures the torque that is applied to compensate the friction of the fluid and maintain the angular frequency. This is done for a range of angular frequencies, resulting in torque as a function of angular frequency $T(\omega)$.
- **Dielectro rheological device (DRD):** This device performs electrical impedance spectroscopy. The parallel plates play the role of electrodes. The DRD applies an alternating voltage over the plates and measures the response in terms of electrical current flowing through the sample. The real and imaginary part of the impedance ($Z = V/I$) are plotted for a range of frequencies resulting in a Nyquist diagram. Based on the Nyquist diagram, and using an equivalent circuit (i.e. an electrical circuit that represents the fluid as a network of resistances, capacitances and inductances), the software of the DRD derives the values of all electrical components in the equivalent circuit. In this manner the ionic and electronic resistance of the electrolyte are derived. This is done

for a range of angular frequencies resulting in the resistance as a function of angular frequency ($R_{electronic}(\omega)$, $R_{ionic}(\omega)$) [12].

A schematic image of the rheometer is shown in figure 5.1.

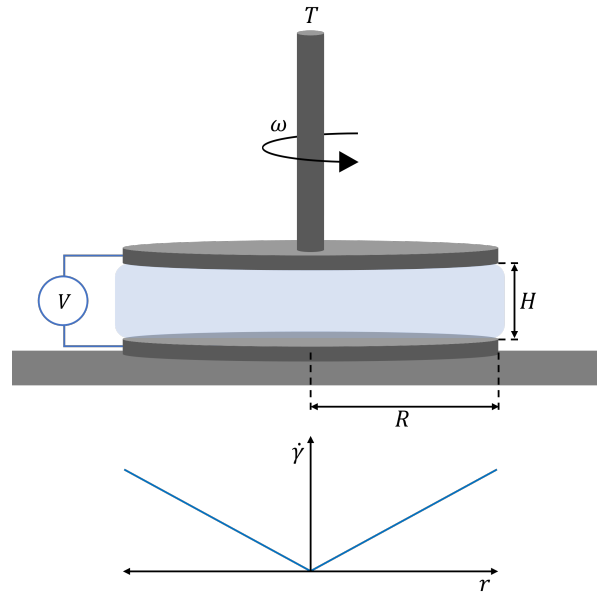


Figure 5.1: Schematic illustration of parallel plate rheometer. The fluid (light blue) is sandwiched between two disks over which a voltage is applied. The lower disk is stationary and the upper disk rotates at angular frequency ω . The rheometer measures the torque T that is needed to maintain the angular frequency. The graph below the rheometer gives the shear rate $\dot{\gamma}$ as a function of radial distance r .

5.2. Viscosity Measurements

A rheometer measures the total torque needed to maintain a certain angular frequency. Hence, the raw measurement output of the rheometer is torque as a function of angular frequency $T(\omega)$. This data must be converted into dynamic viscosity as a function of shear rate $\eta(\dot{\gamma})$. Dynamic viscosity and torque (which is the product of force and lever arm) are related via equations 5.1 and 5.2.

$$T(\omega) = \int_0^R r \tau(\dot{\gamma}(\omega, r)) 2\pi r dr \quad (5.1)$$

$$\tau(\dot{\gamma}) = \eta(\dot{\gamma}) \dot{\gamma} \quad (5.2)$$

In these equations R is the disk radius and r the radial distance (see figure 5.1). The shear stress τ is a function of shear rate ($\dot{\gamma}$), which, in turn, is related to radial distance r (equation 5.5).

- In a cylindrical coordinate system the coordinates represent radial distance r , angular position θ in tangential direction and height z . In a parallel plate rheometer the fluid only has a tangential velocity component u_θ .
- The shear rate is given by:

$$\dot{\gamma}(\omega, r) = \frac{\partial u_\theta}{\partial z} \quad (5.3)$$

- The only forces acting on the fluid in the flow direction are the friction forces at the upper and lower plate. When the upper plate rotates at a constant angular frequency these two friction forces cancel each other out. The net force acting on a ring ($r \rightarrow r + \delta r, z \rightarrow z + \delta z$), with δr and δz infinitesimally, is zero. This means that the shear stress at the top surface of the ring $\tau(z + \delta z)$ equals the shear stress at the bottom surface of the ring $\tau(z)$. Hence, shear stress is not a function of z .

- This also means that viscosity and shear rate $\dot{\gamma}(\omega, r) = \frac{\partial u_\theta}{\partial z}$ do not have a z -dependence. The tangential velocity thus increases linearly with height from 0 to $r\omega$:

$$u_\theta = \frac{\omega r z}{H} \quad (5.4)$$

The shear rate is proportional to radial distance r :

$$\dot{\gamma}(\omega, r) = \frac{\partial u_\theta}{\partial z} = \frac{\omega r}{H} \quad (5.5)$$

As the dynamic viscosity is unknown and depends on shear rate, the integral in equation 5.1 cannot be rewritten as direct relation between shear stress and torque.

5.2.1. Viscosity Conversion Method

Cross and Kaye [50][51] have developed an approximation method to derive the dynamic viscosity from the torque in a simple way. It is based on a formula that relates shear stress at the rim of a parallel plate rheometer to applied torque in the following way.

$$T + \frac{\omega}{3} \frac{dT}{d\omega} = \frac{2\pi R^3}{3} \tau \quad (5.6)$$

In this equation, shear stress is a function of shear rate $\tau = \tau\left(\dot{\gamma} = \frac{\omega R}{H}\right)$ and hence of angular frequency. For a Newtonian fluid the torque is proportional to the shear stress at the rim:

$$\begin{aligned} T &= \int_0^R \tau(\dot{\gamma}(\omega, r)) 2\pi r^2 dr = \int_0^R \eta \dot{\gamma}(\omega, r) 2\pi r^2 dr = \int_0^R \eta \frac{\omega r}{H} 2\pi r^2 dr \\ &= 2\pi \eta \frac{\omega}{H} \int_0^R r^3 dr = 2\pi \eta \frac{\omega}{H} \frac{R^4}{4} = \frac{\eta \omega R \pi R^3}{H} \frac{1}{2} = \frac{\pi R^3}{2} \tau(\omega, R) \end{aligned} \quad (5.7)$$

While this relation does not hold for non-Newtonian fluids, Cross and Kaye assume the torque to be piecewise linear in intervals $[\omega_i, \frac{4}{3}\omega_i]$, where i is the index of the interval. This means that the torque in interval i is written as:

$$T(\omega) = T_i + A_i \omega \quad \text{for} \quad \omega_i \leq \omega \leq \frac{4}{3}\omega_i \quad (5.8)$$

In this equation A_i is a constant describing the slope of the function at angular frequency ω_i . Combining this with equation 5.6 leads to:

$$\frac{2\pi R^3}{3} \tau\left(\dot{\gamma} = \frac{\omega_i R}{H}\right) = T(\omega_i) + \frac{\omega_i}{3} \left(\frac{dT}{d\omega}\right)_{\omega=\omega_i} = T(\omega_i) + \frac{\omega_i}{3} A_i = T_i + \frac{4\omega_i}{3} A_i = T\left(\frac{4}{3}\omega_i\right) \quad (5.9)$$

This equation relates the torque at angular frequency $\omega = \frac{4}{3}\omega_i$ directly to the shear stress at $\dot{\gamma} = \frac{\omega_i R}{H} = \frac{3}{4} \frac{\omega R}{H}$. The torque-angular frequency curve can therefore be converted into a shear stress-shear rate curve by multiplying the measured torque values by $\frac{3}{2\pi R^3}$, and the corresponding angular frequencies by $\frac{3R}{4H}$ as summarized in equation 5.10.

$$\begin{aligned} \tau &= \frac{3T}{2\pi R^3} \\ \dot{\gamma} &= \frac{3R\omega}{4H} \end{aligned} \quad (5.10)$$

Finally, dividing the shear stress by shear rate yields the dynamic viscosity. Even though this method grossly simplifies the situation, Cross and Kaye have found that the error is less than 1% [51].

5.3. Conductivity Measurements

This section zooms in on the conversion of resistance as a function of angular frequency into conductivity as a function of shear rate. As mentioned in section 5.1 the DRD measures the resistance over a range of angular frequencies of the rheometer. As the outer part of the plate moves with a larger velocity than the parts of the plate located close to the rotation axis ($u^{upper\ plate} = \omega r$), the shear rate varies throughout the sample. It is therefore not straightforward to convert conductance as a function of angular frequency ($\Sigma(\omega) = 1/R(\omega)$) into conductivity as a function of shear rate ($\sigma(\dot{\gamma})$). While there are several methods for the conversion of torque into viscosity in literature (such as the method of Cross and Kaye that was presented in section 5.2.1), no existing method for the conversion of conductance into conductivity was found. Therefore, a dedicated algorithm for the conversion of conductance into conductivity was developed as part of this thesis. The algorithm is based on the same principle as was used by Zubieta *et al.* [52] to determine viscosity from torque measurements in rheometers, but has significant differences. Section 5.3.1 explains the algorithm in detail.

5.3.1. Conductivity Conversion Method

This fluid's rotational velocity u_θ and shear rate as a function of height h and radial distance r are given by equations 5.11 and 5.12.

$$u_\theta(z, r) = \frac{z}{H} \omega r \quad (5.11)$$

$$\dot{\gamma}(r) = \frac{du_\theta}{dz} = \frac{\omega}{H} r \quad (5.12)$$

The measured conductance is the total conductance between the plate and is rewritten as an integral of the conductivity over r .

$$\Sigma(\omega) = \int_0^R \sigma(r, \omega) 2\pi r dr \quad (5.13)$$

As shear rate is proportional to r (equation 5.12), this integral is converted into an integral over shear rate using $\dot{\gamma} = \frac{\omega r}{H}$ and $\dot{\gamma}(R) = \frac{\omega R}{H}$.

$$\Sigma(\omega) = \int_0^R \sigma(r, \omega) 2\pi r dr = 2\pi \left(\frac{H}{\omega}\right)^2 \int_0^{\dot{\gamma}(R)} \sigma(\dot{\gamma}) \dot{\gamma} d\dot{\gamma} \quad (5.14)$$

The maximum shear rate reached in the experiment is $\dot{\gamma}_{max} = \frac{\omega^{max} R}{H}$. To derive the conductivity-shear rate curve from the experimental conductance-angular frequency curve, the shear rate domain is split up into N evenly spaced regions of size $\Delta\dot{\gamma} = \frac{\dot{\gamma}_{max}}{N}$ and with index $i \in [0, N - 1]$.

The algorithm builds the conductivity-shear rate curve recursively, starting at a shear rate of 0 s^{-1} . Every iteration step, it moves to the next shear rate ($+\Delta\dot{\gamma}$) and determines the conductivity from its previous value and the slope of the conductivity:

1. Start at $\dot{\gamma}_i = \dot{\gamma}_0 = 0$, measure $\Sigma(\omega_0 = 0)$ and derive the conductivity at zero shear rate in the following way:

$$\Sigma(\omega_j = 0) = \int_0^R \sigma(\omega_j = 0) 2\pi r dr = \pi R^2 \sigma(\omega_j = 0) \quad (5.15)$$

$$\sigma(\dot{\gamma}_j = 0) = \sigma(\omega_j = 0) = \frac{\Sigma(\omega_j = 0)}{\pi R^2} \quad (5.16)$$

2. Move to the next shear rate $\dot{\gamma}_j = \dot{\gamma}_i + \Delta\dot{\gamma} = \frac{\omega_j R}{H}$, measure $\Sigma(\omega_j)$ and assume linear behaviour of σ between between $\dot{\gamma}_i$ and $\dot{\gamma}_j$.
3. Use $\Sigma(\omega_j)$ and $\Sigma(\omega_i)$ to obtain an expression for the derivative of conductivity at $\dot{\gamma}_i$:

- Start with equation 5.14:

$$\Sigma(\omega_j) = C_j \int_0^{\dot{\gamma}_j} \sigma(\dot{\gamma}) \dot{\gamma} d\dot{\gamma} \quad (5.17)$$

In this equation $C_j = 2\pi(H/\omega_j)^2$.

- Split this equation up in two parts: one that integrates from 0 to $\dot{\gamma}_i$ and one that integrates from $\dot{\gamma}_i$ to $\dot{\gamma}_j$:

$$\frac{\Sigma(\omega_j)}{C_j} = \int_0^{\dot{\gamma}_i} \sigma(\dot{\gamma}) \dot{\gamma} d\dot{\gamma} + \int_{\dot{\gamma}_i}^{\dot{\gamma}_j} \sigma(\dot{\gamma}) \dot{\gamma} d\dot{\gamma} = \frac{\Sigma(\omega_i)}{C_i} + \int_{\dot{\gamma}_i}^{\dot{\gamma}_j} \sigma(\dot{\gamma}) \dot{\gamma} d\dot{\gamma} \quad (5.18)$$

- Apply a first order Taylor expansion to $\sigma(\dot{\gamma})$:

$$\begin{aligned} \frac{\Sigma(\omega_j)}{C_j} - \frac{\Sigma(\omega_i)}{C_i} &= \int_{\dot{\gamma}_i}^{\dot{\gamma}_j} \left(\sigma(\dot{\gamma}_i) + \frac{d\sigma}{d\dot{\gamma}}(\dot{\gamma}_i) (\dot{\gamma} - \dot{\gamma}_i) \right) \dot{\gamma} d\dot{\gamma} \\ &= \frac{1}{2} \sigma(\dot{\gamma}_i) (\dot{\gamma}_j^2 - \dot{\gamma}_i^2) + \left(\frac{1}{3} (\dot{\gamma}_j^3 - \dot{\gamma}_i^3) + \frac{1}{2} (\dot{\gamma}_i \dot{\gamma}_j^2 - \dot{\gamma}_i^3) \right) \frac{d\sigma}{d\dot{\gamma}}(\dot{\gamma}_i) \end{aligned} \quad (5.19)$$

Note that $\sigma(\dot{\gamma}_i)$ and $\frac{d\sigma}{d\dot{\gamma}}(\dot{\gamma}_i)$ are constants here.

- Rewrite this to obtain the derivative of $\sigma(\dot{\gamma})$ at $\dot{\gamma}_i$:

$$\frac{d\sigma}{d\dot{\gamma}}(\dot{\gamma}_i) = \frac{\frac{\Sigma(\omega_j)}{C_j} - \frac{\Sigma(\omega_i)}{C_i} - \frac{1}{2} \sigma(\dot{\gamma}_i) (\dot{\gamma}_j^2 - \dot{\gamma}_i^2)}{\frac{1}{3} (\dot{\gamma}_j^3 - \dot{\gamma}_i^3) + \frac{1}{2} (\dot{\gamma}_i \dot{\gamma}_j^2 - \dot{\gamma}_i^3)} \quad (5.20)$$

4. Calculate $\sigma(\dot{\gamma}_j)$ from $\sigma(\dot{\gamma}_i)$ and the difference between $\Sigma(\omega_j)$ and $\Sigma(\omega_i)$:

$$\sigma(\dot{\gamma}_j) = \sigma(\dot{\gamma}_i) + \frac{d\sigma}{d\dot{\gamma}}(\dot{\gamma}_i) (\dot{\gamma}_j - \dot{\gamma}_i) \quad (5.21)$$

5. Set $\dot{\gamma}_i = \dot{\gamma}_j$

6. Repeat step 2-5 until the entire $\sigma(\dot{\gamma})$ function is reconstructed.

Results and Discussion

The goal of this research is to evaluate the internal electrical resistance of alginate-based SSFBs and its dependence on flow behaviour. The flow is simulated with a lattice Boltzmann fluid dynamics model and the internal resistance is computed with a finite volume model for the electric field. The rheological and electrical properties of the alginate-based electrolyte, which are important inputs for the model, have not been characterised yet. Therefore a non-aqueous carbon black suspension, which is more or less similar to the alginate electrolyte and which has been characterised, is used as a replacement (as discussed in section 2.5). Before the models are used to simulate the carbon black suspension, they must be validated. Section 6.1 validates and optimises the two lattice Boltzmann models with three benchmark fluids. Subsequently in section 6.2 the finite volume model is validated. Then, section 6.3 presents the results of fluid dynamics simulations of the carbon black suspension and the consecutive finite volume computation of internal resistance. The flow behaviour and corresponding resistance are evaluated for multiple inflow velocities. Additionally, this section checks the simulations for grid spatial convergence and assesses the impact of some major assumptions. Next, section 6.4 zooms out and reflects on the role of the carbon black electronic resistance in the total internal resistance. Finally, section 6.5 describes the validation of the conductivity conversion method that was introduced in chapter 5.

6.1. Validation of Fluid Dynamics Model

The LBM models are benchmarked by simulating the parallel plate flow of three simple fluids: Newtonian (constant viscosity, $n = 1$), shear thickening ($\nu = (K/\rho)\dot{\gamma}^{n-1}$; $n = 2$) and shear thinning ($\nu = (K/\rho)\dot{\gamma}^{n-1}$; $n = 0.2$). By comparison of the simulation results to the analytical solution the MRT and FMLB lattice Boltzmann models are validated and the best combination of boundary techniques is found.

6.1.1. Analytical Solution

The parallel plate geometry is schematically depicted in figure 6.1. In the fluid dynamics simulations

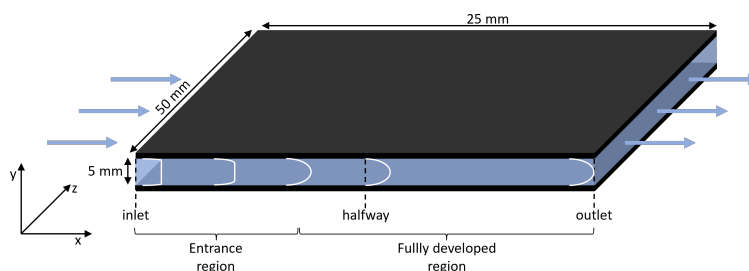


Figure 6.1: Schematic illustration of parallel plate flow geometry. The blue arrows give the direction of the flow. The entrance region for developing flow and the fully developed region are distinguished.

the system is assumed to be two dimensional by disregarding the z dependence. As explained in section 3.3 this approximation is valid for parallel plates which are relatively wide. Equation 6.1 gives the analytical solution of a fully developed flow of a power law fluid between parallel plates [53].

$$\vec{u}(x, y) = \begin{pmatrix} u_x^{in} \frac{2n+1}{n+1} \left(1 - \left(\frac{2|y - \frac{N_y \Delta y}{2}|}{N_y \Delta y} \right)^{\frac{n+1}{n}} \right) \\ 0 \end{pmatrix} \quad (6.1)$$

Where u_x^{in} is the inlet velocity and $\Delta y N_y = H$ the height of the channel. This equation assumes a constant fluid density throughout the flow channel. In the lattice Boltzmann method, however, density is 1-to-1 related to pressure (as described by equation 2.13). Wall friction results in a pressure decrease in the flow direction, and hence in a density gradient. Consequently, in order to obey the law of conservation of mass, the average velocity increases in the flow direction. For that reason mass flux profiles, rather than velocity profiles, are plotted to validate the models. Mass flux is defined as the product of velocity and density: $\rho(x, y)\vec{u}(x, y)$.

When the fluid enters the computational domain, the velocity is uniform ($u_x^{in}(x = 0, y) = u_{in}$). Only after traveling some distance the flow is fully developed and can be compared to the analytical solution. The length of the entrance region depends on channel geometry, flow velocity and fluid properties.

6.1.2. Boundary Conditions

In section 3.4 various techniques for the in- and outlet boundary condition were discussed. The three benchmark cases (parallel plate flow of shear thinning, Newtonian and shear thinning fluids) were used to find the optimal combination of boundary techniques. Simulations were run for all combinations of boundary techniques that were presented in section 3.4 for both the MRT and the FMLB model and for all 3 benchmark fluids. The results are presented in appendix A. This analysis shows the importance of the choice of boundary techniques: for some combinations of boundary techniques the model is unstable or does not reproduce the analytical solution. The MRT model gives the best results with the extrapolation method at the outflow in combination with the bounce back method at the inflow. For FMLB the best combination of boundary techniques is the Neumann method for the outflow and either bounce back or non-equilibrium bounce back at inflow. To have more similarity with the MRT model, the bounce back method was chosen for the inflow of the FMLB model. These boundary techniques are used in the fluid dynamics simulations presented in the remainder of this chapter.

6.1.3. Benchmarking

This section presents the results of the benchmark study. The flow of the three benchmark fluids between parallel plates was simulated with the following input parameters: $height = H = 5 \text{ mm}$, $length = L = 25 \text{ mm}$, $u_x^{in} = 0.01 \text{ ms}^{-1}$, $N_x = 250$, $N_y = 50$, initial density $\rho_0 = 1 \times 10^3 \text{ kgm}^{-3}$. The properties of the benchmark fluid are specified in table 6.1. For shear thinning fluids the viscosity

Table 6.1: Fluid characteristics.

Fluid type	Kinematic viscosity
Newtonian ($n = 1$)	$\nu = 2 \times 10^{-6} \text{ m}^2/\text{s}^{-1}$
Shear thinning ($n = 0.2$)	$\nu = \begin{cases} v_{max} = 0.30 \text{ m}^2/\text{s} & \text{if } \dot{\gamma} < \dot{\gamma}_{cutoff} = 0.0045 \text{ s}^{-1} \\ (K/\rho)\dot{\gamma}^{n-1} & \text{otherwise} \end{cases} \quad \frac{K}{\rho} = 0.004 \text{ m}^2/\text{s}^{1.8}$
Shear thickening ($n = 2$)	$\nu = (K/\rho)\dot{\gamma}^{n-1} \quad \frac{K}{\rho} = 1 \times 10^{-5} \text{ m}^2$

goes to infinity at zero shear rate because $n - 1 < 0$. In the fully developed region the shear rate (which is composed of four components $\frac{\partial u_x}{\partial x}$, $\frac{\partial u_x}{\partial y}$, $\frac{\partial u_y}{\partial x}$ and $\frac{\partial u_y}{\partial y}$) is zero in the center of the channel ($y = H/2$):

- u_y is zero everywhere which means that $\frac{\partial u_y}{\partial x} = \frac{\partial u_y}{\partial y} = 0$.
- As a results of the symmetry of the flow channel $\frac{\partial u_x}{\partial y} = 0$ in the center.
- In the entrance region $\frac{\partial u_x}{\partial x} \neq 0$, while in the fully developed region $\frac{\partial u_x}{\partial x} = 0$ (see figure 6.1 for a definition of the regions).

To prevent the viscosity from going to infinity it is capped at $v_{max} = 0.30 \text{ m}^2/\text{s}$. This means that for shear rates below $\dot{\gamma}_{cutoff} = (v_{max}\rho/K)^{1/(n-1)} = 0.0045 \text{ s}^{-1}$ the viscosity is set at v_{max} . It is expected that this will not yield large errors: for shear thinning fluids with n -values close to 1 the profile will look very much like the parabola of Newtonian fluids and the viscosity will only be capped in a narrow region around the center. The stronger shear thinning the fluid (lower n), the more the profile will look like plug flow with a steep increase at the walls and flat in the middle. In that case the shape of the profile is primarily determined by the viscosity close to the walls, which is orders of magnitude lower than the viscosity in the center.

Lattice Boltzmann simulations typically are performed in dimensionless lattice units. This means that physical quantities are non-dimensionalised. Conversion factors give the relation between the dimensionless lattice parameters and their physical counterparts [38]. Appendix B provides an overview of the simulation parameters in lattice units.

Figures 6.2 and 6.3 show the mass flux profiles and their relative errors of respectively the MRT model and the FMLB model. The error is calculated as:

$$\epsilon_{\rho u_x}(y) = \left| \frac{(\rho u_x)^{simulation}(y) - (\rho u_x)^{analytical}(y)}{(\rho u_x)^{analytical}(y)} \right| \cdot 100\% \quad (6.2)$$

The mass flux profiles show a good correspondence with the analytical solutions. For $N_x \times N_y = 250 \times 50$ the average error stays below 0.7%. This means that both the MRT and the FMLB model are capable of simulating the mass flux profiles of Newtonian ($n = 1$), shear thinning ($n = 0.2$) and shear thickening ($n = 2$) fluids between parallel plates for the given input parameters. Capping the kinematic viscosity of shear thinning fluids at $0.30 \text{ m}^2\text{s}^{-1}$ did not significantly affect the flow behaviour.

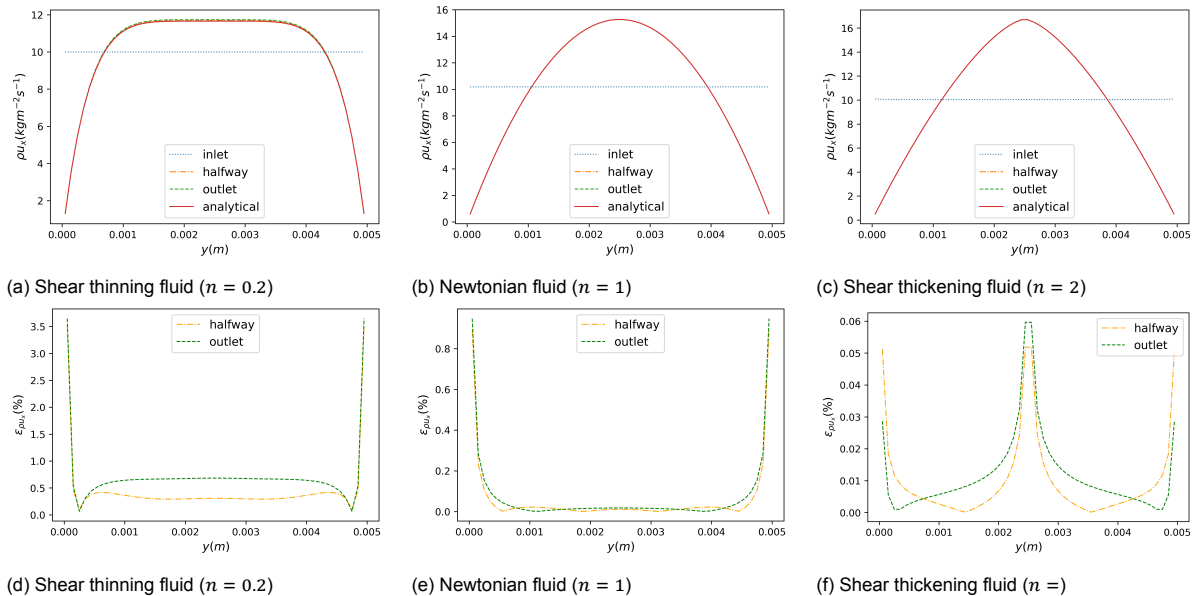


Figure 6.2: Mass flux profiles and their errors obtained with MRT model for three fluids: shear thinning, Newtonian and shear thickening. Top row: The x -velocity as a function of y -location at the inlet, halfway and at the outlet of the channel are plotted along with the analytical solution. Bottom row: The error with respect to the analytical solution as a function of y -location are plotted halfway the channel and at the outlet.

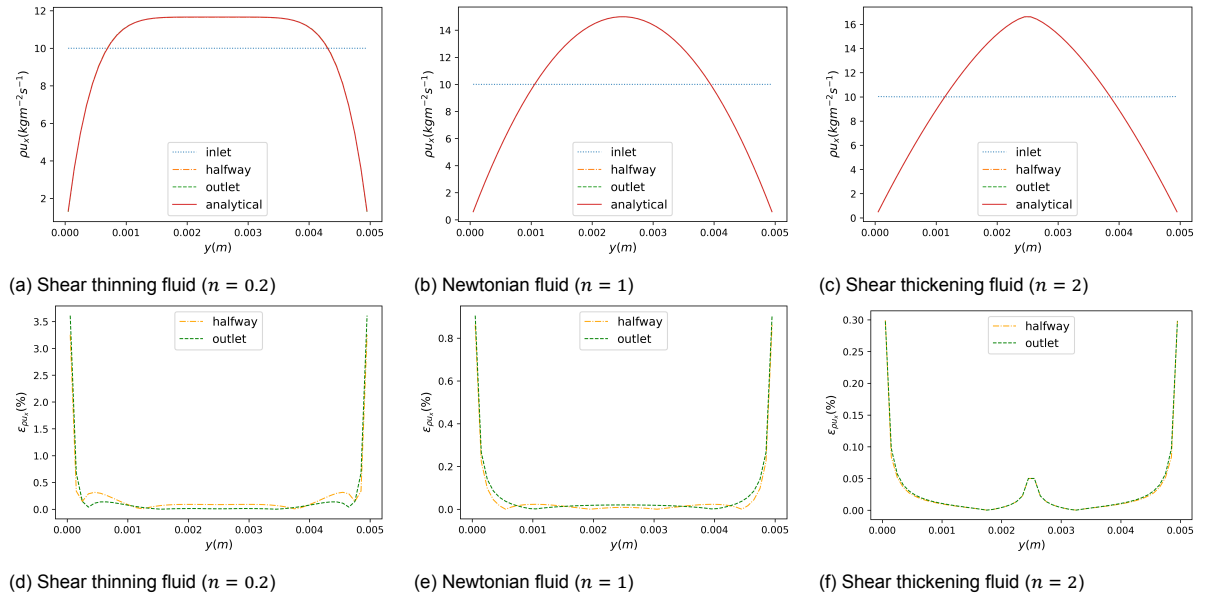


Figure 6.3: Mass flux profiles and their errors obtained with FMLB model for three fluids: shear thinning, Newtonian and shear thickening. Top row: The x-velocity as a function of y-location at the inlet, halfway and at the outlet of the channel are plotted along with the analytical solution. Bottom row: The error with respect to the analytical solution as a function of y-location are plotted halfway the channel and at the outlet.

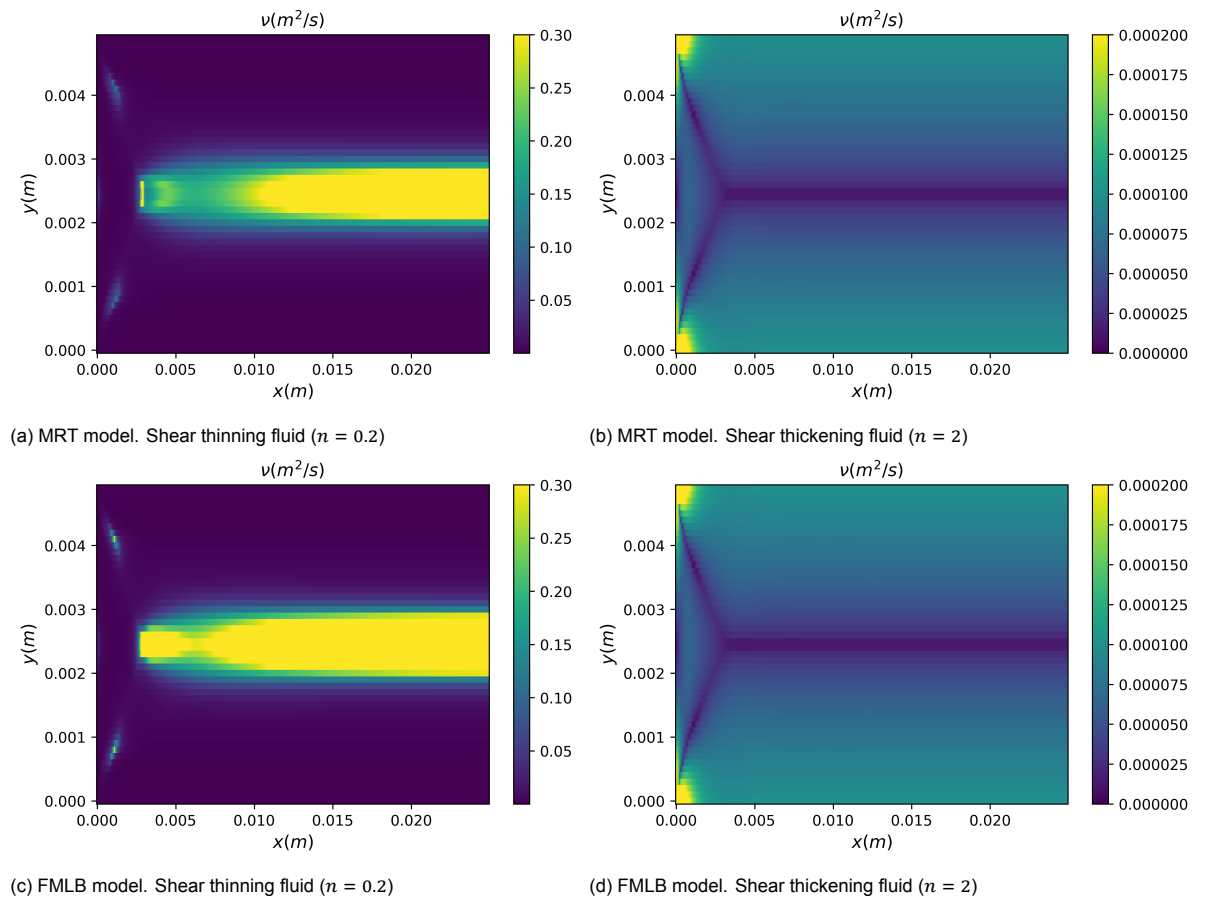


Figure 6.4: Kinematic viscosity obtained with MRT (top row) and FMLB (bottom row) model for shear thinning (left) and shear thickening (right) fluids. For the shear thinning fluid there is a clear discrepancy between the two methods.

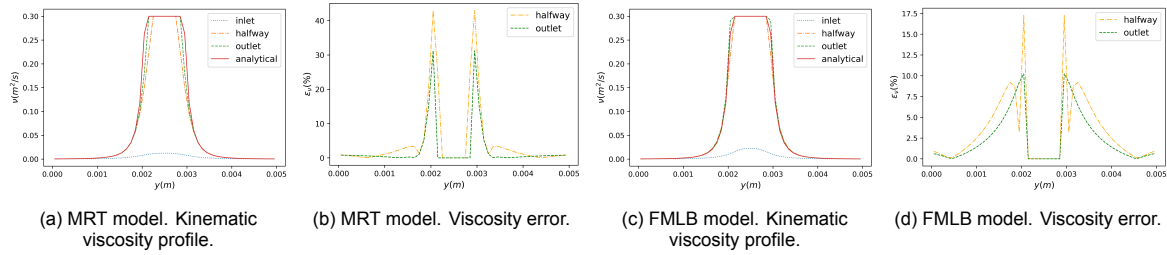


Figure 6.5: Kinematic viscosity profile and relative viscosity error of shear thinning fluids obtained with MRT (a and b) and FMLB (c and d) model. For both models the relative viscosity error is higher than the relative velocity error.

Figure 6.4 shows the kinematic viscosity of the power law fluids as a function of position. From these figures it is clear that the flow does not change significantly at the outlet. This means that the outflow boundary condition is functioning properly. When taking a closer look at the kinematic viscosity of the shear thinning fluids, a difference between the MRT and FMLB result of the shear thinning fluid is observed. This is more obvious when plotting the kinematic viscosity profiles and relative viscosity errors (figure 6.5). The kinematic viscosity obtained with the FMLB model corresponds better to the analytical solution than that of the MRT model. For both models the relative viscosity error is much higher than the relative velocity error. For shear thinning fluids like these, viscosity at low shear rates depends strongly on the shear rate. As a result, small inaccuracies in velocity (and hence shear rate) result in large viscosity inaccuracies.

6.1.4. Wall Friction

Chapter 2.2.4 introduces two methods to calculate the wall friction. One method computes the wall friction from the pressure drop over the flow channel ($F_{pressure}$, equation 2.17). The other method uses the shear stress at the walls (F_{shear} , equation 2.18). These methods should give the same result. The results of the friction force calculations and their relative error (equation 6.3) for the six benchmarks are presented in table 6.2.

$$\epsilon = \left| \frac{F_{shear} - F_{pressure}}{\frac{1}{2}(F_{shear} + F_{pressure})} \right| \cdot 100\% \quad (6.3)$$

Table 6.2: Force calculation

		$n = 0.2$	$n = 1$	$n = 2$
MRT	$F_{shear}(N)$	0.0198	9.72×10^{-5}	0.005 31
	$F_{pressure}(N)$	0.0201	9.26×10^{-5}	0.005 04
	$\epsilon(\%)$	1.5	4.9	5.3
FMLB	$F_{shear}(N)$	0.0199	8.05×10^{-5}	0.005 34
	$F_{pressure}(N)$	0.0201	8.83×10^{-5}	0.004 57
	$\epsilon(\%)$	1.2	9.8	17

For Newtonian and shear thickening fluids the relative error (marked in red) is large ($> 4\%$). This can be explained when looking at the pressure in the flow channel:

- In figure 6.6 the average pressure along the channel length of a shear thickening fluid is plotted for various grids. From this figure it is clear that the pressure at the inlet ($x \lesssim 2$ mm) is not grid-independent, while the pressure in the rest of the channel is. This indicates non-physical behaviour in the inlet region.
- Additionally, the density profiles along the length of the channel were plotted for all six benchmark studies (figure 6.7). Both the average density and the density at the walls are given. The calculation of $F_{pressure}$ is based on the average density. In the inlet region the average density is much lower than the wall density. This density gradient in y -direction results in a nonzero y -velocity u_y . In reality the flow has no y -component. The region of the channel with nonzero density gradient in y -direction thus does not describe the physical situation. When comparing wall density

and average density for all six cases, it is observed that the difference between wall density and average density is highest for the shear thickening fluid, followed by the Newtonian fluid and the shear thinning fluid. This is in accordance with the observation that the force error is largest for shear thickening fluids, followed by Newtonian fluids and shear thinning fluids.

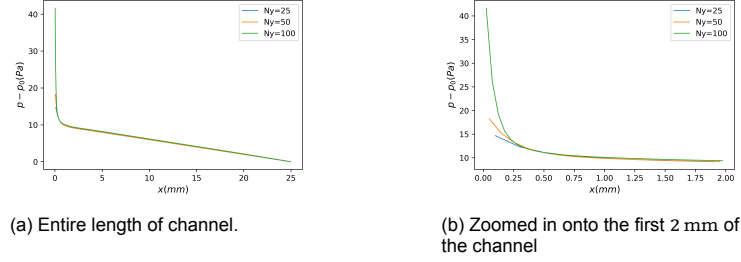


Figure 6.6: Average pressure along the channel length in shear thickening fluid for 3 different grids: $N_x \times N_y = 125 \times 25$, $N_x \times N_y = 250 \times 50$ and $N_x \times N_y = 500 \times 100$. Results were obtained with the FMLB model. The pressure is not grid-independent in the first 2 mm (right).

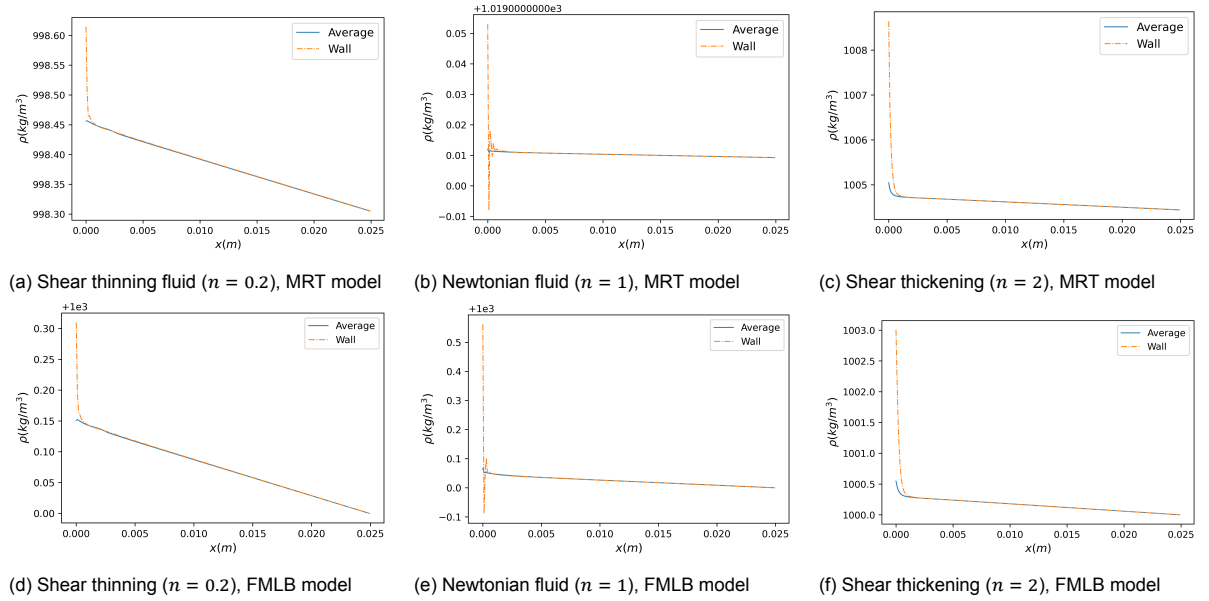


Figure 6.7: Density profiles along the length of the channel for three fluids (shear thinning, Newtonian and shear thickening) and for both the MRT (top row) and FMLB (bottom row) model. The average density (blue) and density alongside the channel wall (orange) are plotted. In the inlet region there is a clear deviation between the two curves.

It is concluded that the behaviour at the inlet of the flow channel is non-physical. When excluding the non-physical inlet region from the force calculation the relative errors are much smaller. The wall friction force and relative errors when excluding the first 2.5 mm of the channel are listed in table 6.3. All errors stay below 2%. This however leads to an underestimation of the wall friction and pumping power. The simulation is incapable of correctly describing the behaviour at the inlet of the channel properly. This is especially of importance in relatively short channels like these ($length/height = 5$). The remaining error partly is a result of the extrapolation error of the shear stress at the walls. Since the lattice points are located $\frac{\Delta x}{2}$ away from the channel wall, the shear stress at the walls is calculated by linear extrapolation of the values in the neighbouring points.

A possible explanation for the non-physical behaviour at the inlet is the combination of inlet and wall boundary condition. The inlet boundary condition imposes a uniform velocity while the wall boundary condition imposes zero velocity at the walls. These two conditions contradict each other. This hypothesis is supported by the observation that for lower inlet velocities the relative difference between wall

Table 6.3: Force calculation

		$n = 0.2$	$n = 1$	$n = 2$
MRT	$F_{shear}(N)$	0.175	5.67×10^{-5}	0.002 23
	$F_{pressure}(N)$	0.0177	5.75×10^{-5}	0.002 22
	$\epsilon(\%)$	0.99	1.4	0.70
FMLB	$F_{shear}(N)$	0.0175	5.47×10^{-5}	0.002 25
	$F_{pressure}(N)$	0.0177	5.53×10^{-5}	0.002 23
	$\epsilon(\%)$	1.1	1.1	0.71

density and average density is smaller.

In summary, the wall friction calculation is corrupted in the inlet region where the simulation does not represent the physical behaviour correctly. This is clear to see from the non-converging inflow behaviour and steep density gradient in y -direction. When excluding the first part of the channel in the calculation the two calculations of friction force are in accordance with each other but underestimate the total friction force.

6.2. Validation of Finite Volume Method

This section describes the validation of the finite volume method for the electric field in the flow channel. A schematic illustration of the flow channel is given in figure 6.1. First of all, there are two simple checks to verify if the results of the FVM correspond to the governing equations.

1. The governing differential equation (equation 2.25) requires the net current through any closed contour that lies within the computational domain (i.e. not enclosing the parallel plates or the edge of the domain) to be zero. For all FVM simulations the net current through any chosen closed contour must be zero within machine precision.
2. The current flow from the lower to the upper plate and cannot leave the channel because there are no sources or sinks in the channel. Therefore the total current in y -direction should be constant in the flow channel and zero outside the channel (e.g., figure 6.8).

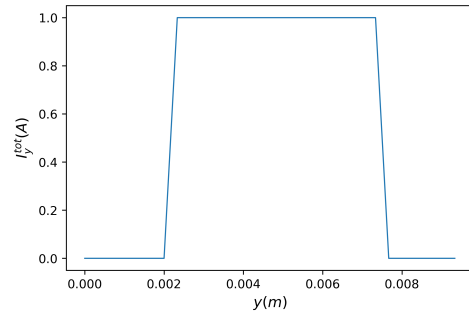


Figure 6.8: The total current in y direction should be constant and non-zero in the flow channel and zero outside the flow channel.

All simulations presented in this chapter have passed these verification tests. Next to that, a benchmark study was performed to validate the model and to assess errors that stem from assumptions. The benchmark case is a flow channel with homogeneous conductivity. The analytical solution of the resistance and the electric field are known. The model inputs are listed below:

- $length = L = 5 \times 10^{-2}$ m, $height = H = 5 \times 10^{-3}$ m, $width = W = 5 \times 10^{-2}$ m
- Width of surrounding medium $W_{surr} = 2.5 \times 10^{-3}$ m
N.B. For a wider surrounding medium the assumption of zero electric potential is more accurate (as explained in chapter 4). Hence, it is expected that the relative error in the resistance calculation decreases with the surrounding medium width.
- $\Delta x = \Delta y = 0.5 \times 10^{-3}$ m, $\Delta z = W$
- $V_{max} = 1$ V

$$\sigma(x, y) = \begin{cases} 1 \text{ Sm}^{-1} & \text{flow channel} \\ 1 \times 10^{-10} \text{ Sm}^{-1} & \text{surrounding medium} \end{cases}$$

N.B. Setting the conductivity of the surrounding medium to 0 Sm^{-1} results in a singular matrix \mathbf{M} . Therefore the conductivity is set at a finite but small value.

Equation 6.4 gives the analytical solution for the resistance of a cuboid with homogeneous resistance.

$$R = \frac{\rho l}{A} = \frac{H}{\sigma WL} = 2\Omega \quad (6.4)$$

The analytical solution for the electric field in a parallel plate capacitor is given by equation 6.5. In this equation the parallel plates are assumed to be infinitely wide.

$$|\vec{E}| = \frac{\Delta V}{d} = \frac{2V_{max}}{H} = 400 \text{ V m}^{-1} \quad (6.5)$$

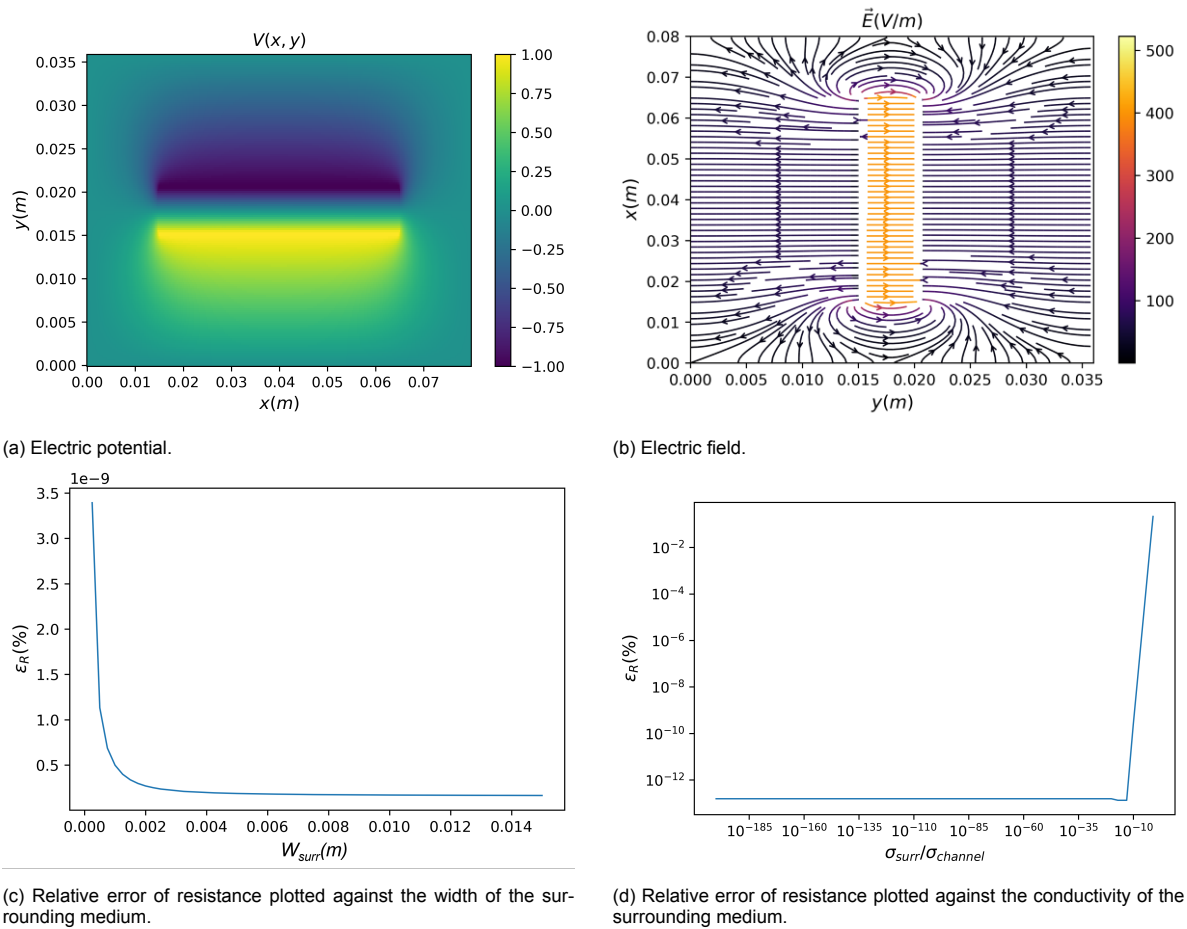


Figure 6.9: Results of finite volume simulations of a homogeneous cuboidal conductor over which a voltage is applied. Top row: The electric field and electric potential are plotted for a surrounding medium width of 15 mm and relative conductivity $\sigma_{surr}/\sigma_{channel} = 1 \times 10^{-10}$. (The two images are rotated 90 with respect to each other.) Bottom row: The error of the internal resistance with respect to its theoretical value is plotted for a range of widths and conductivities of the surrounding medium.

The FVM simulation was run to determine the electric field and compute the resistance. The electric potential and electric field are plotted in figures 6.9a and 6.9b respectively. The electric field between the plates is constant and corresponds to the analytical value of 400 V m^{-1} . The resistance is found to be $(2+4.7 \times 10^{-12}) \Omega$ with a relative error of $2.4 \times 10^{-10} \%$ with respect to the analytical value. It can be concluded that the finite volume simulation accurately represents the physical situation.

The error caused by the finite width of the surrounding medium is evaluated by repeating the simulation for a range of widths W_{surr} . The relative error is plotted against the width and shown in figure 6.9c. The relative error is smaller than $4 \times 10^{-9} \%$ for a width of one lattice spacing ($0.25 \times 10^{-3} \text{ m}$) and, as predicted, decreases with increasing width. It should be noted that the size of the matrix \mathbf{M} is limited by the random access memory. Consequently, a wider surrounding medium is at the cost of spatial resolution. The width of the surrounding medium is set to 5 lattice spacings for the finite volume simulations in the remainder of this chapter. This is sufficiently high to keep the error small. Likewise, the error as a result of the non-zero conductivity of the surrounding medium was evaluated by running the simulation for a range of conductivities of the surrounding medium. The results are presented in figure 6.9. As expected, the relative error decreases exponentially with decreasing conductivity until it reaches a plateau of $1.6 \times 10^{-13} \%$ at $\sigma_{surr}/\sigma_{channel} \approx 1 \times 10^{-20}$. The relative conductivity of the surrounding medium is set to $\sigma_{surr}/\sigma_{channel} = 1 \times 10^{-10}$ for the finite volume simulations in the remainder of this chapter.

In conclusion, the model accurately represents a physical system. In this benchmark study the relative error of the resistance was below $4 \times 10^{-9} \%$ for all combinations of input parameters that were used. This is more than adequate for the purpose of this study.

6.3. Flow Behaviour and Resistance of Carbon Black Suspension

This section discusses the flow behaviour and internal resistance of the nonaqueous carbon black suspension that was introduced in chapter 2.5. The flow channel has a height of 5 mm, a length of 25 mm and a width of 50 mm. To compute the internal resistance, the fluid dynamics model is run first to obtain the flow profile, pumping power and shear rate. Based on this, the conductivity is calculated with equation 2.32. The resulting conductivity field ($\sigma(x, y)$) is used as input for the finite volume model that computes the internal resistance.

In the computation of the pumping power and internal resistance, the first part of the channel is excluded to avoid the non-physical inlet region (see section 6.1.4). It should be noted that the length of the non-physical region differs per simulation (depending on factors such as inlet velocity and grid size). To ensure a fair comparison, the length of the inlet region of all simulations must be set at the same value. Therefore the length of the excluded region is set at a 10 % of the total length for all simulations. This estimation is based on the analysis that was presented in section 6.1.4.

6.3.1. Grid Convergence

In this section the spatial grid convergence of FMLB and MRT simulations of the carbon black suspension is examined. In a grid convergence study the grid is refined multiple times until the results do not change anymore upon further refinement. A simulation of the carbon black suspension flowing through the channel with inflow velocity 0.01 m s^{-1} was performed for various grids. The results are compared to each other by plotting the mass flux, shear rate, kinematic viscosity and conductivity profiles (taken halfway in the channel) for various grids on top of each other. The results of the FMLB and MRT models are presented respectively in figure 6.10 and 6.11.

FMLB Grid Convergence

The FMLB simulation results of the $N_x \times N_y = 775 \times 155$ and $N_x \times N_y = 1035 \times 207$ grid overlap, indicating grid convergence. This is substantiated when assessing the resistivity ($\rho = \sigma^{-1}$) in the flow channel and the internal resistance. The resistivity on the $N_x \times N_y = 775 \times 155$ grid (figure 6.12) and on the $N_x \times N_y = 1035 \times 207$ grid (figure 6.13) look identical. The internal resistances are listed in table 6.4 along with their relative error with respect to the resistance of the finest grid. The relative error decreases with number of grid points and is only 0.2 % for the 775×155 grid. For the computation of the internal resistance the conductivity of the two finest grids (155×775 and 207×1035) was mapped onto a coarser grids before using it as input of the finite volume model because the size of \mathbf{M} matrix ($N_x N_y \times N_x N_y$) is limited by the computer's available random access memory.

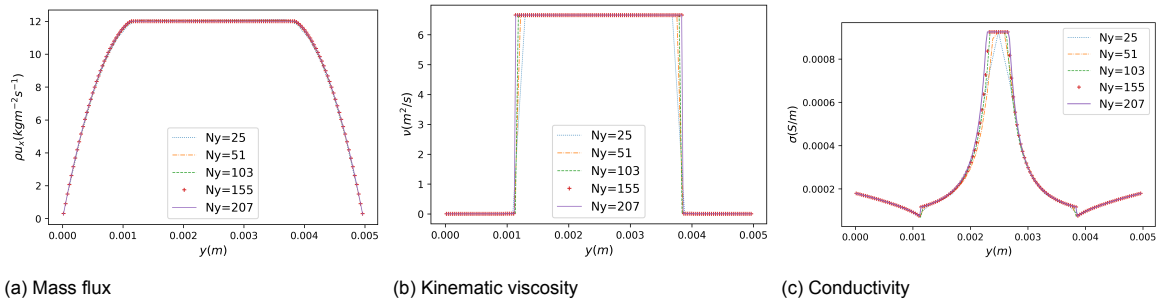


Figure 6.10: Results of grid convergence study of FMLB simulation of carbon black suspension flowing between two parallel plates. Mass flux, shear rate, kinematic viscosity and conductivity profiles halfway the channel are plotted for various grids: $N_y = 25, 52, 103, 155, 207$ ($N_x = 5 \times N_y$). The profiles of the two finest grids overlap indicating grid convergence.

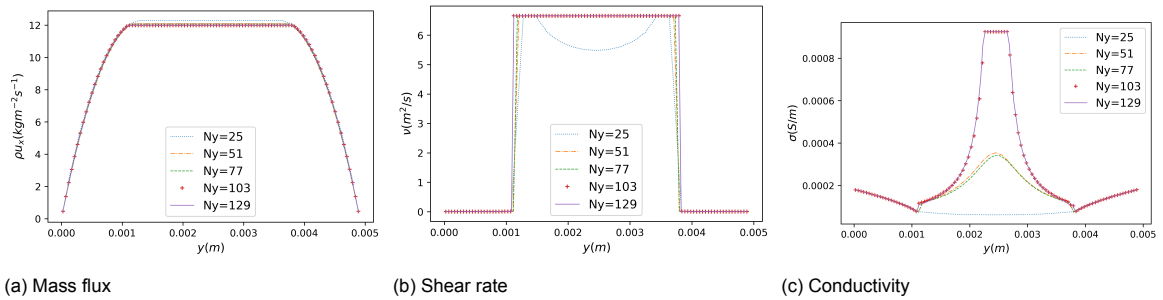


Figure 6.11: Results of grid convergence study of MRT simulation of carbon black suspension flowing between two parallel plates with. Mass flux, kinematic viscosity and conductivity profiles halfway the channel are plotted for various grids: $N_y = 25, 52, 77, 103, 155$ ($N_x = 5 \times N_y$). The profiles of the two finest grids overlap indicating grid convergence.

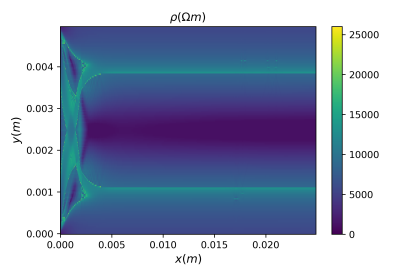


Figure 6.12: Resistivity of carbon black suspension flowing between two parallel plates on $N_x \times N_y = 755 \times 155$ grid. Obtained with FMLB simulation.

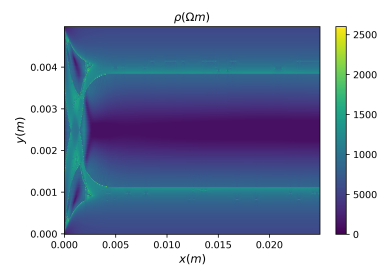


Figure 6.13: Resistivity of carbon black suspension flowing between two parallel plates on $N_x \times N_y = 1035 \times 207$ grid. Obtained with FMLB simulation.

Table 6.4: Internal resistance of carbon black suspension flowing between two parallel plates for various grids and their relative error with respect to the internal resistance of the finest grid.

N_y	$R(\text{k}\Omega)$	$\epsilon(\%)$
25	27.35	2.0
51	27.44	2.4
103	27.40	2.2
155	26.75	0.2
207	26.81	0

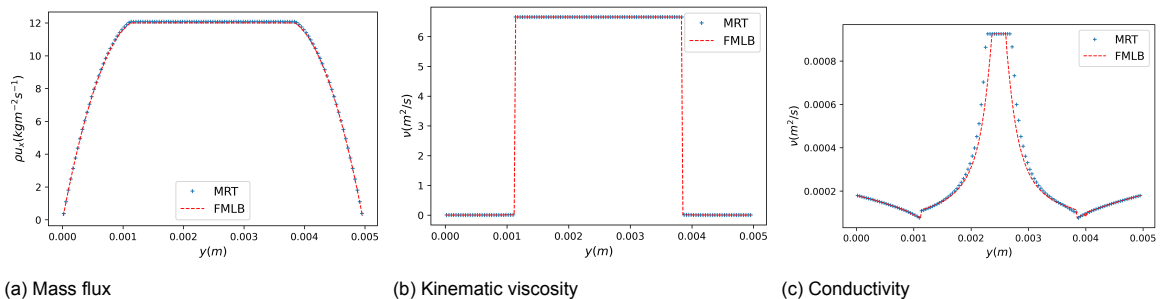


Figure 6.14: Results of FMLB ($N_x \times N_y = 1035 \times 207$) and MRT ($N_x \times N_y = 645 \times 129$) simulation of carbon black suspension flowing between two parallel plates.

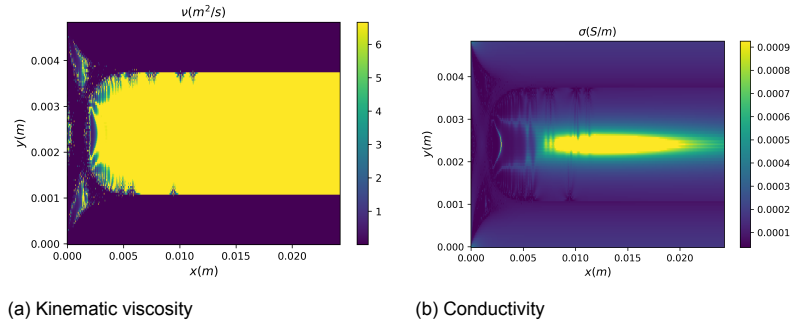


Figure 6.15: Kinematic viscosity and conductivity of carbon black suspension flowing between two parallel plates on $N_x \times N_y = 645 \times 129$ grid. Obtained with MRT simulation. There are clear asymmetries in both figures. In addition, the conductivity map shows bad outflow convergence.

MRT Grid Convergence

The profiles of the $N_x \times N_y = 515 \times 103$ and $N_x \times N_y = 645 \times 129$ grid overlap, indicating grid convergence. Moreover, the profiles of the MRT and FMLB are almost identical (figure 6.14) which is another indication for spatial grid convergence. However, the kinematic viscosity and conductivity (figure 6.15) obtained with the MRT model show asymmetric behaviour and bad outflow convergence (i.e. the conductivity changes at the outflow). Furthermore, the MRT model is unstable for grids with resolution of $N_x \times N_y = 775 \times 155$ or higher. It was therefore concluded that, while the MRT and FMLB models performed comparably in the benchmark cases presented in section 6.1.3, the FMLB model is better suited for simulations of the carbon black suspension. Unless otherwise specified the FMLB method is used for the fluid dynamics simulations in the remainder of this chapter.

6.3.2. Internal Resistance Optimization

This section assesses the internal resistance for various flow geometries. Both the inflow velocity u_x^{in} and the channel height H can be varied. It should be noted that shear rate scales linearly with u_x^{in}/H . Therefore increasing the velocity by a certain factor yields the same shear rate as decreasing the channel height by the same factor. Considering that viscosity and conductivity both are direct functions of shear rate, any simulation with the same value of u_x^{in}/H yields the same results for shear rate, viscosity and conductivity (provided that the flow is laminar). Therefore only one of the two parameters needs to be varied.

The internal resistance of the carbon black suspension was computed for five inflow velocities ($u_x^{in} \in [0, 0.001, 0.01, 0.1, 1.0] \text{ m s}^{-1}$). The conductivity of the carbon black suspension has a maximum of $9 \times 10^{-4} \text{ Sm}^{-1}$ (figure 2.7) for shear rates below $10 \times 10^{-3} \text{ s}^{-1}$. Hence, the internal resistance is lowest when the flow battery is operated in batch mode (zero velocity and thus no shear stress). The lowest attainable resistance of a flow channel with dimensions $5 \times 22.5 \times 50 \text{ mm}$ is $4.94 \text{ k}\Omega$ (equation 6.4). In figure 6.16 the flow channel resistivity is plotted for the four non-zero inflow velocities. To compare the results of the various inflow velocities, the resistivity profiles halfway the channel are plotted in figure 6.17 and the internal resistances are listed in table 6.5.

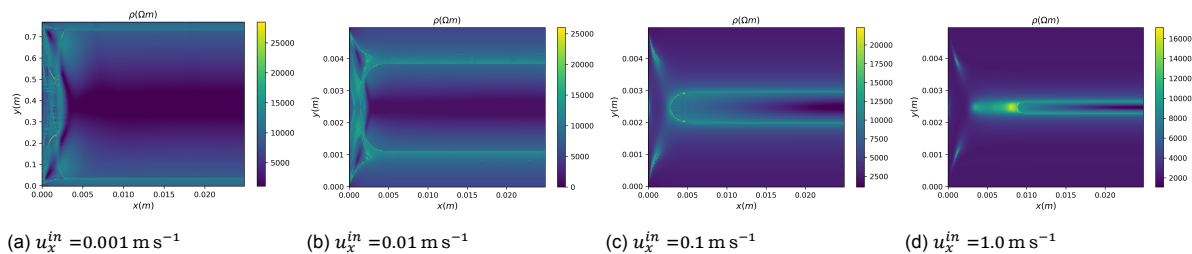


Figure 6.16: Resistivity of carbon black suspension flowing between two parallel plates for various inlet velocities (u_x^{in}). The results have been checked for grid convergence.

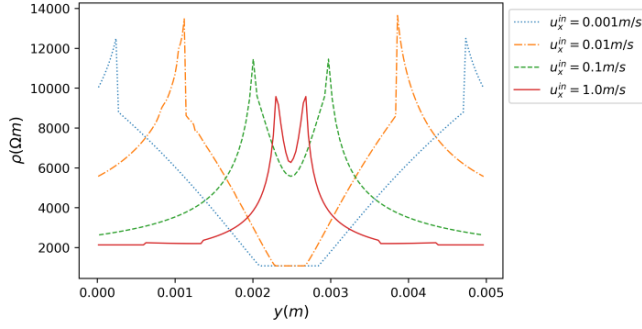


Figure 6.17: Resistivity profile of carbon black suspension flowing between two parallel plates for various inlet velocities. The profiles are taken halfway the channel.

Table 6.5: Internal resistance and pumping power of carbon black suspension flowing between two parallel plates for various inflow velocities.

u_x^{in}	R (k Ω)	$P_{pumping}$ (W)	ϵ_P (%)
0	4.94	0	0
0.001	23.9	1.0×10^{-4}	9
0.01	26.8	1.6×10^{-3}	1
0.1	20.9	4.7×10^{-2}	0.2
1.0	14.2	1.3	1

All resistivity profiles have two peaks separated by a local minimum in the middle of the channel. The local minimum stems from a low shear rate in the middle. As explained in section 6.1.3 the shear rate in the center of the channel is zero in the fully developed region and nonzero in the entrance region because of the $\frac{\partial u_x}{\partial x}$ component. The resistivity profiles of the simulations with inflow velocity 0.01 m s^{-1} and 0.001 m s^{-1} are taken in the fully converged regions while the profiles of the two higher velocities are taken in the entrance region. This explains why the local minimum of the former two simulations reaches the plateau corresponding to zero shear rate while the local minima of the later two simulations are higher. It is expected that in any fully developed flow between two parallel plates, the resistivity will have a local minimum of $1/9 \times 10^{-4} \Omega \text{ m}$ in the center. This hypothesis is supported by the observation that for the simulation with inflow velocity 0.1 m s^{-1} , the resistivity profile at the outlet also reaches the plateau of $1/9 \times 10^{-4} \Omega \text{ m}$ in the center.

The peaks surrounding the local minimum stem from the conductivity dip at a shear rate of approximately $1 \times 10^{-1} \text{ s}^{-1}$ (see figure 2.7). The shear rate is low in the middle of the channel and high along the edges. In between these two extremes the shear rate reaches the value of $1 \times 10^{-1} \text{ s}^{-1}$ resulting in a resistivity peak. Theoretically all peaks should have the same maximum. This is not the case here due to the spatial discretisation: the shear rate in the simulation never reaches $1 \times 10^{-1} \text{ s}^{-1}$ exactly. The internal resistance is highest for $u_x^{in} = 0.01 \text{ m s}^{-1}$ and lowest for $u_x^{in} = 1.0 \text{ m s}^{-1}$. The higher the peak, the higher the internal resistance. There are two ways to reduce the internal resistance:

- Operating the flow battery at very low inflow velocities such that the shear rate always stays well below $1 \times 10^{-1} \text{ s}^{-1}$. For a flow channel with a height of 5 mm the velocity would have to be significantly lower than 0.001 m s^{-1} . This is almost equivalent to operating the flow battery in batch mode.
- Alternatively the internal resistance can be reduced by using high inflow velocities (i.e. significantly higher than 0.1 m s^{-1} for a 5 mm high channel). At high velocities the range of shear rate range is very wide such that the two resistivity peaks are narrow. It would be interesting to run the simulation for even higher velocities. In this research this was not an option because the viscosity-cutoff at high shear rates (as will be discussed in section 6.3.4) would affect the reliability the results of the simulation too much. The viscosity must therefore be determined for a wider range of shear rates.

6.3.3. Pumping Power

This section assesses the pumping power for the simulations presented in section 6.3.2. The pumping power is computed from the wall friction according to equation 2.19. As previously discussed, there are two ways to compute the friction force. The computations should have the same outcome. Table 6.5 presents the results of the pumping power computation. The pumping power $P_{pumping}$ is the average of the two computation methods, ϵ_P represents the relative error between the methods.

In figure 6.18 the pumping power is plotted for four inlet velocities. On a double logarithmic scale the curve is approximately linear which indicates a power law relation between the pumping power and the inlet velocity. From the slope of the curve the power law exponent is found to be ~ 1.5 . This steep relation between pumping power and velocity should be taken into consideration when operating the flow battery at high inlet velocities. The pumping losses diminish the efficiency of the flow battery and should therefore be kept within bounds.

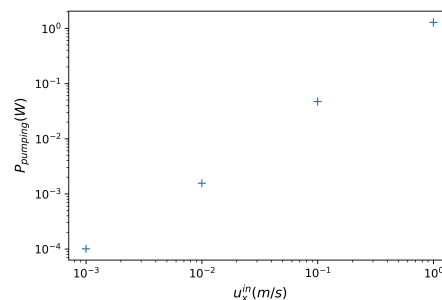


Figure 6.18: Pumping power plotted for various inlet velocities.

The relative error of the simulation with inlet velocity 0.001 m s^{-1} is 9%. The errors in the other simulations are smaller than 2%. Analogous to the analysis in section 6.1.4, the large error in the simulation with inlet velocity 0.001 m s^{-1} can be explained when plotting the density profile along the length of the channel. In figure 6.19 the average density and wall density are plotted. The green vertical line marks the location of the cutoff (at $1/10^{\text{th}}$ of the channel length). There is a clear difference between the graphs below 0.007 m . This means that the non-physical region of this simulation is larger than $1/10^{\text{th}}$ of the channel. When excluding the first 0.007 m of the channel in the pumping power computation the relative error between the two methods is reduced to 0.4%.

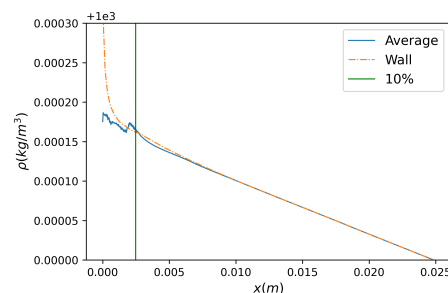


Figure 6.19: Density profile of carbon black suspension flowing between two parallel plates with inlet velocity of 0.001 m s^{-1} . Average density (blue) and density alongside the wall (orange) are plotted. The region on the left of the green vertical line is excluded in the computation of internal resistance and pumping power to avoid non-physical behaviour. The green line must be shifted to the right.

6.3.4. Effect of Viscosity-cutoff

Section 2.5 discusses the characterisation of the nonaqueous carbon black suspension. The viscosity and conductivity have been measured for a range of shear rate [22]. Curves were fit to the experimental results to obtain equations for viscosity and conductivity. These curves are used in the lattice Boltzmann models to compute viscosity and conductivity from shear rate. However, the shear rate range over which the viscosity and conductivity were measured is limited. By lack of a better assumption, the viscosity and conductivity are assumed to be constant outside the measurement range. To illustrate this, the kinematic viscosity of the four simulations that were discussed in section 6.3.2 are plotted as a function of shear rate in figure 6.20. The plateaus indicate viscosity cutoffs. For low inflow velocities the viscosity is only cut off at low shear rates (figure 6.20a) while for high inflow velocities the shear rates also reach the upper cutoff value (figures 6.20b, 6.20c and 6.20d). This section analyses the effect of the low shear rate cutoff and the high shear rate cutoff.

Viscosity-cutoff at Low Shear Rates

The effect of a viscosity-cutoff at low shear rates is studied by comparing two simulations with different cutoff shear rates:

- Kinematic viscosity is cut off at shear rate of 0.012 s^{-1} . Below this shear rate the kinematic viscosity is 6.7 m s^{-1} . This is the cutoff value that was used for all previous simulations.
- Kinematic viscosity is cut off at shear rate of 0.084 s^{-1} . Below this shear rate the kinematic viscosity is 0.70 m s^{-1} .

The inlet velocity of both simulation is 0.01 m s^{-1} . The results are shown in figure 6.21. While the velocity (figure 6.21a) and shear rate (figure 6.21d) profile look very similar, the conductivity profiles

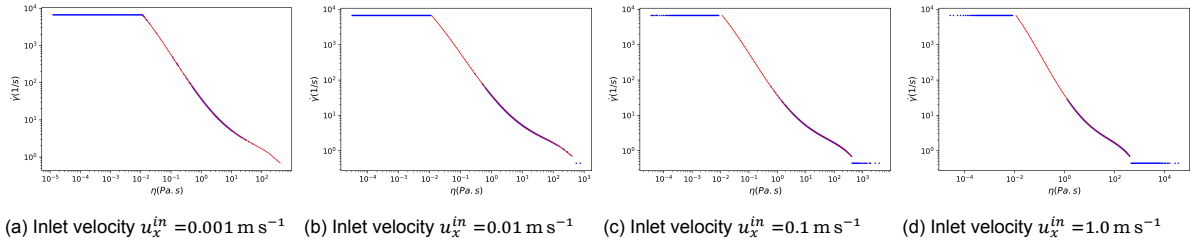


Figure 6.20: Kinematic viscosity as a function of shear rate in the flow channel for various inlet velocities. The red line gives the curve fit to the experimental value. The blue dots represent the actual shear rates and kinematic viscosities that occur in the flow channel. When the shear rate is outside the measured range, the kinematic viscosity stays constant resulting in plateaus at high and low shear rates.

(figure 6.21c) differ significantly. When zooming in on the shear rate profiles (figure 6.21e) a slight difference is observed. Because the conductivity is very sensitive in the low shear rate region, this slight difference in shear rate translates into a large difference in conductivity.

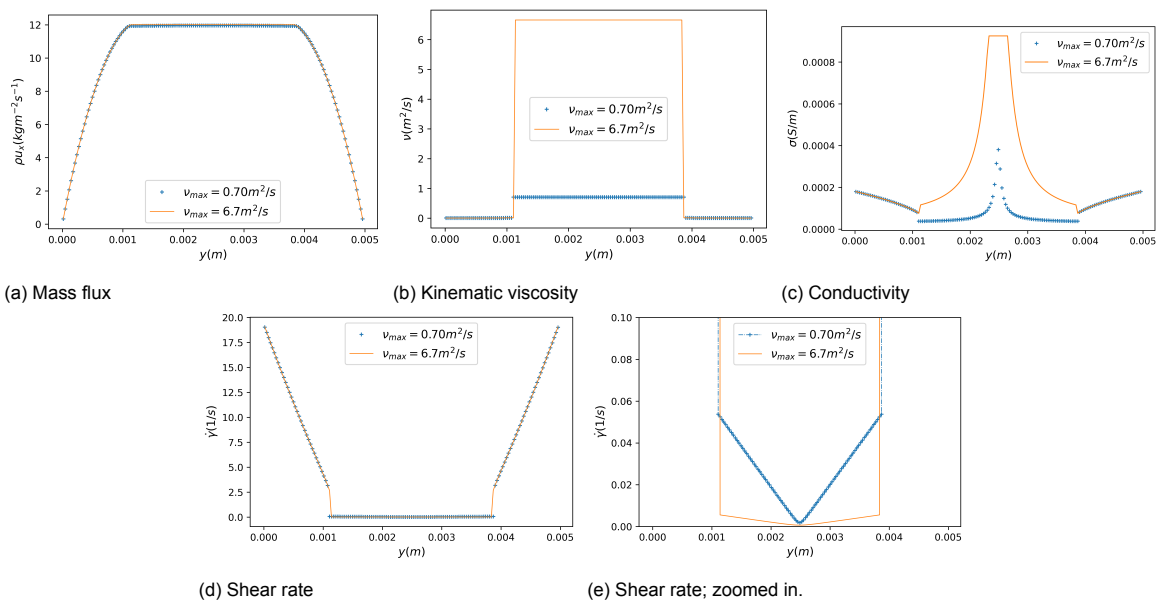


Figure 6.21: Simulation results of carbon black suspension flowing between two parallel plates for two different low shear rate viscosity-cutoff locations. The mass flux, kinematic viscosity, conductivity and shear rate profiles are taken halfway the flow channel. Orange line: Below a shear rate of 0.012 s^{-1} the kinematic viscosity $6.7 \text{ m}^2 \text{ s}^{-1}$. Blue plus symbols: Below a shear rate of 0.084 s^{-1} the kinematic viscosity $0.70 \text{ m}^2 \text{ s}^{-1}$.

Viscosity-cutoff at High Shear Rates

The viscosity-cutoff at high shear rates is analysed by studying the simulation of the flow with inlet velocity of 1.0 m s^{-1} in more detail. In figure 6.22 the mass flux, shear rate and kinematic viscosity profiles are plotted in the same figure. The red dotted lines give the locations of the shear rate cutoffs. They divide the channel in three regions. In the outer regions the shear rate is above the cutoff value and the kinematic viscosity is constant. This means that in these regions the fluid behaves as a Newtonian fluid. Considering that the flow behaviour at the walls greatly influences the flow in the center and that the Newtonian regions encompass more than half of the channel, most likely this simulation is not a correct representation of reality.

To summarize, viscosity-cutoff at low shear rates only slightly affects the flow behaviour. However, in combination with a conductivity-shear rate relation that is very steep at low shear rates, the viscosity-cutoff can lead to large inaccuracies in the conductivity. A viscosity-cutoff at high shear rates results in an inaccurate description of the flow at the walls. This affects the fluid dynamics and the conductivity in the entire channel.

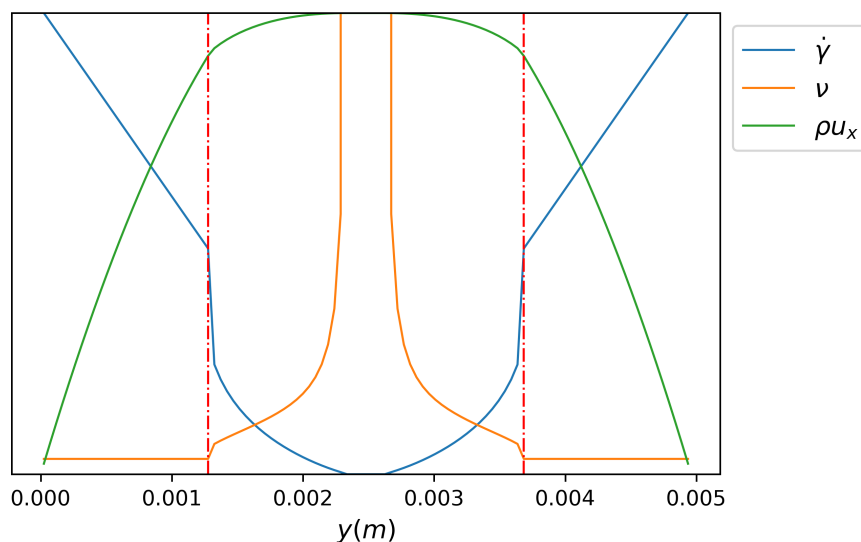


Figure 6.22: Simulation result of carbon black suspension flowing between two parallel plates with inlet velocity of 1.0 m s^{-1} . Mass flux, shear rate and kinematic viscosity profile taken halfway the channel. The vertical red lines mark the locations of high shear rate viscosity-cutoffs.

All simulations that were presented in section 6.3.2 have a viscosity-cutoff at low shear rates and most of them have a viscosity-cutoff at low shear rates too. Therefore the results, especially of the simulations with a high shear rate cutoff, likely deviate from reality. This issue can be resolved by measuring the viscosity and conductivity over a wider range of shear rates.

6.3.5. Asymmetries

Some of the results presented in this section show asymmetries (e.g., figures 6.15, and 6.16.) This is surprising considering that the flow channel geometry, boundary conditions and inlet velocity are perfectly symmetric about the middle of the channel. Possibly these asymmetries can be attributed to the steep slope of the viscosity-shear rate relation in the low shear rate region. Small shear rate inaccuracies are magnified into larger inaccuracies in the viscosity. This in turn affects the shear rate, leading to a self-reinforcing inaccuracy. This hypothesis is supported by the observation that the asymmetries occur mainly in the low shear rate regions of the channel.

6.4. Total Internal Resistance

The total internal resistance is the sum of the carbon black electronic resistance, the charge transfer resistance, the electrolyte ionic resistance and the membrane ionic resistance.

- The carbon black electronic resistance depends on the flow characteristics and was computed with a finite volume model. The results of the resistivity in one half cell are presented in section 6.3 for a flow channel of $5 \text{ mm} \times 22.5 \text{ mm} \times 50 \text{ mm}$. The carbon black resistance has a minimum of $4.94 \text{ k}\Omega$ at zero fluid velocity. This computation was based on the assumption that the electrons travel all the way from the membrane to the current collector.
- The electrolyte ionic resistance depends on the ionic conductivity and the paths of the ions. For the computation of the ionic resistance a similar assumption is made as for the electronic carbon black resistance: The ionic current flows all the way from the current collector to the membrane. Additionally, the same geometry ($5 \text{ mm} \times 22.5 \text{ mm} \times 50 \text{ mm}$) is used. The ionic conductivity is taken to be constant throughout the medium, assuming that changes in concentration as a result of the reactions do not play a significant role. Based on literature, the ionic conductivity is esti-

mated at 50 mS/cm (see section 2.1.2). Under these assumptions the ionic resistance is 0.9 Ω per half cell (equation 6.4).

- Based on literature (see section 2.1.3) the membrane ionic conductivity is estimated at 4 mS/cm, and its thickness at 50 μm . A membrane with an area of 22.5 mm \times 50 mm has an internal resistance of 0.1 Ω (equation 6.4).
- The charge transfer resistance is unknown.

The ionic resistances of the electrolyte and membrane are negligible compared to the electronic resistance of the carbon black network. This is logical considering that the maximum electronic conductivity of carbon black (0.009 mS/cm) is orders of magnitude smaller than the ionic conductivity of the electrolyte. The ionic conduction is therefore not a limiting factor for the reaction rate. The charge transfer resistance for this reaction has not been quantified yet. Without this information it is impossible to distinguish the dominant source of resistance.

It should be emphasised that the electronic carbon black resistance was computed based on conductivity measurements of non-aqueous carbon black suspensions (see section 2.5) [22]. In contrast to this fluid, the alginate-based electrolyte is aqueous. As discussed in section 2.1.2 aqueous carbon black suspensions at rest typically have a much higher conductivity than non-aqueous carbon black suspensions and can reach values of a few mS/cm [5][7][22]. Hence, to get a more accurate estimate of the carbon black resistance, the conductivity-shear rate relation used here must be replaced with that of an aqueous carbon black suspension. Potentially this could lead to a 100-fold decrease in electronic carbon black resistance. Even in that case the ionic resistance is an order of magnitude lower than the electronic conductivity.

It must be noted that in the above calculations the carbon black electronic resistance and electrolyte ionic resistance are overestimated. This is due to the assumption that the paths of the electronic and ionic current span the entire height of the half cell. In reality the reaction can take place anywhere in the half cell. From the location of the reaction an electronic current flows towards the current collector and an ionic current flows towards the membrane. The current flowing between the two half cells is given by equation 6.6.

$$I = \frac{V}{R} = \frac{V_{reaction}}{R_m^i + R_e^i + R_{CB}^e + R_{CT} + R^{ext}} \quad (6.6)$$

In this equation $V_{reaction}$ is the reaction potential, R_m^i the ionic resistance of the membrane, R_e^i the ionic resistance of the electrolyte, R_{CB}^e the electronic resistance of the carbon black, R_{CT} the charge transfer resistance and R^{ext} the resistance of the external circuit. Assuming approximately homogeneous concentrations the reaction potential is constant throughout the cell. The ionic resistance of the electrolyte and the electronic resistance of the carbon black depend on the path of the electronic and ionic current respectively, and hence on the locations of the half reactions. All other resistances are the same for each reaction. Based on this, three scenarios are considered:

- **The electronic resistivity is dominant:** In this scenario the total resistance is lowest for reactions that occur close to the current collectors. As a result, the total current is dominated by contributions that originate from reactions close to the membrane.
- **The ionic resistivity of the electrolyte is dominant:** In this case, the majority of reactions take place close to the membrane where the ionic path length, and hence electrolyte resistance, is minimal.
- **The charge transfer resistance, external resistance or membrane resistance is dominant:** These three resistances are independent of the location of the reaction. Consequently, in this scenario the reactions occur approximately uniformly spread over the flow channel.

6.5. Validation of Conductivity Conversion Method

Chapter 5 discusses a conversion algorithm to convert the resistance data obtained with a parallel plate rheometer into conductivity as a function of shear rate. The algorithm is validated by taking an arbitrary conductivity-shear rate curve ($\sigma(\dot{\gamma})$) and integrating it from $\dot{\gamma} = 0$ to $\frac{\omega r}{H}$ (equation 5.14) to obtain the conductance as a function of angular frequency ($\Sigma(\omega)$). Applying the algorithm to this conductance curve should reproduce the initial conductivity curve. The algorithm has been validated for multiple fluids with different conductivity-shear rate relations. The results of two validation fluids are presented below:

- The first validation fluid is the non-aqueous carbon black slurry as described by Yousry *et al.* [22]. (This fluid was analysed in section 6.3.) The conductivity as a function of shear rate is given by equation 2.31. The shear rate was divided into $N = 1000000$ evenly spaced intervals. The conductance and corresponding conductivity are shown in figure 6.23.

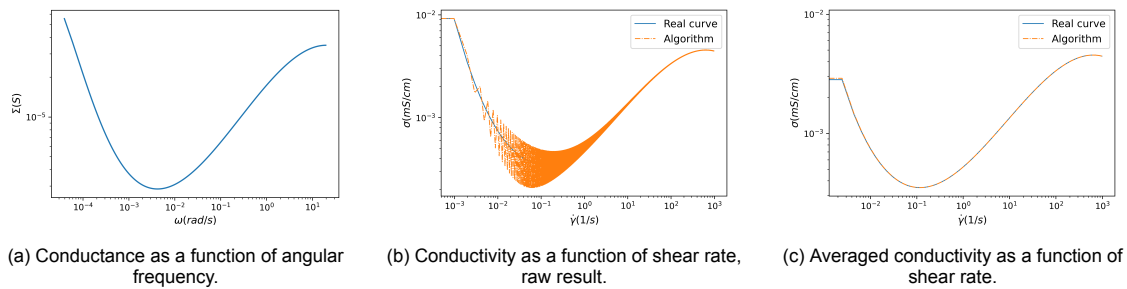


Figure 6.23: Conductance and conductivity of nonaqueous carbon black suspension. Both the real conductivity-shear rate curve (blue) and the curve obtained with the algorithm (orange) are plotted in figures b and c. The raw output of the algorithm (subfigure b) has clear oscillations. In the plot in subfigure c the oscillations are averaged out.

- The second validation fluid is a hypothetical fluid with a conductivity-shear rate relation characterised by equation 6.7. The shear rate was divided into $N = 100000$ evenly spaced intervals. The results of the conductance-to-conductivity conversion of this fluid are shown in figure 6.24.

$$\sigma(\dot{\gamma}) = \sqrt{\dot{\gamma} + 1000} \tag{6.7}$$

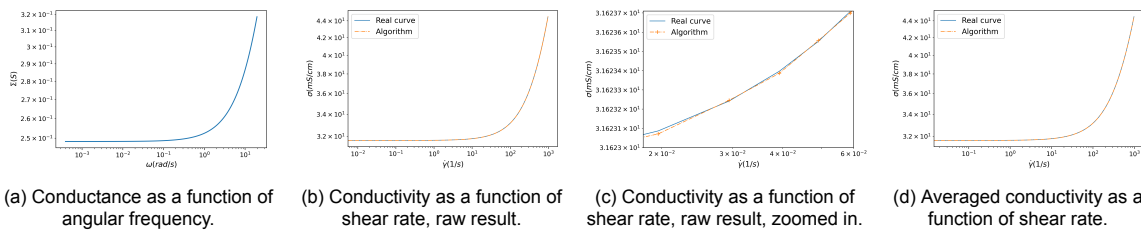


Figure 6.24: Conductance and conductivity of validation fluid 2. Both the real conductivity-shear rate curve (blue) and the curve obtained with the algorithm (orange) are plotted in figures b and c. The raw output of the algorithm (subfigure b) and the averaged output (subfigure d) are almost identical. When zooming in on the raw output (subfigure c) small oscillations are visible.

For both fluids the experimentally obtained conductance as a function of angular frequency ($\Sigma(\omega)$) is plotted next to the conductivity as a function of shear rate ($\sigma(\dot{\gamma})$). The initial conductivity-shear rate curve (blue) and the curve obtained with the algorithm (orange) are plotted in the same figure. Figure 6.23b gives the raw conductivity-shear rate output for the carbon black suspension. The raw curve oscillates around the real curve. These oscillations are removed by averaging. Figure 6.23c presents the averaged curve. In the raw conductivity-shear rate curve of validation fluid 2 the oscillations are much less pronounced. The raw and averaged results look almost identical (figures 6.24b and 6.24d). When zooming in on the raw curve small oscillations are visible (figure 6.24c).

Presumably the oscillation in the conductivity of the carbon black suspension are stronger because for this fluid the slope of the curve changes a lot within one shear rate interval, meaning that the assumption of linear behaviour is not very accurate. This also affects the accuracy of the method: the maximum relative error of the averaged conductivity with respect to the real conductivity is 3 % for the carbon black suspension and 5×10^{-5} % for validation fluid 2. The mean error (averaged over the entire curve) is 0.002 % for the carbon black suspension and 1×10^{-5} %. This accuracy is adequate for the purpose of this study, considering that in this early stage of research there are many other inaccuracies and assumptions that cause larger errors.

Using smaller shear rate intervals would improve the accuracy because the slope of the derived curve would deviate less from the actual slope. Ideally, to save computational time, the grid is only refined locally at shear rates where the conductivity curve is highly non-linear. This however, requires the algorithm to be adapted in such a way that it allows for varying shear rate intervals.

Conclusions and Recommendations

Energy storage plays a crucial role in the decarbonisation of the electricity sector. Large-scale energy storage systems must be safe and affordable. To meet these criteria, a novel aqueous semi-solid flow battery (SSFB) with an alginate-based electrolyte was proposed. Semi-solid electrolytes contain carbon black particles for electronic conduction. Due to these carbon black particles, the electrolytes exhibit non-Newtonian flow behaviour and have an electronic conductivity that depends on shear rate [12][21][23][22]. Internal electrical resistance and mechanical friction limit a flow battery's energy efficiency [7]. The goal of this research was to contribute to a better understanding of these two sources of energy loss. To this end, a fluid dynamics model and a model for the electric field were developed and combined to find the internal electrical resistance under various flow conditions. The viscosity and conductivity as a function of shear rate are important inputs for the simulations and can be determined with rheo-impedance measurements. As part of this thesis, an experimental method for rheo-impedance measurements was developed.

7.1. Simulation of Rheology and Electric Field in SSFBs

The lattice Boltzmann method was employed for the fluid dynamics model. In this research two different lattice Boltzmann models were set up: one based on the multiple relaxation time collision operator (MRT) and the other using a filter matrix approach (FMLB). In a validation study with three well-defined fluids (Newtonian, shear thinning and shear thickening), the simulation results of both models matched the analytical results in the majority (~90 %) of the channel. Only in a small region at the inlet the model yielded a non-physical output. This issue was mitigated by excluding the first part of the channel in further analyses and calculations.

A finite volume model was set up to compute the electric field in the flow channel. To simplify the situation all reactions are assumed to occur close to the membrane such that the flow channel could be represented as a rectangular inhomogeneous resistance. The finite volume model computes the electric field in the resistance as a result of an applied voltage, which then is used to derive the internal resistance. A benchmark study using a flow channel with homogeneous conductivity demonstrated that the model accurately represents the theoretical situation.

The two models were combined to determine the internal electronic resistance of the flowing electrolyte. Because the conductivity and viscosity of the alginate-based electrolyte have not yet been determined, a comparable fluid (a nonaqueous carbon black suspension with known conductivity and viscosity) was used as replacement. The flow of the carbon black suspension through the battery was simulated with the MRT and FMLB model. The results of both models showed asymmetries which are attributed to the steep slope of the viscosity-shear rate relation at low shear rates which magnifies small inaccuracies. The MRT model had stronger asymmetries, a worse outflow convergence and, in some cases, stability issues. The FMLB model is therefore better suited for simulations of the carbon black suspension.

The internal electronic resistance was determined for a range of inflow velocities and for a flow channel with a height of 5 mm, a length of 22.5 mm and a width of 50 mm. It has a minimum of 5 k Ω at zero fluid velocity and peaks at >25 k Ω between 0.001 m s⁻¹ to 0.1 m s⁻¹. Because the viscosity was unknown above a certain shear rate, the range of inlet velocities was limited. In addition to the internal resistance, the pumping power was computed for a range of inlet velocities. The pumping power increases with velocity as a power law with an exponent of ~1.5. This steep increase should be taken into consideration when deciding on the inlet velocity of the semi-solid flow battery.

The internal ionic resistance was determined by a simple calculation based on conductivity data from literature [5][34][35][36][37]. Both the ionic resistance of the electrolyte ($\approx 0.9 \Omega$) and of the membrane ($\approx 0.1 \Omega$) were orders of magnitude smaller than the minimum electronic resistance of the carbon black particles. Ionic transport therefore is not a limiting factor for the reaction rate. Determining the total internal resistance was impossible because the charge transfer resistance was unknown. It is likely that using the data of a nonaqueous suspension instead of that of an aqueous suspension causes a significant overestimation of the internal electronic resistance.

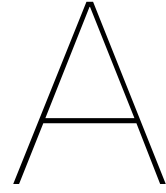
7.2. Experimental Method for Rheo-impedance Measurements

As part of this thesis an experimental method for simultaneous viscosity and conductivity measurements was proposed, including an algorithm that converts the raw experimental data into a conductivity-shear rate curve. The experimental setup is a parallel plate rheometer equipped with a dielectro-rheological device. The device measures torque and conductance as a function of angular frequency. A method found by Cross and Kaye [51] gives reliable results for the conversion of torque as a function of angular frequency into viscosity as a function of shear rate. For the conversion of conductance as a function of angular frequency into conductivity as a function of shear rate on the other hand, a dedicated algorithm was developed and validated. The error of the derived conductivity with respect to its real value was well below 5% in the validation study, which is adequate for the purpose of this research. The algorithm gives more accurate results for finer shear rate intervals. When a better accuracy is desired, adapting the algorithm such that it allows for local refinement of the shear rate grid is recommended.

7.3. Recommendations

The description of energy losses in alginate-based SSFBs put forward in this thesis is not complete. This is partly due to a lack of information, partly due to the gross simplification of the electrochemical processes and geometry and partly due to inaccuracies in the models. The following recommendations are therefore given for further research:

- The viscosity and conductivity of the electrolyte suspension play a vital role in the internal resistance. These properties are inputs for the internal resistance model and vary significantly per suspension. Therefore, measuring the viscosity and conductivity of the alginate electrolyte will contribute significantly to our understanding of alginate SSFBs. Future research should measure the viscosity and conductivity for a wide range of shear rates. This removes the need for a viscosity-cutoff that limits the accuracy of the simulations. Rheo-impedance measurements can also be used to study the influence of factors including electrolyte composition, pH and temperature on rheological and electrical properties [5][12][21][23][22].
- In addition, setting up a coupled electrochemical-transport model of the battery is recommended to get a more complete description of the electrochemical performance. This model should incorporate the location of the reactions. Experimental work must be performed to investigate the reaction kinetics and determine inputs for the model such as the activation overpotential.
- Since carbon black suspensions have been reported to exhibit thixotropic behaviour [12], it would be interesting to investigate the history dependence of the flow field and internal resistance.
- Finally, improving and extending the fluid dynamics model is recommended. The model can be improved by removing the asymmetries, by finding a solution for the non-physical behaviour in the inlet region, by implementing a more realistic geometry (e.g., realistic shape of the in- and outlet) and by adding a third spatial dimension.



Systematic Analysis of Boundary Techniques for Lattice Boltzmann Method

This appendix presents the results of a systematic analysis of techniques for open boundary conditions in lattice Boltzmann simulations of the parallel plate flow of non-Newtonian fluids. Sections 3.4.2 and 3.4.3 introduce multiple boundary techniques for the open boundaries at the inlet and outlet of the flow channel. The goal of this analysis was to find the optimal combination of inlet and outlet boundary technique. To this purpose, all combinations of inlet and outlet boundary techniques have been evaluated for both the MRT model and for the FMLB model. To ensure that the combination of boundary technique works for different fluid types, four different fluids have been included in this analysis. Their characteristics are stated in table A.1.

Table A.1: Fluid characteristics.

Fluid type	Kinematic viscosity
Newtonian (n=1)	$\nu = 2 \times 10^{-6} \text{ m}^2/\text{s}^{-1}$
Shear thinning (n=0.2)	$\nu = K/\rho\dot{\gamma}^{n-1}$ $K/\rho = 0.004 \text{ m}^2/\text{s}^{1.8}$
Shear thickening (n=2)	$\nu = K/\rho\dot{\gamma}^{n-1}$ $K/\rho = 1 \times 10^{-5} \text{ m}^2$
Yousry fluid	Empirical viscosity relation

The lattice Boltzmann models (MRT and FMLB) simulate fluid flow between parallel plates. For the boundary technique analysis the following input parameters were used:

$$W = 5 \times 10^{-3} \text{ m}, L = 25 \times 10^{-3} \text{ m}, u_x^{in} = 0.01 \text{ ms}^{-1}, N_y = 25, N_x = 125.$$

Simulations were run for four fluids and for all 10 combinations of boundary techniques. The results are presented in figure A.1. From these results it is clear that the FMLB model gives the best output with the Neumann method at the outlet in combination with either of the two inlet boundary techniques. For the MRT model the preferred choice of boundary techniques is the bounce back method at the inlet in combination with the extrapolation condition method at the outlet.

B

Simulation Parameters

This appendix presents the (dimensionless) simulation parameters of the lattice Boltzmann simulations that were presented in chapter 6. The physical parameters are linearly related to the simulation parameters as given by equation B.1.

$$Q_{physical} = Q_{simulation} C_Q \quad (\text{B.1})$$

The conversion factors used for the simulations in this thesis are given in table B.1. There are three independent conversion factors. The other conversion factors are combinations of the three independent factors.

Table B.1: Conversion factors

Physical quantity	Conversion factor	Value
Density	C_ρ (kg/m ³)	ρ/ρ_{sim}
Kinematic viscosity	C_ν (m ² /s)	ν/ν_{sim}
Velocity	C_u (m s ⁻¹)	u^{in}/u_{sim}^{in}
Distance	C_l (m)	C_ν/C_u
Time	C_t (s)	C_l/C_u
Fluid consistency coefficient divided by density	$C_{K/\rho}$ (m ² /s ⁿ⁻²)	$C_\nu C_t^{n-1}$

The general simulation parameters (i.e. parameters that were used in all simulations) are listed in table B.2.

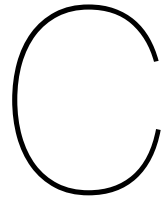
Table B.2: General simulation parameters.

Quantity	Value in lattice units (dimensionless)
Lattice spacing	$\Delta x = \Delta y = 1$
Time step	$\Delta t = 1$
Density	$\rho_{sim} = 1$
Channel length	$L_{sim} = N_x \Delta x$
Channel height	$H_{sim} = N_y \Delta y$
Speed of sound	$c_s = \frac{\Delta x}{\Delta t \sqrt{3}} = 1/\sqrt{3}$

The other input parameters differ per simulation and depend on the physical inlet velocity and the desired the grid size. Table B.3 presents simulation parameters of the benchmark simulations that were presented in section 6.1.

Table B.3: Simulation parameters used in benchmark simulations.

Fluid type	Newtonian	Shear thinning ($n = 0.2$)	Shear thickening ($n = 2$)
N_x	50	50	50
N_y	250	250	250
u_{sim}^{\dagger}	0.0005	0.00025	0.001
$C_v(\text{m}^2/\text{s})$	0.002	0.004	0.001



Codes

This QR code links to a gitlab page where all python codes of the developed models can be found.



Bibliography

- [1] V Masson-Delmotte et al. *IPCC, 2021: Climate Change 2021: The Physical Science Basis. Contribution of Working Group I to the Sixth Assessment Report of the Intergovernmental Panel on Climate Change*. 2021.
- [2] IEA. "Global Energy and CO₂ Status Report 2018". In: *International Energy Agency, Paris* 562 (2019).
- [3] IEA. "World Energy Outlook 2021". In: *International Energy Agency, Paris* (2021).
- [4] M Skyllas-Kazacos, C Menictas, and T Lim. "Redox flow batteries for medium-to large-scale energy storage". In: *Electricity Transmission, Distribution and Storage Systems*. Elsevier, 2013, pp. 398–441.
- [5] Zheng Li et al. "Aqueous semi-solid flow cell: demonstration and analysis". In: *Physical Chemistry Chemical Physics* 15.38 (2013), pp. 15833–15839.
- [6] Simone van den Akker. "Experimental study on the electrochemical ability of Mn alginate and Fe alginate complexes in an aqueous Na alginate electrolyte with the purpose of a semi solid flow cell". In: [Unpublished Master Thesis]. Delft University of Technology (2021).
- [7] Thaneer Malai Narayanan et al. "Low-cost manganese dioxide semi-solid electrode for flow batteries". In: *Joule* 5.11 (2021), pp. 2934–2954.
- [8] Mihai Duduta et al. "Semi-solid lithium rechargeable flow battery". In: *Advanced Energy Materials* 1.4 (2011), pp. 511–516.
- [9] Wei Wang et al. "Recent progress in redox flow battery research and development". In: *Advanced Functional Materials* 23.8 (2013), pp. 970–986.
- [10] Remy Lacroix et al. "Modelling the rheology and electrochemical performance of Li₄Ti₅O₁₂ and LiNi_{1/3}Co_{1/3}Mn_{1/3}O₂ based suspensions for semi-solid flow batteries". In: *Electrochimica Acta* 304 (2019), pp. 146–157.
- [11] Zhaoxiang Qi and Gary M Koenig Jr. "Flow battery systems with solid electroactive materials". In: *Journal of Vacuum Science & Technology B, Nanotechnology and Microelectronics: Materials, Processing, Measurement, and Phenomena* 35.4 (2017), p. 040801.
- [12] Aditya Narayanan, Frieder Mugele, and Michael HG Duits. "Mechanical history dependence in carbon black suspensions for flow batteries: A rheo-impedance study". In: *Langmuir* 33.7 (2017), pp. 1629–1638.
- [13] China Energy Storage Alliance. *CNESA Global Energy Storage Market Analysis-2020.Q1*. <http://en.cnesa.org/latest-news/2020/5/28/cnesa-global-energy-storage-market-analysis-2020q1-summary>, Last accessed on 2020-2-17. 2020.
- [14] Narges Ghorbani, Hamed Makian, and Christian Breyer. "A GIS-based method to identify potential sites for pumped hydro energy storage-Case of Iran". In: *Energy* 169 (2019), pp. 854–867.
- [15] O Ramadan et al. "Analysis of compressed air energy storage for large-scale wind energy in Suez, Egypt". In: *International Journal of Low-Carbon Technologies* 11.4 (2016), pp. 476–488.
- [16] Sarah Hamdy, Tatiana Morosuk, and George Tsatsaronis. "Cryogenics-based energy storage: Evaluation of cold exergy recovery cycles". In: *Energy* 138 (2017), pp. 1069–1080.
- [17] Qinghua Yu et al. "Cryogenic energy storage and its integration with nuclear power generation for load shift". In: *Storage and Hybridization of Nuclear Energy*. Elsevier, 2019, pp. 249–273.
- [18] Haisheng Chen et al. "Progress in electrical energy storage system: A critical review". In: *Progress in natural science* 19.3 (2009), pp. 291–312.

- [19] Iain Staffell et al. "The role of hydrogen and fuel cells in the global energy system". In: *Energy & Environmental Science* 12.2 (2019), pp. 463–491.
- [20] Furquan Nadeem et al. "Comparative review of energy storage systems, their roles, and impacts on future power systems". In: *IEEE access* 7 (2018), pp. 4555–4585.
- [21] Mohamed Youssry et al. "Aqueous dispersions of carbon black and its hybrid with carbon nanofibers". In: *RSC advances* 8.56 (2018), pp. 32119–32131.
- [22] Mohamed Youssry et al. "Non-aqueous carbon black suspensions for lithium-based redox flow batteries: rheology and simultaneous rheo-electrical behavior". In: *Physical Chemistry Chemical Physics* 15.34 (2013), pp. 14476–14486.
- [23] Yuzi Zhang, Joseph P Sullivan, and Arijit Bose. "Rheological and microstructural characterization of aqueous suspensions of carbon black and reduced graphene oxide". In: *Colloids and Surfaces A: Physicochemical and Engineering Aspects* 592 (2020), p. 124591.
- [24] Chongrui Dong et al. "Design Strategies for High-Voltage Aqueous Batteries". In: *Small Structures* 2.7 (2021), p. 2100001.
- [25] Alireza Heidarian, Sherman CP Cheung, and Gary Rosengarten. "The effect of flow rate and concentration on the electrical conductivity of slurry electrodes using a coupled computational fluid dynamic and discrete element method (CFD–DEM) model". In: *Electrochemistry Communications* 126 (2021), p. 107017.
- [26] Kudakwashe Chayambuka, Jan Fransaer, and Xochitl Dominguez-Benetton. "Modeling and design of semi-solid flow batteries". In: *Journal of Power Sources* 434 (2019), p. 226740.
- [27] Victor E Brunini, Yet-Ming Chiang, and W Craig Carter. "Modeling the hydrodynamic and electrochemical efficiency of semi-solid flow batteries". In: *Electrochimica acta* 69 (2012), pp. 301–307.
- [28] Kun Yang, Shaoping Xiong, and Haitao Zhang. "A comprehensive 3D multi-physics coupled simulation model of slurry redox flow batteries". In: *Journal of Power Sources* 531 (2022), p. 231315.
- [29] Siddhesh N Pawar and Kevin J Edgar. "Alginate derivatization: a review of chemistry, properties and applications". In: *Biomaterials* 33.11 (2012), pp. 3279–3305.
- [30] Gregor T Grant et al. "Biological interactions between polysaccharides and divalent cations: the egg-box model". In: *FEBS letters* 32.1 (1973), pp. 195–198.
- [31] Chuhuan Hu et al. "Ions-induced gelation of alginate: Mechanisms and applications". In: *International Journal of Biological Macromolecules* (2021).
- [32] H Parant et al. "Flowing suspensions of carbon black with high electronic conductivity for flow applications: Comparison between carbons black and exhibition of specific aggregation of carbon particles". In: *Carbon* 119 (2017), pp. 10–20.
- [33] H. Strathmann. "MEMBRANE SEPARATIONS | Electrodialysis". In: *Encyclopedia of Separation Science*. Ed. by Ian D. Wilson. Oxford: Academic Press, 2000, pp. 1707–1717. ISBN: 978-0-12-226770-3. DOI: <https://doi.org/10.1016/B0-12-226770-2/05131-0>. URL: <https://www.sciencedirect.com/science/article/pii/B0122267702051310>.
- [34] Muhammad Zahir Iqbal, Sana Zakar, and Syed Shabhi Haider. "Role of aqueous electrolytes on the performance of electrochemical energy storage device". In: *Journal of Electroanalytical Chemistry* 858 (2020), p. 113793.
- [35] Parveen Kumar and S Yashonath. "Ionic conductivity in aqueous electrolyte solutions: Insights from computer simulations". In: *Journal of Molecular Liquids* 277 (2019), pp. 506–515.
- [36] Are Yllö and Chao Zhang. "Experimental and molecular dynamics study of the ionic conductivity in aqueous LiCl electrolytes". In: *Chemical Physics Letters* 729 (2019), pp. 6–10.
- [37] Miranda J Baran et al. "Design rules for membranes from polymers of intrinsic microporosity for crossover-free aqueous electrochemical devices". In: *Joule* 3.12 (2019), pp. 2968–2985.
- [38] Timm Krüger et al. "The lattice Boltzmann method". In: *Springer International Publishing* 10.978-3 (2017), pp. 4–15.

- [39] Congshan Zhuo, Chengwen Zhong, and Jun Cao. "Filter-matrix lattice Boltzmann model for incompressible thermal flows". In: *Physical Review E* 85.4 (2012), p. 046703.
- [40] David J. Griffiths. *Introduction to Electrodynamics*. Pearson, 2013. ISBN: 978-0-321-85656-2.
- [41] Dominique d'Humières. "Multiple-relaxation-time lattice Boltzmann models in three dimensions". In: *Philosophical Transactions of the Royal Society of London. Series A: Mathematical, Physical and Engineering Sciences* 360.1792 (2002), pp. 437–451.
- [42] Zhenhua Chai et al. "Multiple-relaxation-time lattice Boltzmann model for generalized Newtonian fluid flows". In: *Journal of Non-Newtonian Fluid Mechanics* 166.5-6 (2011), pp. 332–342.
- [43] Michael E McCracken and John Abraham. "Multiple-relaxation-time lattice-Boltzmann model for multiphase flow". In: *Physical Review E* 71.3 (2005), p. 036701.
- [44] Manju Bisht and Dhiraj V Patil. "Assessment of multiple relaxation time-lattice Boltzmann method framework for non-Newtonian fluid flow simulations". In: *European Journal of Mechanics-B/Fluids* 85 (2021), pp. 322–334.
- [45] JA Somers. "Direct simulation of fluid flow with cellular automata and the lattice-Boltzmann equation". In: *Applied Scientific Research* 51.1-2 (1993), pp. 127–133.
- [46] Qisu Zou and Xiaoyi He. "On pressure and velocity boundary conditions for the lattice Boltzmann BGK model". In: *Physics of fluids* 9.6 (1997), pp. 1591–1598.
- [47] Qin Lou, Zhaoli Guo, and Baochang Shi. "Evaluation of outflow boundary conditions for two-phase lattice Boltzmann equation". In: *Physical review E* 87.6 (2013), p. 063301.
- [48] Salvador Izquierdo and Norberto Fueyo. "Characteristic nonreflecting boundary conditions for open boundaries in lattice Boltzmann methods". In: *Physical Review E* 78.4 (2008), p. 046707.
- [49] Robert Eymard, Thierry Gallouët, et al. "Finite volume method". In: *Scholarpedia* 5.6 (2010), p. 9835.
- [50] MM Cross and A Kaye. "Techniques for the viscometry of suspensions". In: *Polymer Engineering & Science* 26.2 (1986), pp. 121–126.
- [51] MM Cross and A Kaye. "Simple procedures for obtaining viscosity/shear rate data from a parallel disc viscometer". In: *Polymer* 28.3 (1987), pp. 435–440.
- [52] Mikel Zubieta, María Jesús Elejabarrieta, and Mounir Bou-Ali. "A numerical method for determining the shear stress of magnetorheological fluids using the parallel-plate measuring system". In: *Rheologica acta* 48.1 (2009), pp. 89–95.
- [53] Primož Ternik. "Planar sudden symmetric expansion flows and bifurcation phenomena of purely viscous shear-thinning fluids". In: *Journal of non-newtonian fluid mechanics* 157.1-2 (2009), pp. 15–25.